國立交通大學

電子物理學系

博士論文

奈米線之製備及其熱、電傳導與熱力學性質之研究

Fabrication and Investigation of transport and

thermodynamic properties of nanowires

學　　　　號：　9221809

研　究　　生：　歐敏男

指　導　教　授：　楊宗哲 (Dr. Yang, Tzong-Jer)　教授

陳洋元 (Dr. Chen, Yang-Yuan)　教授

中 華 民 國 九 十 七 年 六 月

奈米線之製備及其熱、電傳導與熱力學性質之研究

學生：歐敏男　　　　　　　　　　　　　指導教授：楊宗哲 教授

　　　　　　　　　　　　　　　　　　　　　　　　陳洋元 教授

國立交通大學電子物理學系（研究所）碩士班

摘要

　　許多實驗結果顯示低維度材料具有與塊狀材料迥異的特性，這些性質的改變可能肇因於材料尺寸的縮減。以一維量子線之奈米線為例，其電子能態的分佈受到量子侷限限效應的改變，或因表面原子的比例增加，這些都可能是導致材料熱、電、磁等性質改變的原因。為了研究奈米線的各種物理性質，我們分別利用自組構與微影製程這兩種方法製備群聚之奈米線陣列及單一鎳奈米線。我們以電化學沉積法讓材料填充於陽極氧化鋁(AAO)模板的孔洞中，製作奈米線陣列。以此方法我們製作六角形排列之鐵(Fe)與三碲化二鉍(Bi_2Te_3)奈米線陣列，用以研究其群聚之磁性與電性。其中鐵奈米線之線徑約 60 及 200 奈米，而三碲化二鉍奈米線之線徑則約 60 奈米。X 光繞射顯示，60 奈米的鐵與三碲化二鉍奈米線陣列均具有較好的結晶性，而線徑約 200 奈米之鐵奈米線陣列，並無此明顯特徵。進一步的磁性量測結果顯示，60 奈米鐵之飽合場較小且矯頑場較大，顯示 60 奈米鐵確實具有較強之磁異向性能，此外其在小外加磁場中磁阻的變化與外加磁場大小呈現平方關係，與材料之退磁場效應相關。

　　金屬的許多特性均與電子的行為相關，如金屬的熱傳導主要來自電子的貢獻，因此金屬材料的電導率與熱導率比值遵守 Wiedemann-Franz 定律，研究單一鎳奈米線之熱導性與電導性可以獲得電子與聲子在一維材料中的傳輸行為，並進一步瞭解電子在材料中的特性。我們整合光與電子束微影製程、薄膜沉積及蝕

刻技術用以製備一根懸橋結構之鎳奈米線，其截面為 100 奈米厚及 180 奈米寬之矩形，長約 35 微米。磁阻之量測顯示單一之鎳奈米線仍保有鐵磁性，其矯頑場約 500 Oe。我們用自行開發的電性量測系統與三倍頻技術(3ω technique)量測此鎳奈米線在溫度 15~300 K 之間的電阻率、熱傳導率與比熱，其室溫電阻率約為 36 μΩ-cm，殘餘電阻率約 17 μΩ-cm，因此其 RRR ~ 2 (Residual Resistivity Ratio)，較一般塊材小，顯示此奈米線中具有許多雜質與缺陷，使電子受到嚴重的散射。熱導率量測之結果亦顯示奈米線之室溫熱導率約為塊材的 20%，且其值隨溫度下降而下降，明顯與塊材不同。熱傳導率與電導率的量測結果顯示奈米線其電聲子傳導特性僅於 75-300 K 之間符合接近 Wiedemann-Franz 定律，顯示鎳奈米線中熱流的傳播比電流更受到壓抑。

Fabrication and Investigation of transport and thermodynamic properties
of nanowires

student： Min-Nan Ou　　　　　Advisors： Dr. Yang, Tzong-Jer

Dr. Chen, Yang-Yuan

Department of Electrophysics
National Chiao Tung University

Abstract

There are experiments revealing changes of physical properties in low dimensional materials likely due to size reduction. In quasi one dimension nanowires, the quantum confinement and surface effect may affect their magnetism, transport, and thermodynamic properties. To evaluate these one-dimensional properties a bottom-up method was used to fabricate iron and Bi_2Te_3 nanowires in an AAO template using chemical electrodeposition. The average diameters of two highly ordered iron nanowires are about 60 and 200 nm, respectively, and that of Bi_2Te_3 nanowires is 60 nm. Magnetization measurements show a larger anisotropic magnetization in both 60-nm nanowires. It is illustrated by the formation of magnetic easy axis and preferred crystal orientation of [110] along the longitudinal axes of nanowires. The quadratic magnetic field dependence of normalized magnetoresistance (MR) at low field is attributed to the additional effect of demagnetization in low dimensional systems.

A top-down fabrication method was employed to create single nickel

nanowires for the direct study of transport and thermodynamic properties in one wire. Optic, e-beam lithography, thermal evaporation, and etching techniques were applied to construct individual and sagging nickel nanowires on a silicon wafer. The thermal conductivity of the sagging nickel nanowire was measured between 15 and 300 K. The room temperature and 0.5 K electrical resistivity are about 36 μΩ-cm and 17 μΩ-cm respectively, giving a low residual resistivity ratio (RRR) of only 2. As compared to the bulk Ni，this result indicates that the conductive electrons are strongly scattered by defects and impurities. The temperature dependence of thermal conductivity and Lorenz number also significantly differ from that of the bulk. Transport measurement data on the nickel nanowire show that at 75- 300 K, it follows the Wiedemann-Franz law, whereas the agreement break down below 75 K indicating that the thermal current is more suppressed than the electrical current in the one dimension system.

誌謝

　　論文完成了，接下來才是最困難的部份，要把所有我在中央研究院物理所這八年中所有該感謝的人一一列出，並將對他們的感謝之語寫下來，內容可能比論文本文還長！回憶八年前，為了拓展自己科學研究的寬度，離開了中山大學物理所，也離開了周雄老師的保護傘，帶著忐忑不安的心來到物理所陳洋元老師的實驗室，首先面對的是完全不同的人際關係、以及新的實驗設備，面臨的是極度嚴酷的挑戰，幸運的是有老師的支持-在生活上，老師盡可能的照顧大家並且給予我們最好的福利，在實驗上，不免要求嚴格。而這正是從事科學研究最重要的基本精神-在該謹慎的地方要求嚴謹，也才是迫使一個人蛻變的真實力量，而我就是在這樣開放又嚴謹的環境下學習科學。之後在陳老師的鼓勵下進入交通大學電子物理所攻讀博士班，這段期間在陳洋元及楊宗哲老師的諄諄教誨下，使我在各方面均有長足的進步，過去八年，不僅在物理知識上收穫豐實，並培養了積極與樂觀的研究態度，老師們對我的影響深遠，在這裡，由衷地再跟兩位老師說聲感謝。

　　在這幾年的漫長時間裡，經歷了許多人生的大事，結婚、兩個小孩的出生，這一切都不是我個人的力量足以承擔的，很感謝老師們這段期間給予我最大的支持及體諒，更要感謝爸、媽、大妹、小妹以及整個家族給我的支持，雖然遇到了很多困難，但也總算有驚無險的度過了，更感謝文娟及我的岳父母，不辭辛勞的為我照顧兩個頑皮的小孩，也感謝兩個可愛的小孩昱辰、昱謙，在爸爸為實驗及課業憂煩時帶給我歡樂，而這些人的支持是讓我繼續走向科學研究之路最大的助力。當然不能忘記在奈米材料與低溫物理實驗室一起工作的夥伴，要感謝的人很多，尤其在與王昌仁博士共事的幾年，讓我學習到許多的實驗技術，也要感謝董崇禮博士及何建民教授為我修改文章，特別是何老師超導領域豐富的閱歷，擴展了我的研究領域。感謝陳正龍在成長孔洞氧化鋁材料上的專業協助，尤其是他的

Contents

Tables

Figures

Chapter 1

Introduction

Metal and semiconductor nanowires (NW) exhibit much different behaviors from those of the bulk, because of quantum confinement and surface effects, distribution of electron energy states, diameter dependence of band gap, enhanced surface scattering of electrons and phonons, large surface to volume ratio and large aspect ratio. Some of their unique mechanical, electrical, magnetic and thermal properties make them become fundamental building blocks for both nano-science and nano-technology in electronic and magnetic materials, as well as biologic sensor and recording media. Consequently, nanowires become an important one-dimensional system in research.

Ferromagnetic NW arrays have attracted special attention owing to their great potential applications in high density magnetic storage media, high sensitivity magnetic sensor and biologic technology [1-4]. For example, perpendicular magnetic recording (PMR) of nanowire arrays could overcome the thermal instability limit of superparamagnetism. Modern magnetic storage devices made by these materials can have bit densities in excess of 100 Gbit/in^2 [5-7]. Indeed, extensive research has been focused on magnetic nanowires in recent years [8-15] for their great importance on the production of magnetic devices. In this required, better understanding of their magnetism, electrical transport and fundamental low-dimensional properties is a pressing issue.

Also relevant to this work is the development of thermoelectric materials, which

convert the heat energy to electric power. The energy conversion efficiency of thermoelectric materials is judged by a figure-of-merit,

$$ZT = \frac{S^2 \sigma}{\kappa_L + \kappa_e} T$$
$$= \frac{S^2}{(\frac{\kappa_L}{ne\mu}) + L_0 T} T \quad , \qquad (1.1)$$

where n, S, L_0, e, κ_L, κ_e and σ are the carrier density, seebeck coefficient, Lorenz number, electronic charge, lattice thermal conductivity, electronic thermal conductivity and electrical conductivity, respectively. Clearly, the transports properties of nanowires are critically important to enhance dominate the efficiency of thermoelectric materials.

The characteristic transport properties of nano-crystalline materials are sensitive to the number of interfaces, random atomic arrangements, impurities, and defects. In consequence, the effective number of conduction electrons are limited to those, which pass or tunnel through all the boundaries along the mean free path (*mfp*), resulting in additional resistivities [16-18]. The grain size and transverse dimensions in nanowires are comparable to *mfp* leading to the enhanced contribution of normal (N-processes) electron-phonon and electron-electron scattering at low temperatures [19], because in this case each scattering is followed by a collision with the surface. There is also a considerable s-d scattering in ferromagnets, particularly in Ni [20, 21], which, for its turn, increases the number of N-processes, leading to redistribution of energy between hot and cold electrons. Thus, in nanowires the behavior of charge current may differ from the behavior of heat current, even if the heat carriers are also charged particles, giving rise to the violation of Wiedemann-Franz law (WF). Recently, the behavior of the Lorenz number (L) in disordered systems has become the topic of several theoretical treatments, which suggest the deviation from the WF

law in nonmagnetic granular metals [22, 23], and the correction ΔL of Lorenz number have to be positive. In addition, there are theoretical supports that a decreasing diameter will also cause changes of electron band structure, then the thermopower (Figure 1.1a).

Since, from the microscopic view, understanding of the electron and phonon transport mechanisms in an individual nanowire is important for the study of low-dimensional thermoelectric materials, the size reduction may be a new factor to improve the thermoelectric properties, such as seebeck coefficient (S), electrical conductivity (σ) and thermal conductivity (κ). One experimental result showed that bismuth nanowires experience a semimetal-to-semiconductor transition. Figure 1.1b shows a temperature dependent resistance with varies size of bismuth-nanowire [24]. Moreover, there is a further prediction that the segment nanowires may deeply reduce phonon transport in nanowires. To achieve these object there are two efforts required. The first one is the preparation of one-dimensional materials. The other one is the construction of a transport property measurement system.

For sample preparation, the porous anodic aluminum oxide (AAO) is considered to be a template for growing nanowire because of its high-density and uniformity of pores. This kind of bottom-up method is to fill thermoelectric materials such as bismuth and Bi_2Te_3 into AAO template by chemical electrodeposition, as already demonstrated by several groups. Such a combination of AAO and electrodeposition technique provides a high quality and low cost approach in synthesizing low dimensional materials for both scientific research and applications [25, 26].

Although fabrications of nanowire arrays and their magnetic properties have been widely studied [27-31], magneto transport properties have been seldom reported. Especially, most of transport studies on nanowires focused on electrical resistivity, whereas the knowledge of heat transport suffers from the lack of information. As

the goal to study conductive nanowires, we built a system for thermodynamic and transport properties measurements, based on a so-called "self-heating 3ω method". By using this method, we measured the electrical resistivity, thermal conductivity and specific heat of a single sagging nickel nanowire at the same time.
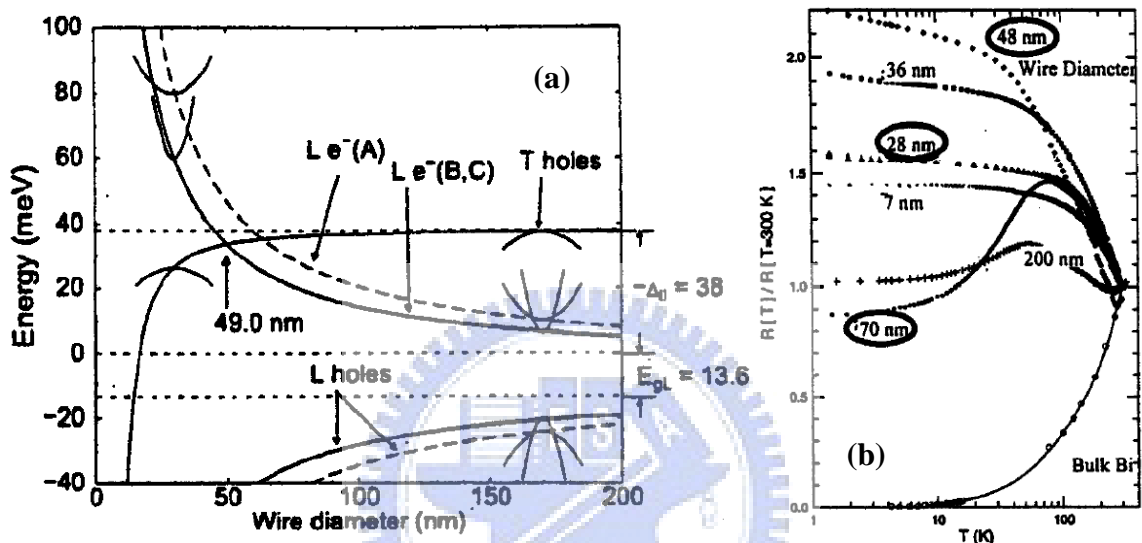
Figure 1.1 (a) Below a certain wire diameter, a semimetal-to-semiconductor transition occurs in Bi-nanowire. (b) Measured temperature dependence of the resistance ratio R(T)/R(300) of Bi-nanowire of various diameter.

4

Chapter 2

Theorem

Introduction

This chapter descripts properties for transports behavior, magnetism, and thermoelectricity. Section 2.1 focuses on transport properties of electrons and phonons, which include (A) Kinetic theory of ideal particles and (B) Thermal conductivity of metals. [32-34]

Section 2.2 gives a common description to magnetism about magnetic materials. Section 2.3 will introduce the thermoelectricity for thermoelectric materials, which include bulk and low-dimensional materials. Mainly, this section will talk about the two important effect, they are Seebeck, and Peltier effect and the definition of favor thermaoelectric parameter: figure-of-merit *ZT*.

2.1   Thermal conduction

Thermal energy can be transmitted through materials via electrical carriers (electrons or holes), phonons (lattice waves), electromagnetic waves, spin waves, or other excitations.   Normally, the total thermal conductivity is the summation of carriers, phonons, and the other components representing various excitations:

$$\kappa = \kappa_e + \kappa_{ph} + \sum \kappa_\alpha \ , \tag{2.1}$$

where α denotes other excitations.   The thermal conductivities of solids vary dramatically in different materials.   This is caused by differences of lattice structure, defects or dislocations of lattice, anharmonic of the lattice vibration, grain sizes for polycrystalline samples and carrier concentrations.   All of these differences will take effects to interactions between the carriers and the phonons and etch other, interactions between magnetic ions and the lattice waves, etc.   These effects make the thermal conductivity an interesting area of study both experimentally and theoretically.   In metals, the major thermal energy carriers are electrical carriers (electrons and holes), while in insulators lattice waves are the dominant heat transporter.

2.1.1　Kinetic theory of ideal particles

To consider a general case, in a thermal nonequilibrium system with ideal particles, the thermal conductivity coefficient κ of gas is defined with respect to the steady-state flow of heat with a temperature gradient:

$$\vec{Q} = -\kappa \cdot \vec{\nabla} T \,, \tag{2.2}$$

where κ, Q, and T are thermal conductivity, heat flow rate, and absolute temperature respectively.

A particle moves in the presented temperature gradient with velocity v, we assume that the heat capacity of this particle is c, its energy must change at a rate of

$$\frac{\partial E}{\partial t} = -c\vec{\upsilon} \cdot \vec{\nabla} T \,. \tag{2.3}$$

The average distance of particles collect with one another is $\upsilon\tau$, where τ is the relaxation time. The average total heat flow rate per unit area summing over all particles is therefore

$$\vec{Q} = -nc\tau \langle \vec{\upsilon} \cdot \vec{\upsilon} \rangle \vec{\nabla} T = -\frac{1}{3} nc\tau\upsilon^2 \vec{\nabla} T \,. \tag{2.4}$$

The brackets in Eq. (2.4) represent an average over all particles. To Combine Eq. (2.2) and (2.4), we have

$$\kappa = \frac{1}{3} nc\tau\upsilon^2 = \frac{1}{3} C\upsilon l \,, \tag{2.5}$$

where $C=nc$ is the total heat capacity and $l=\upsilon\tau$ is the particle mean free path (*mfp*). In solids the same derivation can be made for various excitations (electrons, phonons, etc.). In general, the thermal conductivity is the contributions from all components, the total κ can be

$$\kappa = \frac{1}{3}(C_e \upsilon_e l_e + C_p \upsilon_p l_p + \sum_{\alpha} C_{\alpha} \upsilon_{\alpha} l_{\alpha}) \,, \tag{2.6}$$

where the summation is over all excitations, denoted by α. Equation (2.6) gives a

good phenomenological description of the thermal conductivity, and it is practically very useful for order of magnitude estimates.

Like most of the nonequilibrium transport parameters, thermal conductivity cannot be solved exactly. Calculations are usually based on a combination of perturbation theory and the Boltzmann equation, which are the bases for analyzing the microscopic processes that govern the heat conduction by carriers and lattice waves.

2.1.2   Thermal conductivity of metals

Most metals are solids with crystal structure where the ions occupy translational equivalent positions to form 3-dimensional lattice structure in the crystal.   Thermal energy could be transported via lattice vibration in crystal structure when a temperature gradient is imposed on the structure.   In metals, the heat conduction associated with the vibrations of the lattice called phonon thermal conductivity, κ_p. Meanwhile, the periodic arrays of ions construct a condition, in which the free electrons could transport freely in the lattice structure.   These electrons are responsible not just for the transport of charge but also for the transport of heat. Their contribution to the thermal conductivity is referred to as the electronic thermal conductivity κ_e.   In discussions of the heat transport in metals, one makes an implicit and essential assumption that the electrons and phonons are independent entities. They are described by their respective unperturbed wave functions, and any kind of interaction between the charge carriers and lattice vibrations enters the theory subsequently in the form of transitions between the unperturbed states. This suggests that one can express the overall thermal conductivity of metals as consisting of two

independent terms, the phonon contribution and the electronic contribution:

$$\kappa = \kappa_e + \kappa_p . \qquad (2.24)$$

These two electrons and phonons are certainly the main heat carrying entities.

In fact, in metals such as gold, silver, copper, and aluminum, the heat current associated with the flow of electrons by far exceeds a small contribution due to the flow of phonons.   Thus, for practical purposes, the thermal conductivity can be taken as that due to the charge carriers.   For high impurity metals the electronic term is less dominant, and one has to take into account the phonon contribution in order to properly assess the heat conducting potential of such materials.   It is known that there are some other possible excitations in the structure of metals, such as spin waves, that may, under certain circumstances, contribute a small additional term to the thermal conductivity.   For simplification, we shall not consider these small and often conjectured contributions.   In the following selections, the transport of electrons and phonons would be discussed, respectively.   Table 2.1 presents thermal and electrical conductivities of familiar metals together with their Lorenz ratio, all referring to a temperature of 273 K.
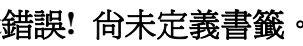
TABLE 2.1 Thermal conductivities of pure metals at 273 K. [34]

Metal	κ (W/m-K)	ρ (10^{-8} Ωm)	L (10^{-8} V^2/K^2)	Ref.
Ag	436	1.47	2.34	11
Al	237	2.43	2.10	12
Au	318	2.03	2.39	13
Ba	23.3	29.8	2.55	14
Be	230	2.8	2.36	15
Ca	186	3.08	2.13	16
Cd	100	6.80	2.49	15
Ce	11.2 (291 K)	80.0	~ 3.5	17
Co	99 (300 K)	5.99	1.98 (300 K)	18
Cr	95.7 (280 K)	11.8	4.11	19
Cs	37 (295 K)	18.0	2.5 (295 K)	20
Cu	402 (300 K)	1.73 (300 K)	2.31 (300 K)	21
Dy	10.4 (291 K)	93	3.75 (291 K)	22
Er	13.8 (291 K)	79	3.75 (291 K)	22
Fe	80.2 (280 K)	8.64	2.57 (280 K)	23
Ga ($\parallel c$)	16.0	50.3	2.95	19
($\parallel a$)	41.0	16.1	2.41	19
($\parallel b$)	88.6	7.5	2.43	24
Gd	9.1 (291 K)	128	4.2 (291 K)	22
Hf	22.4 (293 K)	31.0 (293 K)	2.45 (293 K)	25
Hg ($\parallel$)	34.1 (197 K)	14.6 (197 K)	2.53 (197 K)	26
($\perp$)	25.9 (197 K)	19.3 (197 K)	2.55 (197 K)	26
Ho	11.8 (300 K)	78.0 (300 K)	3.2 (300 K)	27
In	81.0 (280 K)	8.25 (280 K)	2.39 (280 K)	28
Ir	149 (277 K)	4.70	2.57 (277 K)	29
K	98.5	6.20	2.24	30
La	14.0 (291 K)	59	2.9	22
Li	65	8.5	2.05	31
Lu	16.2 (291 K)	~ 50	3.3 (291 K)	22
Mg	153 (301 K)	4.5 (301 K)	2.29 (301 K)	32
Mn (α)	7.8 (291 K)	137	4.0 (291 K)	22
Mo	143	4.88	2.56	33
Na	142	4.29	2.23	34
Nb	51.8 (280 K)	13.3	2.53 (280 K)	35
Nd	16.5 (291 K)	58	3.7 (291 K)	22
Ni	93 (280 K)	6.24	2.19 (280 K)	36
Os	87 (323 K)	8.3	2.7 (323 K)	29
Pb	35.5	19.2	2.50	37
Pd	71.7	9.74	2.57	38
Pr	12.8	65	3.1 (280 K)	39
Pt	71.9 (280 K)	9.82	2.59 (280 K)	23
Pu	5.2 (298 K)	~ 130	2.48 (298 K)	40
Rb	55.8	11.3	2.30	41
Re	49	16.9	3.05	42
Rh	153 (280 K)	4.35	2.46 (280 K)	43
Ru	110 (280 K)	6.7	2.72 (280 K)	43
Sc	21.8	44	4.3	44
Sm	13.4 (291 K)	90	4.3 (291 K)	22
Sn	64	10.6	2.48	15
Sr	51.9	11.0	2.18	14
Ta	57.7 (280 K)	12.1	2.56 (280 K)	45
Tb	10.4 (291 K)	110	4.25 (291 K)	22
Tc	51 (300 K)	16.7	~ 3.4 (300 K)	46
Th	49.3	13.9	2.56	47
Ti	22.3	40	3.25	48
Tl	50.6	15	2.8	49
U	28 (278 K)	24	2.8 (278 K)	50
V	35 (260 K)	18.9	2.4 (260 K)	51
W	183 (280 K)	4.85	3.27 (280 K)	23
Y	15.9 (291 K)	~ 52	2.9 (291 K)	22
Zn	114.5 (283 K)	5.5	2.31 (283 K)	52
Zr	20.5 (323 K)	39	3.4 (323 K)	53
As (pc)	27 (298 K)	31.7 (298 K)	2.87 (298 K)	54
($\perp c$-axis)	51.0 (300 K)	28.4 (300 K)	4.83 (300 K)	55
($\parallel c$-axis)	29.0 (300 K)	38.6 (300 K)	3.73 (300 K)	55
Bi (pc)	7.8 (298 K)	148 (298 K)	3.87 (298 K)	56
($\perp c$-axis)	9.8 (300 K)	112 (300 K)	3.65 (300 K)	57
($\parallel c$-axis)	6.0 (300 K)	135 (300 K)	2.69 (300 K)	57
Sb	18.2	43	2.87	58

Electronic thermal conduction

For the free electron theory in solids, we consider each electron as an ideal particle. These particles move in a periodic potential produced by the ions and other electrons without interaction, and then regards the deviation from the periodicity due to the vibrations of the lattice as a perturbation. The values of the electron wave vector $\vec{k}$ depend on the periodicity and the size of the crystal. The electron energy $E_{\vec{k}}$ depends on the form of the potential and is a continuous function of $\vec{k}$ in a Brillouin zone, but it is discontinuous at the zone boundaries. According to Fermi-Dirac distribution, the equilibrium distribution function $f_{\vec{k}}^0$ of electrons in the state $\vec{k}$ is given by

$$f_{\vec{k}}^0 = \frac{1}{\exp(\dfrac{E_{\vec{k}} - E_F}{k_B T}) + 1},$$

(2.7)

where E_F and k_B are the Fermi energy and Boltzmann's constant, respectively. For Boltzmann's equation, in the presence of an electrical field $\vec{E}$ and a temperature gradient $\vec{\nabla} T$, the steady state that represents a balance between the effects of the scattering processes, the external field and temperature gradient. The expressions for the current density $\vec{J}$ and the heat錯誤! 尚未定義書籤。 $\vec{Q}$ are

$$\vec{J} = \int e \vec{v}_{\vec{k}} f_{\vec{k}} d\vec{k}$$

(2.8)

and

$$\vec{Q} = \int (E_{\vec{k}} - E_F) \vec{v}_{\vec{k}} f_{\vec{k}} d\vec{k}.$$

(2.9)

Here we define an integral function K_n as

$$K_n = -\int \vec{v} k_{\vec{k}}^2 \tau(k)(E_{\vec{k}} - E_F)^n \frac{\partial f_{\vec{k}}^0}{\partial E_{\vec{k}}} d\vec{k}.$$

(2.10)

Thus Eqs (2.8) and (2.9) can be written as [34]

$$\vec{J} = e^2 K_0 \vec{E}_{eff} - \frac{e}{T} K_1 \vec{\nabla} T \qquad (2.11)$$

and

$$\vec{Q} = e K_1 \vec{E}_{eff} - \frac{1}{T} K_2 \vec{\nabla} T , \qquad (2.12)$$

respectively.   As $\vec{J} = 0$, the electronic thermal conductivity can be simplified as

$$\kappa_e = -\left.\frac{\vec{Q}}{\vec{\nabla} T}\right|_{\vec{J}=0} = \frac{1}{T}\left(K_2 - \frac{K_1^2}{K_0} \right). \qquad (2.13)$$

And from Eq. (2.11), the electrical conductivity σ can be derived as

$$\sigma = e^2 K_0 . \qquad (2.14)$$

Since $\partial f_{\vec{k}}^0 / \partial E_{\vec{k}}$ is approximately a delta function at the Fermi surface with width $k_B T$,

K_n can be evaluated by expansion.   Therefore we observe

$$K_2 = \frac{\pi^2}{3} \frac{k_B^2 T^2}{e^2} \sigma(E_F) + O\left(\frac{k_B T}{E_F}\right)^2 , \qquad (2.15)$$

and

$$\frac{K_1^2}{K_0} \approx O\left(\frac{k_B T}{E_F}\right)^2 . \qquad (2.16)$$

Thus Eqs. 2.13 can be derived into the Wiedemann-Franz law with the standard

Lorentz number L_0 as

$$L_0 = \frac{\kappa_e}{\sigma T} = \frac{\pi^2 k_B^2}{3 e^2} = 2.45 \times 10^{-8} W \cdot \Omega / K^2 . \qquad (2.17)$$

From this free electron gas model, the Lorenz number is totally a calculation of

physics constants.   This implied that pure metals should have the same electronic

thermal conductivity to electrical conductivity ratio, and this ratio is proportional to

the absolute temperature.   Furthermore, for strong degenerate electron gases, Eq.

(2.17) is independent of the scattering mechanism and the band structure for the

electrons as long as the scatterings are elastic. The Wiedemann-Franz law is generally well obeyed at high-temperatures. However, the law fails at low- and intermediate-temperature due to the enhanced inelastic scattering of the charge carriers. Over a wide temperature range, scattering of electrons by phonons is a major factor for determining the electrical and electronic thermal conductivities. The resistance due to this type of scattering is called the ideal resistance. The ideal electrical and electronic thermal resistances can be approximately written as

$$\rho_i = \frac{1}{\sigma_i} = A \left(\frac{T}{\theta_D} \right)^5 J_5 \left(\frac{\theta_D}{T} \right) \tag{2.18}$$

and

$$W_i = \frac{1}{\kappa_i} = \frac{A}{L_0 T} \left(\frac{T}{\theta_D} \right)^5 J_5 \left(\frac{\theta_D}{T} \right) \left\{ 1 + \frac{3}{\pi^2} \left(\frac{k_F}{q_D} \right)^2 \left(\frac{\theta_D}{T} \right)^2 - \frac{1}{2\pi^2} \frac{J_7 \left(\theta_D/T \right)}{J_5 \left(\theta_D/T \right)} \right\}, \tag{2.19}$$

where

$$J_n \left(\frac{\theta_D}{T} \right) = \int_0^{\theta_D/T} \frac{x^n e^x}{\left(e^x - 1 \right)^2} dx, \tag{2.20}$$

$$A = \frac{3\pi \hbar q_D^6 \left(G' \right)^2}{4 e^2 \left(m^* \right)^2 n_c k_B \theta_D k_F^2 \upsilon_F^2}, \tag{2.21}$$

θ_D is the Debye temperature for phonons, k_F is the electron wave number at the Fermi surface, q_D is the phonon Debye wave number, G' is the constant representing the strength of the electron-phonon interaction, n_c is the number of unit cells per unit volume, and υ_F is the electron velocity at the Fermi surface. By combining Eqs. (2.18) and (2.21), at high temperature ($T \gg \theta_D$), as the electron-phonon interaction under consideration, the electronic thermal conductivity is

$$\rho_i = \frac{AT}{4\theta_D}, \tag{2.22}$$

and thermal resistivity is

$$W_i = \frac{A}{4\theta_D L_0} = \frac{\rho_i}{L_0 T} . \tag{2.23}$$

At low temperature ($T \ll \theta_D$), the electronic thermal conductivity is

$$\rho_i = 124.4 A \left(\frac{T}{\theta_D} \right)^5 , \tag{2.24}$$

and thermal resistivity is

$$W_i = 124.4 \frac{A}{L_0 T} \left(\frac{T}{\theta_D} \right)^3 \frac{3}{\pi^2} \left(\frac{k_F}{q_D} \right)^2 . \tag{2.25}$$

In addition to the electron-phonon interaction, the electron-defect interaction contributes to the electrical resistivity and electronic thermal resistivity. According to Matthiessen's rule, the resistivity ρ and the electronic thermal resistivity W_e is

$$\rho = \frac{1}{\sigma} = \rho_0 + \rho_i \tag{2.26}$$

and

$$W_e = \frac{1}{\kappa_e} = W_0 + W_i , \tag{2.27}$$

where ρ_0 and W_0 are the residual electrical resistivity and electronic thermal resistivity, respectively, due to the electrons scattered by impurities and defects. At very low temperature, the electronic thermal conductivity

$$\kappa_e \approx \frac{1}{W_0} = \frac{L_0 T}{\rho_0} . \tag{2.28}$$

is linear dependence of temperature. The Wiedemann-Franz law hold at very high and very low temperature as shows in Figure 2.1. In alloys or metals with a high concentration of defects, electron-defect and electron-phonon interaction only become comparable at high-temperatures. In this case, there is no maximum in the κ_e, versus, T curve, and κ_e will approach the high-temperature constant monotonically as T increases. Both cases are illustrated in Figure 2.2, which shows the low temperature thermal conductivity of silver [34].
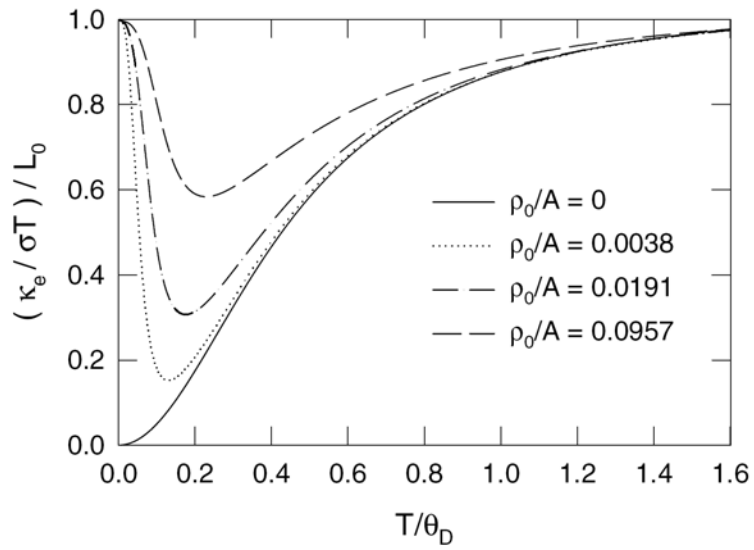
Figure 2.1 Temperature dependence of normalized Lorenze number for monovalent metals.
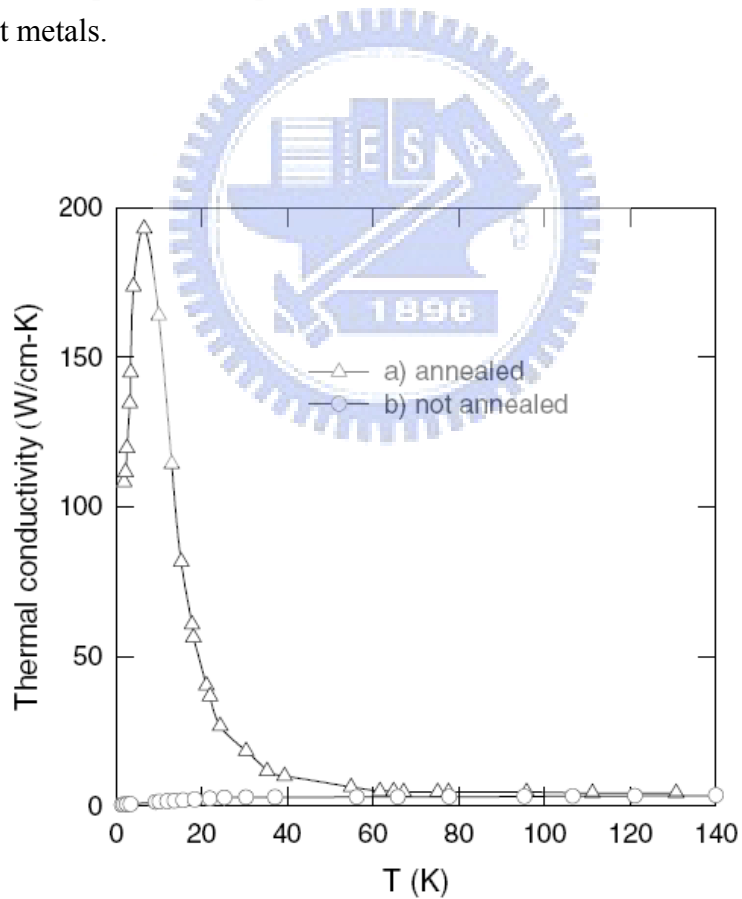
Figure 2.2 Thermal conductivity of very low and high residual resistivity silver, showing the influence of the residual resistivity on the low-temperature thermal conductivity.

Lattice thermal conduction

Lattice thermal conduction is the dominant thermal conduction mechanism in nonmetals, if not the only one. In solids, lattice vibrations are an essential feature of all crystalline material, atoms vibrate about their equilibrium positions. Even in some semiconductors and alloys, it dominates a wide temperature range. The vibrations of atoms are not independent of each other, but are rather strongly coupled with neighboring atoms. The crystal lattice vibration can be characterized by the normal modes, or standing waves. The quanta of the crystal vibration field are referred to as "phonons", a kind of ideal particle. Phonon dispersion curves for solids normally consist of acoustic and optical branches. Schematic phonon dispersion curves for monatomic and diatomic lattices are shown in Figure 2.3.
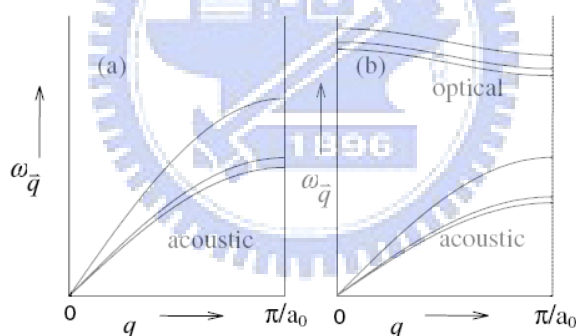
Figure 2.3 Schematic phonon dispersion curves for a given direction of $\bar{q}$ of (a) monatomic lattice and (b) diatomic lattice. The lattice parameter is denoted a_0.

The low-frequency acoustic branches correspond to atoms in a unit cell moving in same phase, whereas the high-frequency optical branches represent atoms in a unit cell moving in opposite phases. In the presence of a temperature gradient, the thermal energy is considered as propagating by means of wave packets consisting of various normal modes, or phonons. So, from this point of view, we could treat transport of lattice vibration as interaction of particles, collision of phonons. There are two collision-process, they are the *N*ormal and *U*mklapp processes. As the *N*

process ($K_1+K_2=K_3$) occur, where the K_1, K_2, and K_3 are the momentum of three collision phonons, the phonon flux is unchanged in momentum on collision. Therefore there is no thermal resistance in this kind of elastic collision. The other one is U process, the important three-phonon processes that cause thermal resistivity are of the form $K_1+K_2=K_3+G$, where G is a reciprocal lattice vector. As temperature higher than Debye temperature (θ_D), all phonon collisions will then be U processes, with the attendant high momentum change in the collision. In this regime we can estimate the thermal resistivity without particular distinction between N and U processes. At high temperature the lattice thermal resistivity is linear dependence of temperature. [32]

2.2   Magnetism

Paramagnetism

The orientations of magnetic moments in paramagnetic materials are random and they are independent to each other.   We could consider the total magnetic moment of a paramagnetic material as an atom or ion in free space.   The magnetization should proportion to the external applied field, and obey the Curie law [1, 2]. Paramagnets do not retain any magnetization in the absence of an externally applied magnetic field, because thermal motion causes the spins to become randomly oriented. Thus the total magnetization will drop to zero when the applied field is removed. Even in the presence of the field there is only a small induced magnetization because only a small fraction of the spins will be oriented by the field.   Paramagnetic materials possess a quite small positive magnetic susceptibility (χ), which is less than 10^{-5}, normally.

Ferromagnetism

It is well known that ferromagnets expose to a magnetic field they retain the magnetization even the field is removed.   Ferromagnet was used for any material that could exhibit spontaneous magnetization: a net magnetic moment in the absence of an external magnetic field.   In particular, a material is "ferromagnetic" in this narrower sense only if all of its magnetic ions add a positive contribution to the net magnetization. If some of the magnetic ions subtract from the net magnetization, then the material is "ferrimagnetic".   If the ions anti-align completely so as to have zero

net magnetization, despite the magnetic ordering, then it is an antiferromagnet.   All of these alignment effects only occur at temperatures below a certain critical temperature, called the Curie temperature for ferromagnets and ferrimagnets or the Néel temperaturefor antiferromagnets. The most common way to represent the magnetic properties of a ferromagnetic material is by a plot of magnetization M against H, as shows in Figure 2.4 [32].
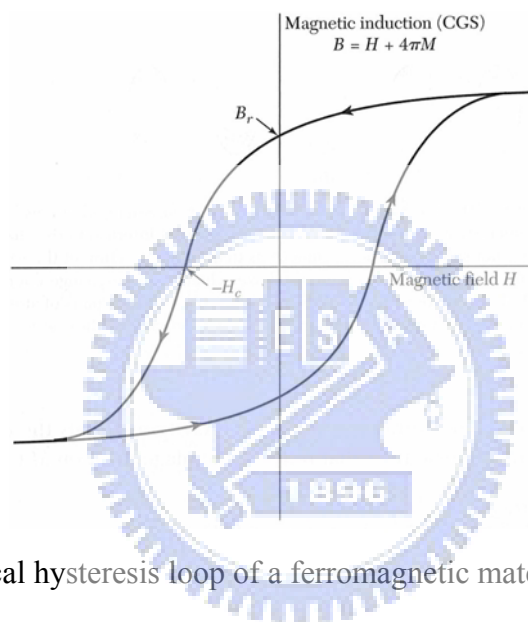
Figure 2.4 A typical hysteresis loop of a ferromagnetic material.

2.3　Thermoelectricity

In the three decades from 1821 to 1851, the basic effects were discovered and understood macroscopically, and their applicability to thermometry, power generation, and refrigeration was recognized. The sole lasting contribution in the next 80 years was Altenkirch's derivation of thermoelectric efficiency in 1911.　Then in the late 1930s, there began 20 years of progress (figure 2.6) that lead to a microscopic understanding of thermoelectricity and the development of today's materials [35].

The topic of thermal-electric energy conversion phenomena were studied over two century.　The thermoelectric effect provides a means by which thermal energy can be converted into electricity can be used for heat pumping or Power generation. Especially, the solid state cooling and power generation devices which based on thermoelectric effects have been investigated since the Seebeck and Peltier effect were discovered [36, 37].
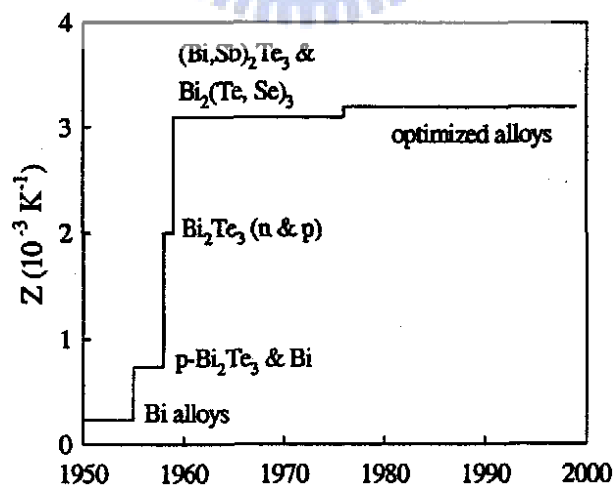
Figure 2.5 Progress in the figure of merit of thermoelectric materials at room temperature.

Seebeck effect

The Seebeck effect was first presented by Thomas Johann Seebeck in 1821. This phenomenon related with the generation of a voltage along a conductor when it is subjected to a temperature gradient. Chemical potential cause carriers (electrons or holes) diffuse from the hot side to the cold side, creating an internal electric field that opposes further diffusion. The Seebeck coefficient is defined as the voltage generated per degree of temperature difference between two ends (figure 2.7a).

$$S = -\frac{\delta V}{\delta T}, \qquad\qquad (2.30)$$

Peltier effect

The Peltier effect is the reverse of the Seebeck effect and observed in 1834 by Jean Peltier. The Peltier effect describes a phenomenon that carriers carry heat when they flow through a conductor. The heat current I_Q is proportional to the current I and the proportionality constant Π is called the Peltier coefficient (figure 2.7b).

$$I_Q = \Pi \bullet I, \qquad\qquad (2.31)$$
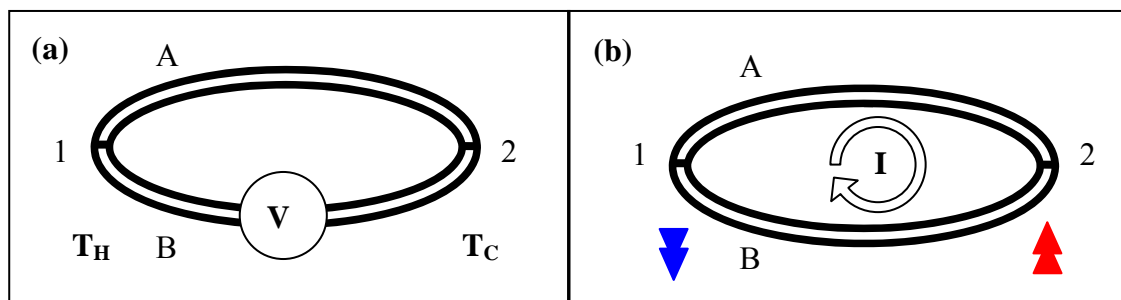
Figure 2.6 Definition of the thermaoelectric effects. The conductors A and B are joined at junctions 1 and 2. (a) If these junctions are at different temperature, a Seebeck voltage appears across an opening in one of the conductor. (b) If a current is passed, there is Peltier cooling at one junction and Peltier heating at the other.

A thermoelectric EMF is created in the presence of a temperature difference between two different materials. This usually causes a continuous current to flow in the conductors. The voltage is on the order of hundred and several microvolts per degree in semiconductor and metal, respectively. As two materials are joined together, there will be an excess or deficiency in the energy at the junction. The energy difference make the junction either absorb or emit heat, causing heating or cooling. The Seebeck and the Peltier coefficients are related through the Kelvin relation $\Pi=ST$, where T is the absolute temperature. A commercial thermoelectric device is shown in Figure 2.8a, which made of many pairs of p–n legs. P-type and n-type semiconductor elements are welded in the top and bottom sides, such that a current flows through all the elements in series, while the energy they carry leaves the cold or hot side in parallel. The thermoelectric power generator and cooler work in reverse, which shown in Figure 2.8b and 2.8c, respectively. For example, in a power generator the hot side has a higher temperature, electrons and holes are driven to the cold side through diffusion and flow through an external load to do useful work.

(a)

N P N P N P N P

(b)

(c)

Loading
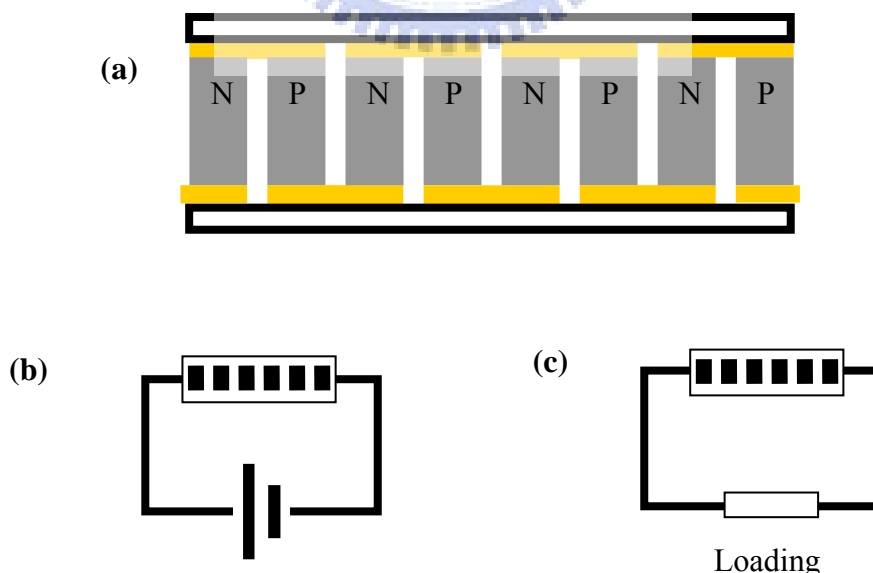
Figure 2.7 (a) The actual commercial thermaoelectric device. (b) and (c) are the cooler and power generator, respectively.

The heat energy to electrical power conversion efficiency for a given thermocouple varies with the resistance of the load. Ioffe (1957) showed that the highest efficiency is given by

$$\eta = \frac{(T_H - T_C)}{T_H} \frac{(1 + ZT)^{0.5}}{T_C / T_H + (1 + ZT)^{0.5}} ,$$ (2.32)

where T is taken to be equal to $(T_H + T_C)/2$, and the quantity Z, which is known as the figure of merit of the thermocouple. The performance of thermoelectric device depends on the figure of merit (ZT) of the material, given by

$$ZT = \frac{S^2 \sigma}{\kappa} T ,$$ (2.33)

where S, T, σ and κ are the Seebeck coefficient, absolute temperature, electrical conductivity and thermal conductivity, respectively. From an intuitional view, the reason that the electrical conductivity σ enters Z is due to Joule heating. The thermal conductivity κ appears in the denominator of Z because, in thermoelectric coolers or power generators, the thermoelectric elements also act as the thermal insulation between the hot and the cold sides. The main research issue in thermoelectric materials is to increase power factor (mutilation of $S\sigma$) and decrease thermal conductivity (κ) to cause a large figure of merit.

In the recent two decades, environment-protection concepts lead to renewed activity in the science and technology of alternative energy. The directly usage of solar energy is an important issue. There are two accepted proposes for develop the solid-state energy converter, they are photonic-electric and thermal-electric effects.

The thermal-electric effect related phenomena were observed and studied for a long time. Closely related cooling and power generation mechanisms, thermomagnetic effects and themionic emission, are less well established but may soon have their day.

In bulk materials, the quantities S, σ and κ are inter-related, so that the figure of merit, ZT, is difficult to increase in conventional 3D crystalline systems. For a long time, materials with ZT ~1 were accepted limit of ZT. But the new variable of size gives rise to differences in the density of electronic states, allowing new opportunities to vary S, σ and κ independently. The common picture of dimensional-dependent band structure is shown in figure 2.5. As the dimension decreases from 3D crystalline solids to 2D (quantum wells) to 1D (quantum wires) and finally to 0D (quantum dots), new physical phenomena are introduced and new opportunities to vary S, σ and κ independently.
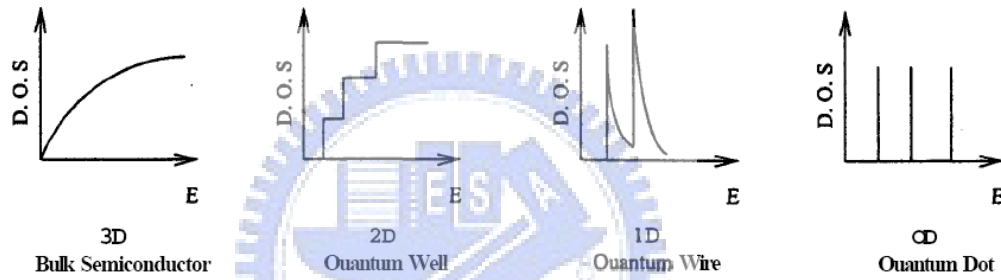
Figure 2.8 Electronic density of states for (a) bulk 3D crystal, (b) 2D quantum well, (c) 1D nanowire and (d) 0D quantum dot.

There are three generic approaches have been proposed to date for low-dimensional materials, which described in ref.4. (1) quantum-confinement effects [38]: to enhance density of states near the Fermi energy. Using such effects, a ZT of 0.9 at 300 K and 2.0 at 550 K, using estimated thermal-conductivity values, has been reported [39] in $PbSe_{0.98}Te_{0.02}/$ PbTe quantum-dot structures. (2) phonon-blocking-electron-transmitting superlattices: These structures utilize the acoustic mismatch between the superlattice components to reduce κ_L [40-42], thereby potentially eliminating alloy scattering of carriers. (3) thermionic effects in heterostructures. [43] Furthermore, they also report a ZT at 300 K of ~2.4 in p-type Bi_2Te_3/Sb_2Te_3 superlattices and a ZT ~1.4 in n-type $Bi_2Te_3/Bi_2Te_{2.83}Se_{0.17}$

superlattices.

The low-dimensional materials seem owing a lot of different behavior from bulk materials. This gives us the motivation to investigate on electronic and thermodynamic behavior for understanding the fundamentals in nano-physics. In the recent two decades, environment-protection concepts lead to renewed activity in the science and technology of alternative energy. The directly usage of solar energy is an important issue. There are two accepted proposes for develop the solid-state energy converter, they are photonic-electric and thermal-electric effects.

The thermal-electric effect related phenomena were observed and studied for a long time. Closely related cooling and power generation mechanisms, thermomagnetic effects and themionic emission, are less well established but may soon have their day.

Chapter 3

Experimental facilities and measurement methods

Introduction

This chapter introduce equipments for study the samples. Section A of 3.1 gives a bright description of X-ray diffraction (XRD) technique for characterizing the lattice structure of nanowires by the x-ray powder diffraction method. Section B of 3.1 gives the description of Scanning electron microscope (SEM) for determining and observing the geometry dimensions and morphology of samples, respectively. Section C of 3.1 talks about the sample temperature control system.

The last decays have seen significant developments in thin-film thermal conductivity measurement techniques. However, the characterization of the thermal conductivity of a nanowire remains a challenging task. Usually, thermal conductivity measurements are difficult to make with relatively high accuracy, certainly better than within 5%. Sections of 3.2 descript the methods for us to study the electronic and thermal conductivity. Section A of 3.2 introduces the four-probe method for resistivity measurement. Section B and C of 3.2 gives the detail description for Self-heating 3ω method and Construction of measurement system & sample holder, respectively.

3.1   Introduction to experimental equipments

3.1.1   X-ray diffraction (XRD)

X-ray diffraction (XRD) is a non-destructive technique that reveals detailed information about the crystallographic structure of natural and manufactured materials. It's now a common technique for the study of crystal structures and atomic spacing. When a monochromatic X-ray beam with wavelength λ is projected onto a crystalline material at an angle θ, diffraction occurs only when the distance traveled by the rays reflected from planes differs by a complete number n of wavelengths when conditions satisfy Bragg's Law ($n\lambda=2d \sin \theta$). This law relates the wavelength of electromagnetic radiation to the diffraction angle and the lattice spacing in a crystalline sample. Conversion of the diffraction peaks to d-spacing allows identification of materials. By varying the angle, the Bragg's Law conditions are satisfied by different d-spacings in polycrystalline materials. Based on the principle of X-ray diffraction, a wealth of structural, physical and chemical information about the material investigated can be obtained. A host of application techniques for various material classes is available, each revealing its own specific details of the sample studied.

The specific wavelengths are characteristic of the target material (Cu, Fe, Mo, Cr).   The geometry of an X-ray diffractometer is such that the sample rotates in the path of the collimated X-ray beam at an angle θ while the X-ray detector is mounted on an arm to collect the diffracted X-rays and rotates at an angle of 2θ. The instrument used to maintain the angle and rotate the sample is termed a goniometer.   X-ray powder diffraction is the method used for the identification of unknown crystalline materials. In our results, the XRD is performed by the PANalytical X'Pert PRO analysis system.

3.1.2　　Scanning electron microscope (SEM)

The scanning electron microscope (SEM) is a type of electron microscope that images the sample surface by scanning it with a high-energy beam of electrons in a raster scan pattern. The electrons interact with the atoms that make up the sample producing signals that contain information about the sample's surface topography, composition and other properties such as electrical conductivity.

The types of signals produced by an SEM include secondary electrons, characteristic x-rays, specimen current and transmitted electrons. These types of signal all require specialized detectors for their detection that are not usually all present on a single machine. The signals result from interactions of the electron beam with atoms at or near the surface of the sample. In the most common or standard detection mode, secondary electron imaging or SEI, the SEM can produce very high-resolution images of a sample surface, revealing details about 1 to 5 nm in size. Due to the way these images are created, SEM micrographs have a very large depth of field yielding a characteristic three-dimensional appearance useful for understanding the surface structure of a sample. This is exemplified by the micrograph of pollen shown to the right. A wide range of magnifications is possible, from about x 25 (about equivalent to that of a powerful hand-lens) to about x 250,000, about 250 times the magnification limit of the best light microscopes.　Characteristic X-rays are emitted when the electron beam removes an inner shell electron from the sample, causing a higher energy electron to fill the shell and release energy. These characteristic x-rays are used to identify the composition and measure the abundance of elements in the sample.　The morphology and geometry dimensions of our samples are determined with models Hitachi S-4200 FESEM and Horeba EX-220 energy dispersion spectroscopy.

3.1.3   Magnetic Property Measurement System (MPMS)

The Quantum Design MPMS provides solutions for a unique class of sensitive magnetic measurements in key areas such as high-temperature superconductivity, biochemistry, and magnetic recording media.   The modular MPMS design integrates a Superconducting Quantum Interference Device (SQUID) detection system, a precision temperature control unit residing in the bore of a high-field superconducting magnet, and a sophisticated computer operating system. Powerful software controls measurements, making data collection and analysis quick and easy.

3.1.4   Physical Property Measurement System (PPMS)

The Quantum Design PPMS represents a unique concept in laboratory equipment: an open architecture, variable temperature-field system, designed to perform a variety of automated measurements.   Use the PPMS with options designed for it or easily adapt it to your own experiments.   Sample environment controls include fields up to ± 5 Tesla and temperature range of 1.8 - 400 K. Its advanced expandable design combines many features in one instrument to make the PPMS the most versatile system of its kind.

3.1.5　Cryostat system

The construction for temperature control system include three main parts, the OXFORD Heliox series ^{3}He refrigerator, sample holder, and control device.　The figure below represents a schematic of the.　The ^{3}He refrigerator insert can be treated like any sample rod for a variable temperature insert.　Once loaded, the insert is cooled from 300K down around 70K using exchange gas.　The ^{3}He gas contained in a small dump sitting on top of the insert is then condensed at around 1.5K.　Once the ^{3}He pot has reached a stable temperature and condensation is completed, the adsorption pump will start to cool the ^{3}He pot and experimental set-up to below 300 mK.　The condensation and the cool down time typically require less than 1 hour. Meanwhile, a homemade sample holder (Figure 3.1) was mounted together with the commercial heater on the ^{3}He pot.　The minimum temperature of this construction is 0.4 K, and in our experience, the temperature of sample can keep at this temperature over 4 hours.　Furthermore, the whole temperature control instruments were monitored by a computer through the interface GPIB.
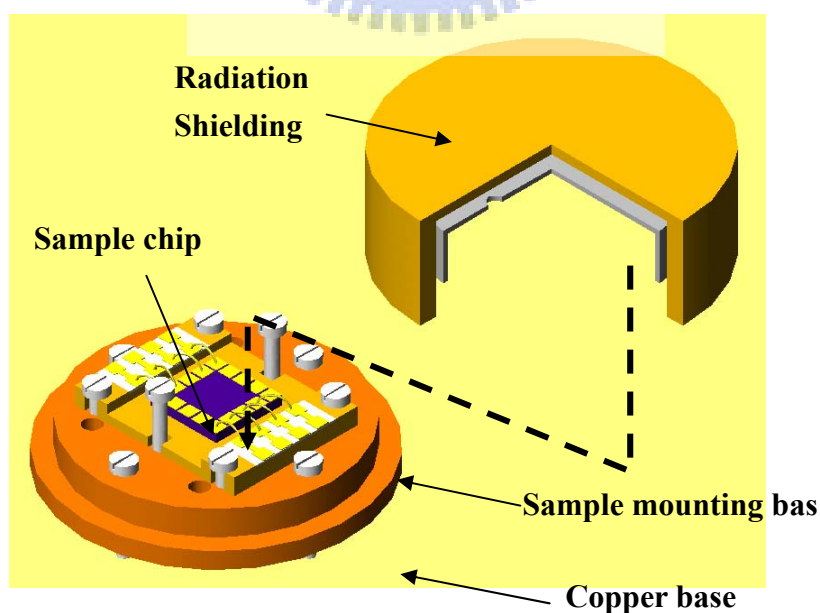
Figure 3.1 The sketch of the homemade sample holder with copper base and two layer shields.

3.2   Electronic property measurement methods

3.2.1   Four-probe method

If you wanted to determine the high precise of a resistance, you would probably connect its two leads up to an Ohmmeter and read off the value. This could be a problem, if the resistance you are trying to measure is very small. A voltage source may damage your sample due to the high passing current. Do you know how much current should we use to measure resistance? For this reason, one often determines the resistance of a sample by passing through it a known current I, measuring the resulting voltage drop ΔV, and performing the division to get $R = \Delta V/I$. This might be a direct current, or it might be an alternating current. The constant-current circuit allows us to determine the sample resistance with a very small current eliminating the possibility of damage to the sample, especially for an ultra fine wire.

We now turn to the other issue, the problem of lead resistance. The sample resistance might be so low that the resistance of the leads running to the sample might be significant by comparison. A related problem is that of contact resistance. Somehow we must connect leads between our sample and the external circuit, and this involves making "contact" to the sample. Contacts are notorious sources of resistance. The situation is illustrated as Figure 3.2a. Let the two contacts to the sample be represented by equivalent resistances R_{C1} and R_{C2}. The measured voltage drop $V = I (R_{C1} + R_S + R_{C2})$. How do we know what fraction of the voltage drop V is due to R and how much is due to the contacts? Fact is we have no way of knowing, because we measure their series combination. This is especially a problem if R_S is much smaller than R_{C1} and R_{C2}. Consequently, the resistance of the leads will be in series with the resistance you are trying to measure, so will of course

include to the reading.

The four-probe method is the most common way to separate out the resistivity of conducting materials. This can be seen by looking at the equivalent circuit, shown in the Figure 3.2b. Two of the probes are used for applied current source and the other two probes are used to measure voltage. By separating the current contacts from the voltage contacts we are able to distinguish the sample resistance from that of the contacts and connecting wires. If the voltmeter has an infinite input impedance, no current will flow through the voltage contacts, and the measured voltage drop V is across the portion of the sample that is between the two voltage contacts. Even if R is much smaller than R_{C1} and R_{C2}, the measured voltage drop is still $V = I R$.
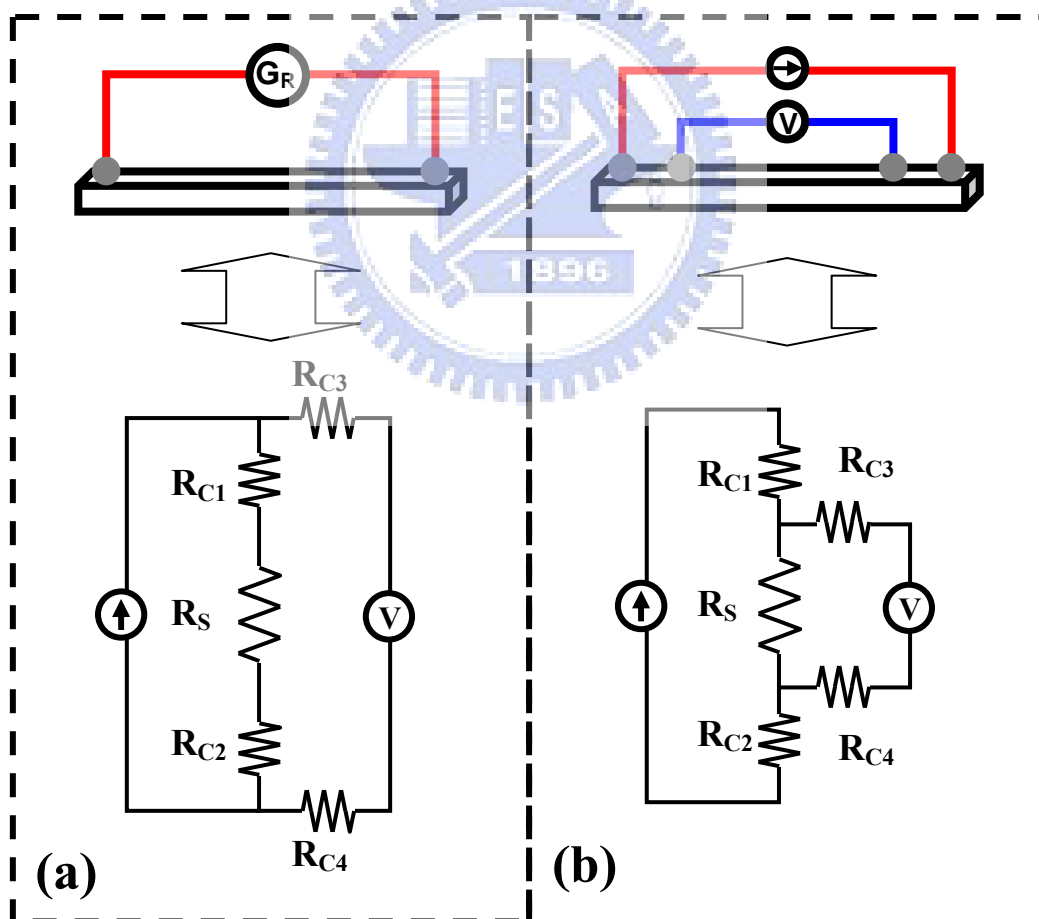
Figure 3.2 The sketch for the conditions of leads connection from sample to instruments and the effective circuits. Inset (a) is the 2-probe method. Inset (b) is the 4-probe method.

Using a Lock-in to Measure Resistance

The voltage drop ΔV is measured with an oscilloscope, high sensitive voltmeter, or better yet, with a lock-in amplifier. If you are trying to measure voltages on the order of microvolt, you should consider using a lock-in amplifier. Lock-in amplifiers are ideal for making low-frequency resistance measurements. The basic idea is to replace the direct current source with an oscillator $I_0 \sin \omega t$, and to replace the voltmeter with a phase-sensitive-detector. Most lock-in amplifiers combine both of these. The oscillator frequency ω is set to some low value, say 13 Hz. The lock-in is set to use its own internal oscillator as the reference for the PSD. The lock-in is calibrated to read ΔV in RMS-voltage so that the sample resistance $R = \Delta V/I = (\Delta V/E_{RMS}) \times R_L$, where E_{RMS} and R_L is the RMS-voltage of the lock-in's oscillator and a series resistor, respectively. In the circuit above there is an oscilloscope connected to the signal monitor output of the lock-in. It is very important to "look" at what it is that you are measuring; never trust the reading without first viewing the signal. The BNC cable connections are "blown up" on the sample box to show the internal wiring of the box. To be sure, all BNC connectors are connected to the BNC cables as expected.

3.2.2 Self-heating 3ω method

Knowledge of the thermal conductivity of thin films, multilayer thin-film, and wires structures is critical for a wide range of applications in microelectronics, photonics, microelectromechanical systems, and thermoelectric materials [44-47]. Some methods developed for the determination or measurement of thermal conductivity of materials, such as the steady-state technique, the 3ω technique, and the thermal diffusivity measurement. [48] Each of these techniques has its own advantages as well as its inherent limitations, with some techniques more appropriate to specific sample geometry, such as the 3ω technique for individual nanowires. For steady-state method, the thermal conductivity of solids is usually determined by measuring the temperature gradient produced by a steady heat flow in a one-dimensional geometry. Direct measurements of the thermal conductivity, for example, typically require the determination of the heat flux and the temperature drop between two points of the sample. Figure 3.3 shows a typical sample configuration of a bulk system. Unfortunately, these techniques often require large, precisely shaped samples and extreme care to be used successfully. From a practical view, it's impossible to achieve this setup for thin-film and nanowire system. In order to study thin-film and nanowire system, a technique was developed to measure thermal properties. One important technique is the 3ω method, which take 3rd harmonic signal to measure the thermal and electrical conductivity along longitudinal direction. The 3ω technique and methods for the measurement of thermal conductivity of nanowires is discussed in detail as follow.

In this method, if the sample is electrically conductive and with a temperature-dependent electric resistance, the specimen itself could serve as a heater as well as a temperature sensor. Feeding an ac electric current of the form $I_0 \sin \omega t$

into the specimen creates a temperature fluctuation on it at the frequency 2ω, and accordingly a resistance fluctuation at 2ω.　This further leads to a voltage fluctuation at 3ω across the specimen.　Systematic investigations of the 3v method were carried out mainly during the 1960's [49-51] and in the last ten years, [52-57] which made the method practical.　However, in the previous studies the heat conduction equation was solved under the approximations either only for the high frequency limit, [49, 50, 57] or only for the low frequency limit. [52, 54, 55] With those approximations one lost either the information on the thermal conductivity or the information on the specific heat of the specimen.　By comparison with other methods, the 3ω method yields more information.　This method can measure electrical conductivity (σ), thermal conductivity (κ) and specific heat (C_p) at the same time.　In following sessions the explicit solution for the 1D heat-conduction equation, which was reported by L. Lu in [58] would discuss.
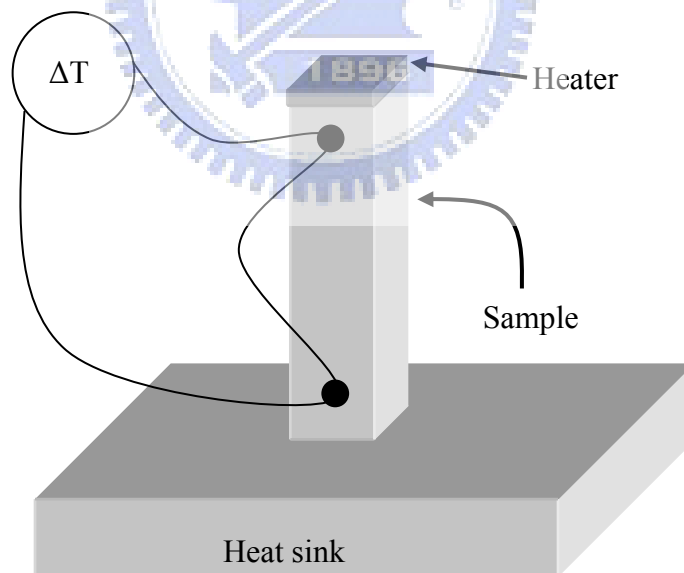
Figure 3.3 The typical arrangement for thermal conductance measurement. Usually, the large bulk sample is fixed on a high thermal conductive heat sink. The heater is placed on top of sample to provide a steady heat flow by a power P, which generate a stable temperature gradient cross the sample. The temperature different ΔT then is measured with a set of thermometry, since the thermal conductivity κ can be calculate with the simple formula $\kappa = P/\Delta T$.

We consider a uniform filament-like specimen in a four-probe configuration as for electrical resistance measurement. A complete construction for this model is shown in Figure 3.4. The two outside probes are used for feeding an electric current, and the two inside ones for measuring the voltage across the specimen. The specimen between the two voltage probes is suspended to allow temperature fluctuation. All probes have to be highly thermal conductive, to heat link the specimen at these points to the substrate. The specimen has to be maintained in a high vacuum and the whole setup is heat shielded to the substrate temperature to minimize the radial heat loss through convection and radiation. In such a configuration and with an ac electrical current of the form $I_0\sin(\omega t)$ passing through the specimen, the heat generation and diffusion along the specimen can be described by a partial differential equation, which the details will descript in next session.
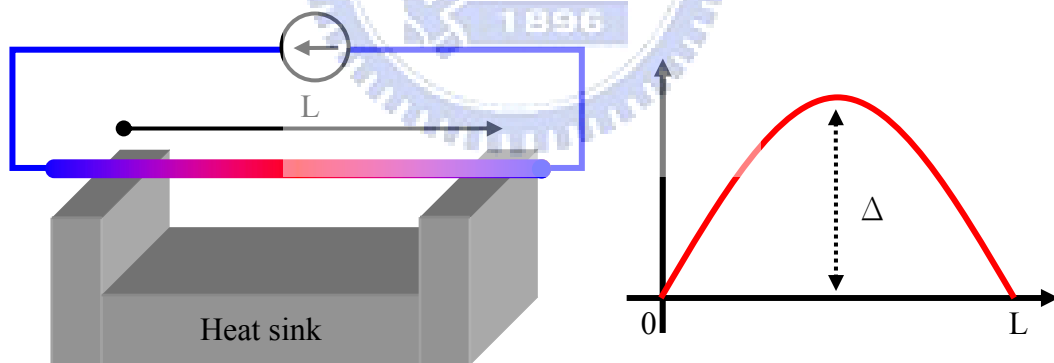
Figure 3.4 the sketch for sagging structure and the temperature distribution of a wire. As shows in the right figure, a sagging wire presents a temperature gradient by injecting a current into wire. For an appropriate applied current, the temperature of end points of the wire contacting with heat sink is keeping the same with heat sink.

3rd harmonic signal:

In a one-dimensional configuration and with a sinusoid electrical current passing through the specimen, the heat generation and diffusion along the specimen can be described by the following partial differential equation and the initial and boundary conditions:

$$\rho C_p \frac{\partial}{\partial t} T(x,t) - \kappa \frac{\partial^2}{\partial x^2} T(x,t) = \frac{I_0^2 \sin^2 \omega t}{LS}(R + R'(T(x,t)) - T_0), \qquad (3.1)$$

where κ, C_p, R, ρ, L, and S are the thermal conductivity, specific heat, electric resistance, mass density, length, and cross-section of the specimen at the substrate temperature T_0, respectively. Let $\Delta(x, t)$ denote the temperature variation from T_0, i.e., $\Delta(x,t)=T(x,t)-T_0$ Eqs. 3.1 then becomes

$$\frac{\partial}{\partial t}\Delta(x,t) - \alpha \frac{\partial^2}{\partial x^2}\Delta(x,t) - c \sin^2 \omega t \cdot \Delta(x,t) = b \sin^2 \omega t, \qquad (3.2)$$

where $\alpha = \kappa/\rho C_P$ is the thermal diffusivity, and $b = I_0^2 R/\rho C_P LS$, $c = I_0^2 R'/\rho C_P LS$. They obtain the temperature distribution along the specimen:

$$T(x,t) - T_0 = \Delta_0 \sum_{n=1}^{\infty} \frac{\left[1 - (-1)^n\right]}{2n^3} \times \sin \frac{n\pi x}{L}\left[1 - \frac{\sin(2\omega t + \phi_n)}{\sqrt{1 + \cot^2 \phi_n}}\right], \qquad (3.3)$$

where $cot\varphi_n = 2\omega\gamma/n^2$, and $\Delta_0 = 2\gamma b/\pi = 2I_0^2 RL/\pi\kappa S$ is the maximum dc temperature accumulation at the center of the specimen. Δ_0 is only κ dependent. The information of C_P is included in the fluctuation amplitude of the temperature around the dc accumulation.

By solving the partial differential equation, the resistance fluctuation can be expressed as

$$\delta R = R'\Delta_0 \sum_{n=1}^{\infty} \frac{\left[1 - (-1)^n\right]^2}{2\pi n^4} \times \left[1 - \frac{\sin(2\omega t + \phi_n)}{\sqrt{1 + \cot^2 \phi_n}}\right]. \qquad (3.4)$$

The production of the total resistance $R+\delta R$ and the current $I_0 \sin\omega t$, the voltage across the specimen contains a 3ω component $V_{3\omega}(t)$. Only taking the $n=1$ term at

low frequency range, the 3ω component can be express as

$$V_{3\omega}(t) \approx -\frac{2I_0^3 LRR'}{\pi^4 \kappa S \sqrt{1+(2\omega\gamma)^2}} \sin(3\omega t - \phi).$$ (3.5)

The root-mean-square value of voltage across the specimen contains a 3ω component $V_{3\omega}(t)$, we have

$$V_{3\omega} \approx \frac{4I^3 LRR'}{\pi^4 \kappa S \sqrt{1+(2\omega\gamma)^2}},$$ (3.6)

where the κ and γ are thermal conductivity and thermal time constant, respectively. By fitting the experimental data to this result, we can get the thermal conductivity and thermal time constant of the specimen. The specific heat can then be calculated as $C_p=\pi^2\gamma\kappa/\rho L^2$.

3.2.3   Electronics and sample chip

The measurement system for four-probe and self-heating method includes three main parts; sample temperature control and electronic measurement system.

For the sample temperature control, a sample holder from THERMODYNAMIC INSTRUMENTS CORP. with low magnetic field NiCr-heater was mounted onto the commercial cryostat (OXFORD He^3 refrigerator), which provide a cooling power to cool sample to low temperature.   The heating power was controlled by the temperature controller LakeShore-340 of Lake Shore Cryotronics, Inc., which control the temperature of sample in the range form 0.3 to 350 K.   In the holder, there were three resistance-temperature-detector (RTD) used to detect the temperature of sample. They are PT100 and Cernox from Lake Shore Cryotronics, Inc., and SA-1400 from THERMODYNAMIC INSTRUMENTS CORP.   PT100 perform an accuracy temperature sensing in the calibrated range from 30 to 550 K, however, Cernox and SA-1400 give the accuracy temperature from 0.3 to 100 K.   Especially, the calibrated SA-1400 temperature sensor is a high sensitivity and low magnetic influence sensor, which provide a double checking to prevent the missing working of Cernox. Furthermore, this whole set was installed to a He^4 dewar, which includes a superconductor magnetic with maximum field up to 9 Tesla.

The electronic instruments for resistance measuring include an alternating current source, preamp and lock-in amplifier, and power transformer.   The model of current source was KEITHLEY 6221, which provide sine wave current from 1 nA to 100 mA and frequency range from 1 mHz to 100 kHz.   The voltage signal were amplified by pre-amplifier 5113 and pick up with lock-in amplifier AMetek model 7265.   All instruments operating were performed by a computer with GPIB and LABVIEW program.   Meanwhile, all data were collected and transfer to computer

for recording and calculating by GPIB interface.   The characterization and operating detail of cryostat probe was described in session 3.1-D.   The detail schema of the temperature control devices and electronic instruments show in figure 3.5.
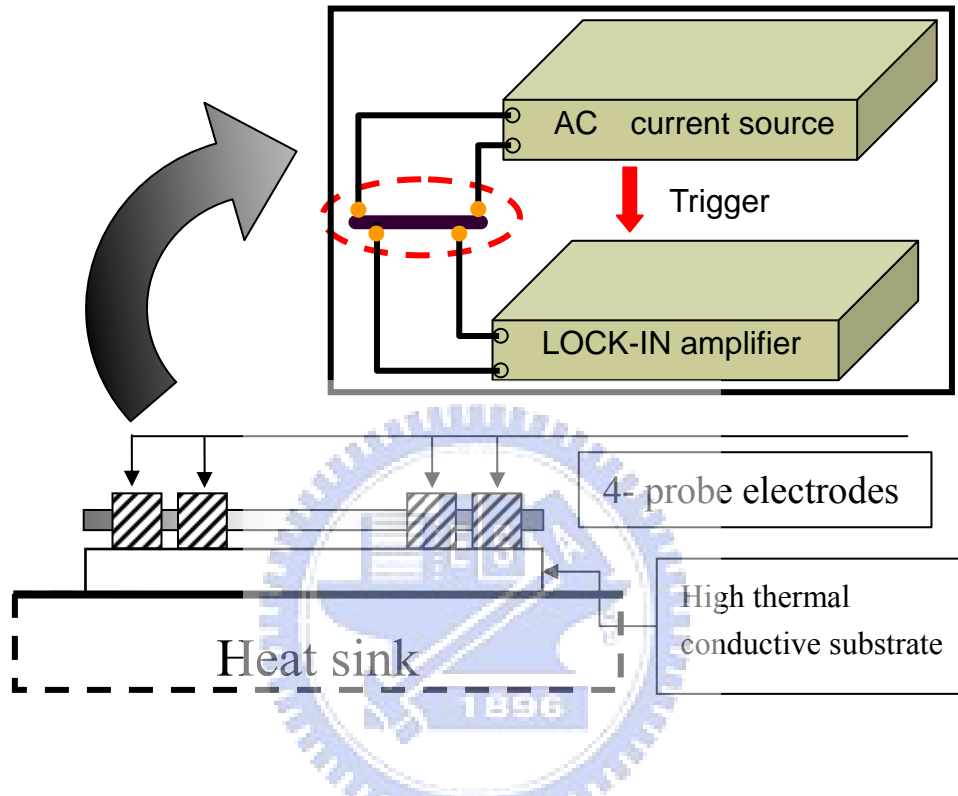
Figure 3.5 The schematic sketch of measurement setup and settling of specimen.

Chapter 4

Nanowires fabrication

Introduction

First of all, the fabrication of nano-scale materials is a challenge and much important to research of low-dimensional systems. This chapter introduces the experimental tools and techniques involved in fabricating nanowires. In order to synthesis nano-materials, several methods were reported to form nanostructure. Some of them, the methods are used usually for some special materials. This chapter introduces two methods to fabricate nanowires. The first part is a Bottom-up method, which the nanostructure formed self-assembly (Self-assembly method, SAM). Section 4.1 describes the detail procedures to fabricate nano-porous template and how to form nanowires within these anodic aluminum oxide (AAO) templates. The second part is a Top-down method, which need a lot of patterning and etching processes. Sections 4.2 will give the description to the lithographic (Optical Lithography, OL and Electron Beam Lithography, EBL), film deposition and etching techniques.

4.1   Bottom-up method

In this method, we combined two techniques to form nanowires.   First, we use the anodization process to form porous template, it's so called anodic aluminum oxidation technique.   This technique is a self-assembly reaction, the acid solution will oxidize aluminum (Al) foil under a specific applied electric field to form amorphous alumina (Al_2O_3) with high aspect ratio and uniform nano-pores.   Second, a deposition procedure is used to grow materials into these nanopores in templates by so called electrodeposition.

4.1.1 Fabrication of nano-scale porous template

In recent years, there has been increasing interest in the fabrication of nanometer-sized fine structures because of their potential utilization in electronic, optical, and micromechanical devices.   Although, Several techniques have been proposed to synthesis high-density and regular nano-pore arrays, such as e-beam and x-ray lithography, proton beam writing (PBW) and AAO [59-65].   The AAO is one approach to the fabrication of nanometer-sized structures, and the AAO has been considered as a naturally occurring structure as a host for the fabrication [64-71]. This approach is promising, especially for the preparation of large-area, nanometer-sized structures with high aspect ratios, which are difficult to form by a conventional lithographic process.   Over all techniques, AAO is the better choice by most material researchers, because of its simple and rapid fabrication and cost effectiveness.   The technique of porous formed in electrolytes under anodic bias has been studied and reported in 1953. [72] In 1970s, O'Sullivan and Wood [73] presented a model based on the electric field distribution to explain why pores grow at

all and why their size distribution is quite narrow. The further refined models [74-76] can give microscopic explanations for the dependence of, e.g., pore diameters and pore distances on applied voltage or electrolyte composition. In recent decade, the attractive issue about low-dimensional science is giving rise to a lot of research on growing porous anodic aluminum oxide (AAO) [77-85]. Anodic porous alumina, which is prepared by the anodic oxidation of aluminum in an acidic electrolyte, is one of the typical self-organized fine structures with a nanopore array [86, 87]. Anodic porous alumina has a packed array of columnar hexagonal cells with central, cylindrical, uniformly sized holes ranging from 7 to 400 nm in diameter. Such nanopore arrays of alumina (Al_2O_3) are known to exhibit hexagonally ordered pores and considerable structural strength on the nanoscale. Many types of nano-composites have been fabricated with anodic porous alumina used as a host material; when used for the preparation of magnetic recording media [88, 89], optical devices [90], functional electrodes [91, 92], and electrochromic [93] and electroluminescence display devices [94], the holes in these materials are filled with metals or semiconductors.

Self-organized formation of hexagonal pore arrays in anodic alumina provides a conventional tool to fabricate the low-dimension materials. Porous oxide growth on aluminum under anodic bias in various electrolytes has been studied for several decades [86]. But highly regular polycrystalline pore structures occur only for a quite small processing window. Recently reported self-organized pore growth, leading to a densely packed hexagonal pore structure for certain sets of parameters. Especially, within an oxalic acid, the pore size is a linear relationship to anodic voltage [95]. Figure 4.1 shows this published result revealing this dependence. According to these parameters and follow the process, it is easy to select the parameter for getting suitable size of pores.
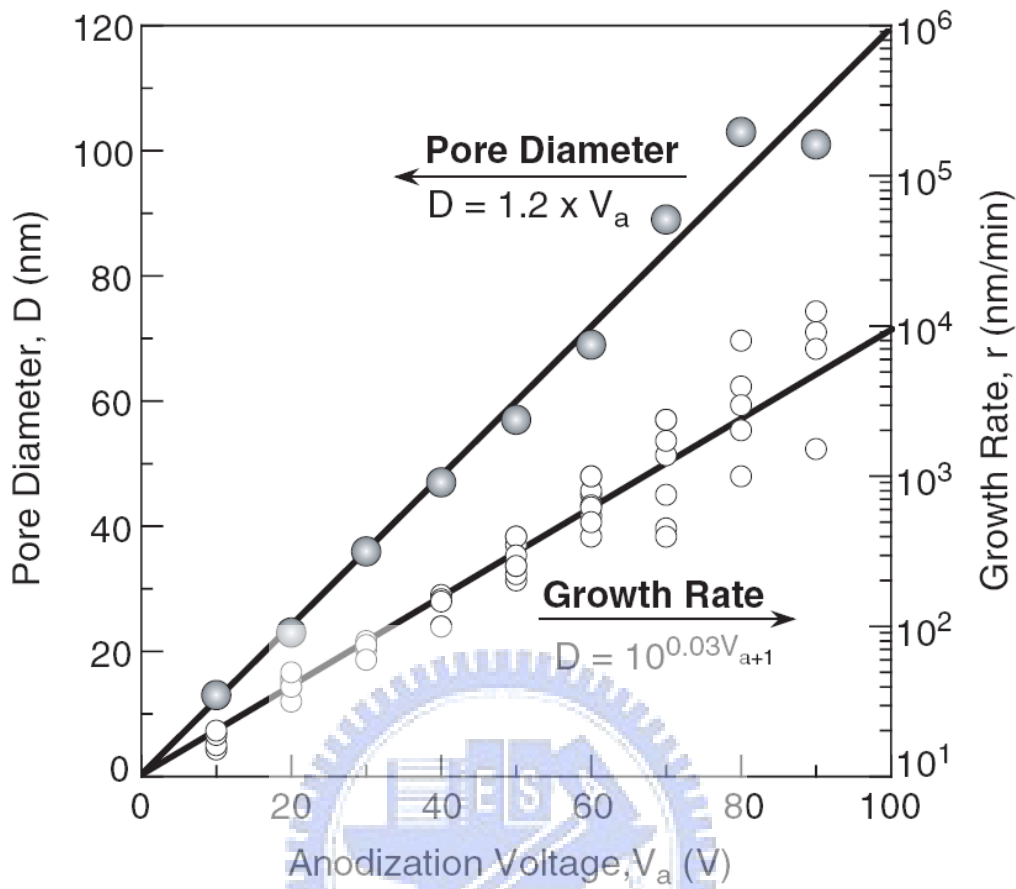
Figure 4.1 Relationship between pore diameter and growth rate of anodic alumina membrane and anodic voltage.

Experiment

The chemical reactions of aluminum oxidation are [96]

Anodic reaction: $2\,Al \rightarrow 2\,Al^{3+} + 6\,e^{-}$

Oxide-electrolyte interface: $2\,Al^{3+} + 3H_2O \rightarrow Al_2O_3 + 6\,H^{+}$

Cathodic reaction: $6\,H^{+} + 6\,e^{-} \rightarrow 3H_2$

Overall reaction: $2\,Al + 3\,H_2O \rightarrow Al_2O_3 + 3\,H_2$
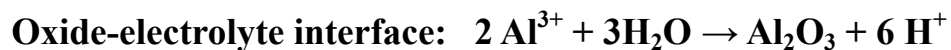
This reaction occurs spontaneously until the compact barrier layer is formed. Chemical reactions in aqueous are always complex, so that the diameter of pores in

AAO template well depend on temperature, electrolyte composition, and electrical potential. In order to obtain the high regular, uniform pore diameter, and thick alumina foil, a low temperature experimental set-up is designed to provide all components at low temperature. Figure 4.2 shows the experimental set-up. Temperature of the electrolyte and components are maintained at low temperature around 0 °C using a commercial refrigerator. A resistance temperature detector (RTD) was used for the temperature sensing, and a 400 mL beaker was used to contain the electrolyte.
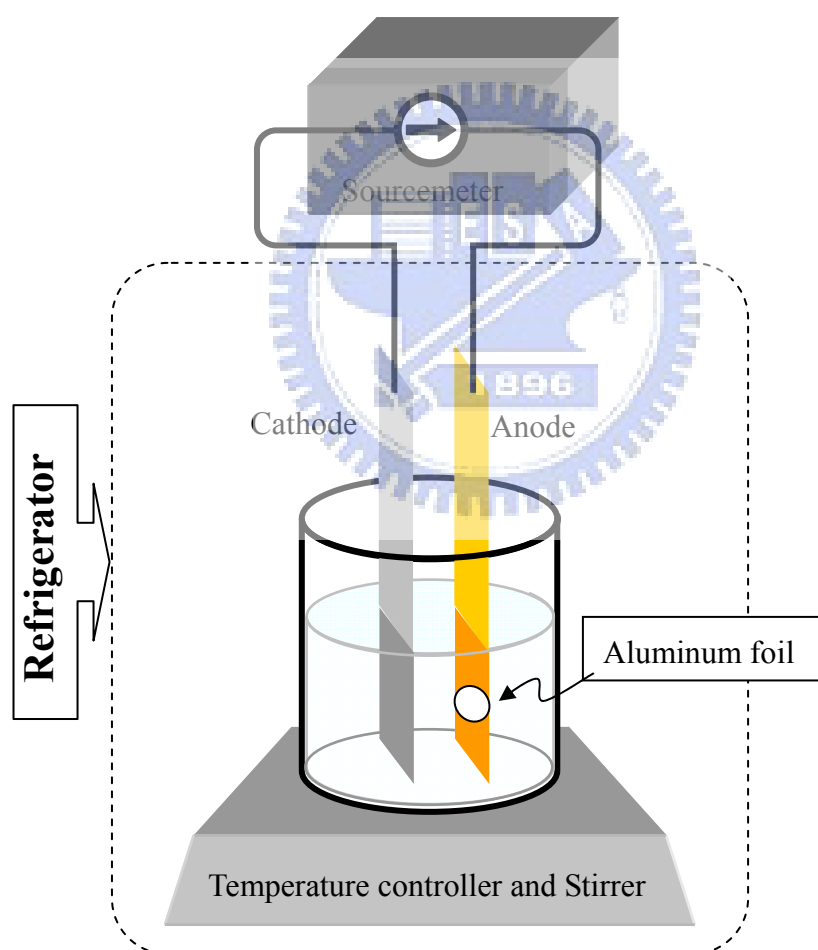
Figure 4.2 The setup scheme for the fabrication of nano-porous template. sThe materials of anode and cathode electrode are copper and platinum, respectively. This whole set were placing on a temperature and stirrer controller in a refrigerator.

A pure Aluminum foil (purity ~ 99.9999%) is degreased by ultrasonic cleaner with acetone and ethanol in sequence. The pure and cleaned aluminum foil was mounted on a copper plate which was served as the anode electrode, and subjected to electro-polishing in a H_3PO_4: H_2SO_4: H_2O solution with weight ratio 4:4:2 for obtaining smooth surface. The applied potential is about 20 Volt to flatten the surface of foil. Then, a two-step anodic oxidization process is performed to fabricate AAO template. The flattened foil is anodized in an acid aqueous at a suggested applied voltage about 0 ~ 3 °C. Pretreated foil then goes through the second anodizing with the same condition of first step. To this step, sample formed three layers, they are pore-layer, barrier-layer, and aluminum-layer. The barrier-layer is a thin alumina layer, which is covering and stoking nanochannels to stop the passing of electrolyte. For the goal to remove the barrier layer, $CuCl_2$ and 2 wt% NaOH are used to etch the aluminum and barrier layer in sequence. Figure 4.3 shows some SEM images of AAO templates by the above condition. This detail processes will show in Figure 4.4.
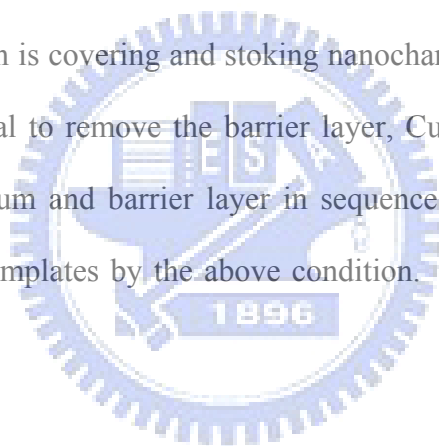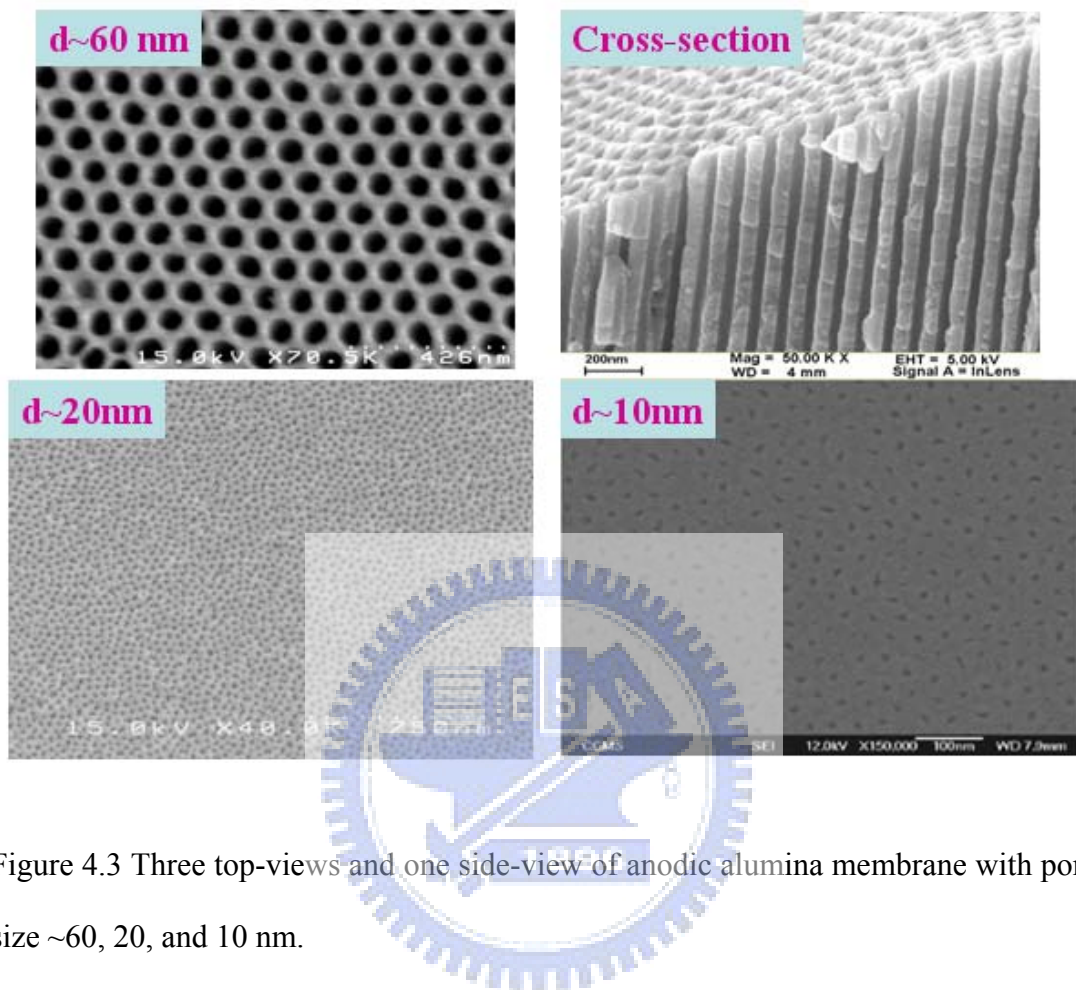
Figure 4.3 Three top-views and one side-view of anodic alumina membrane with pore size ~60, 20, and 10 nm.
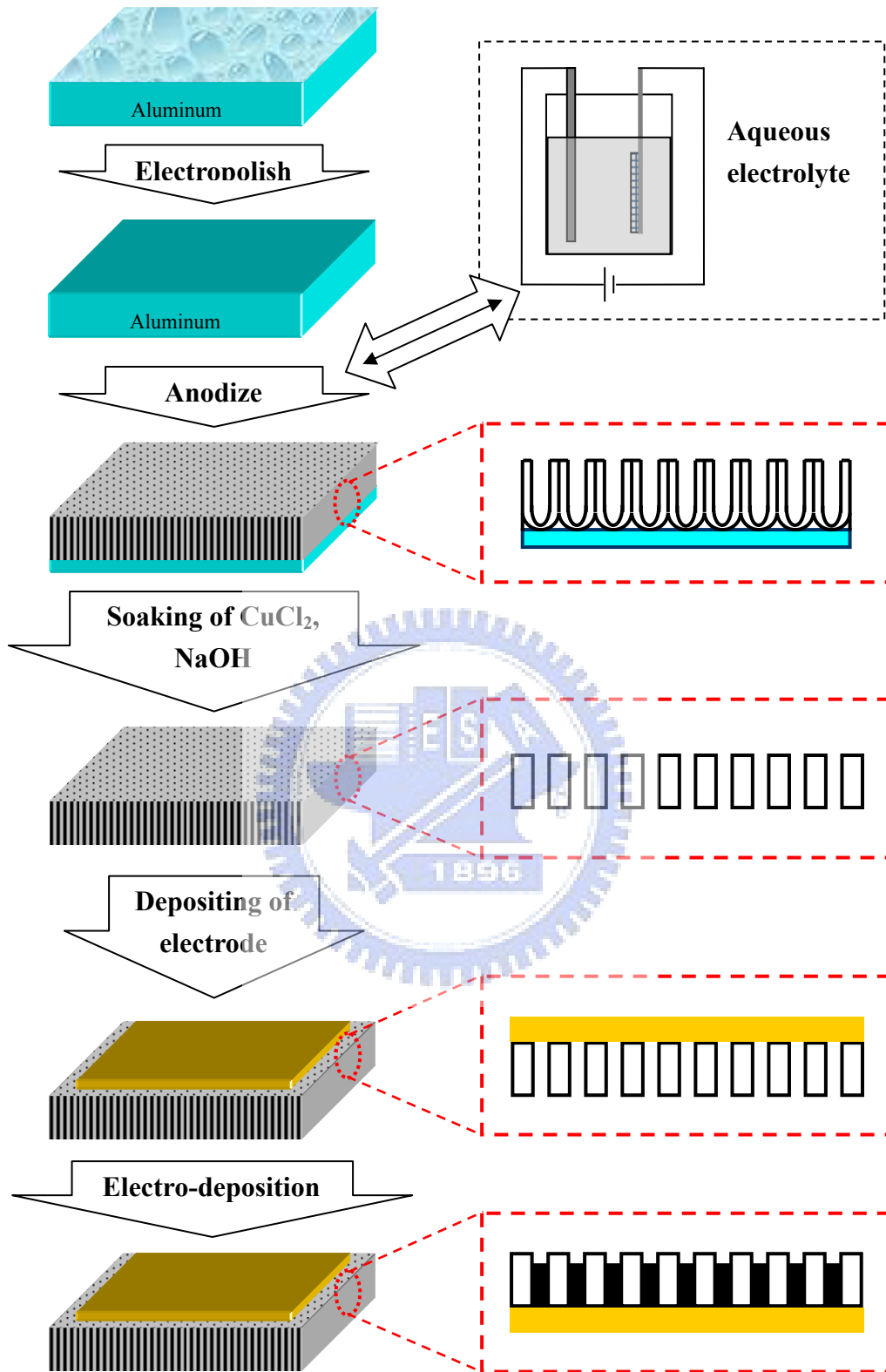
Figure 4.4 The scheme of a whole procedure to deposit nanowires in AAO template.

4.1.2　　Fabricate nanowires by electodeposition

Metal Electrochemical deposition also called electrodeposition for short is the branch of electrochemistry that deals with the chemical action of electricity and production of electricity by chemical reaction. Electrodeposition is an important processing technique for depositing thin films and nanostructures due to its low cost, high yield, low energy requirements, and capability for generating complex and high aspect ratio features. Electrodeposition has been widely used in the microelectronics industry for interconnects, chip packaging, and magnetic storage. Especially, the thin film deposition or growth is important in these fields. Thin film science and technology play a crucial role in the high-tech industries all over the world today. For the first half of the past century, interests in thin films were centered on optical applications. Here, we will use this technique to grow iron and Bi_2Te_3 nanowires. The experiment setup were shown as Fig. 4.6
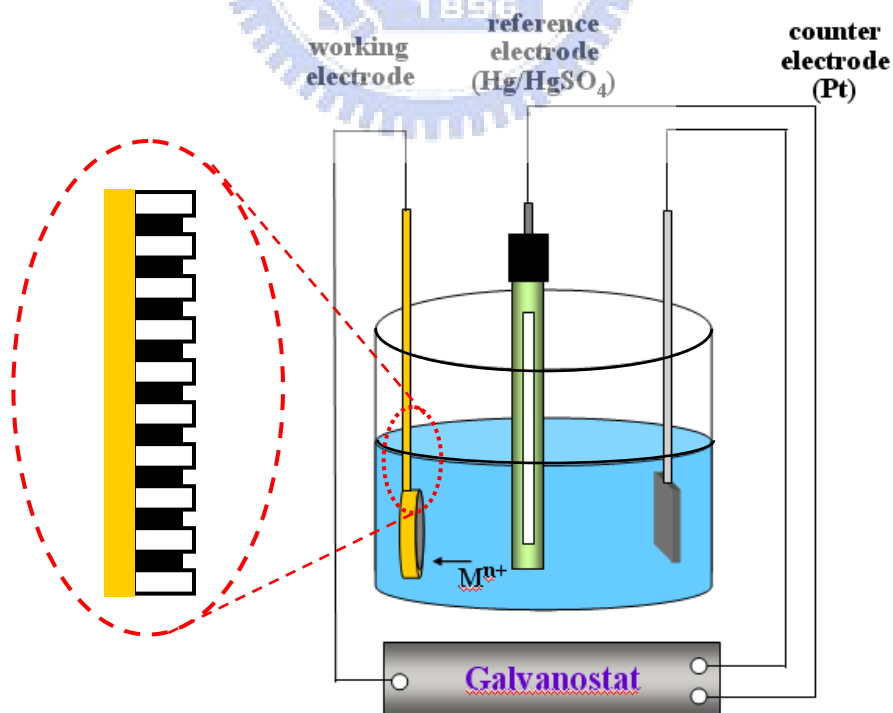
Figure 4.5 The scheme of experimental arrangement of electrodeposition setup.

4.2   Top-down method

The typical Top-to-Down technique for fabricating devices or sample is lithography.   Roughly, there are two techniques used to make devices and samples, one is the Optical lithography, the other one is so called Electron-beam lithography. The following sections will introduce these two technique and related techniques.

4.2.1   Lithography

Introduction to patterning

Optical lithography also called Photolithography is a process used in microfabrication to selectively remove parts of a thin film.   Usually, it uses ultraviolet light to transfer a pattern from a photomask to a light-sensitive photoresist (or say resist) on the substrate.   The exposed sample will go through a series of chemical treatments then cut the exposure parts into the material underneath the photoresist.

Photolithography shares some fundamental principles with photography, in that the pattern in the etching resist is created by exposing it to light, either using a projected image or an optical mask.   This step is like an ultra high precision version of the method used to make photography.   Subsequent stages in the process have more in common with etching than to lithographic printing.   It is used because it affords exact control over the shape and size of the objects it creates, and because it can create patterns over an entire surface simultaneously.

The steps involved in the photolithographic process are wafer cleaning; photoresist application; soft baking; mask alignment; exposure and development; and

hard-baking. The typical sequences of process steps are given in Figure 4.6 is typical for most silicon substrate fabrication steps. The cleaned substrate is covered with a homogeneous metal layer, which is subsequently coated with suitable photoresist. Illumination and development of the resist through a mask exposes some areas of the metal layer, while others are protected by the resist. The illumination is usually carried out with ultraviolet light or with electrons. An etch step follows, which selectively removes the free metal surfaces. Here, the resist acts as an etch mask. Finally, the resist gets removed, and a patterned metal layer on the substrate results. However, the much nonmetal material is not performed by this processing, since essentially all suitable metal etchants attack those materials as well. Therefore, fabrication scheme Figure 4.7 is typically used. Here, the substrate is first covered by resist, which gets illuminated and developed. Now, the metal is evaporated on the substrate, with the patterned resist acting as evaporation mask. The lift-off step follows. i.e., the resist is removed with the metal film on top. The final result is identical to that one of scheme Figure 4.6. For selective etching of the substrate Figure 4.8, steps 1 to 3 are identical to Figure 4.7. Then, the patterned resist is used as an etch mask for the substrate. We now discuss these fabrication steps in following sections.

| | **Thin film deposition** |

| | **Resist spin coating** |

UV light or e-beam   Metal mask

| | **UV light exposure** |

| | **Development** |

| | **Etching and resist remove** |
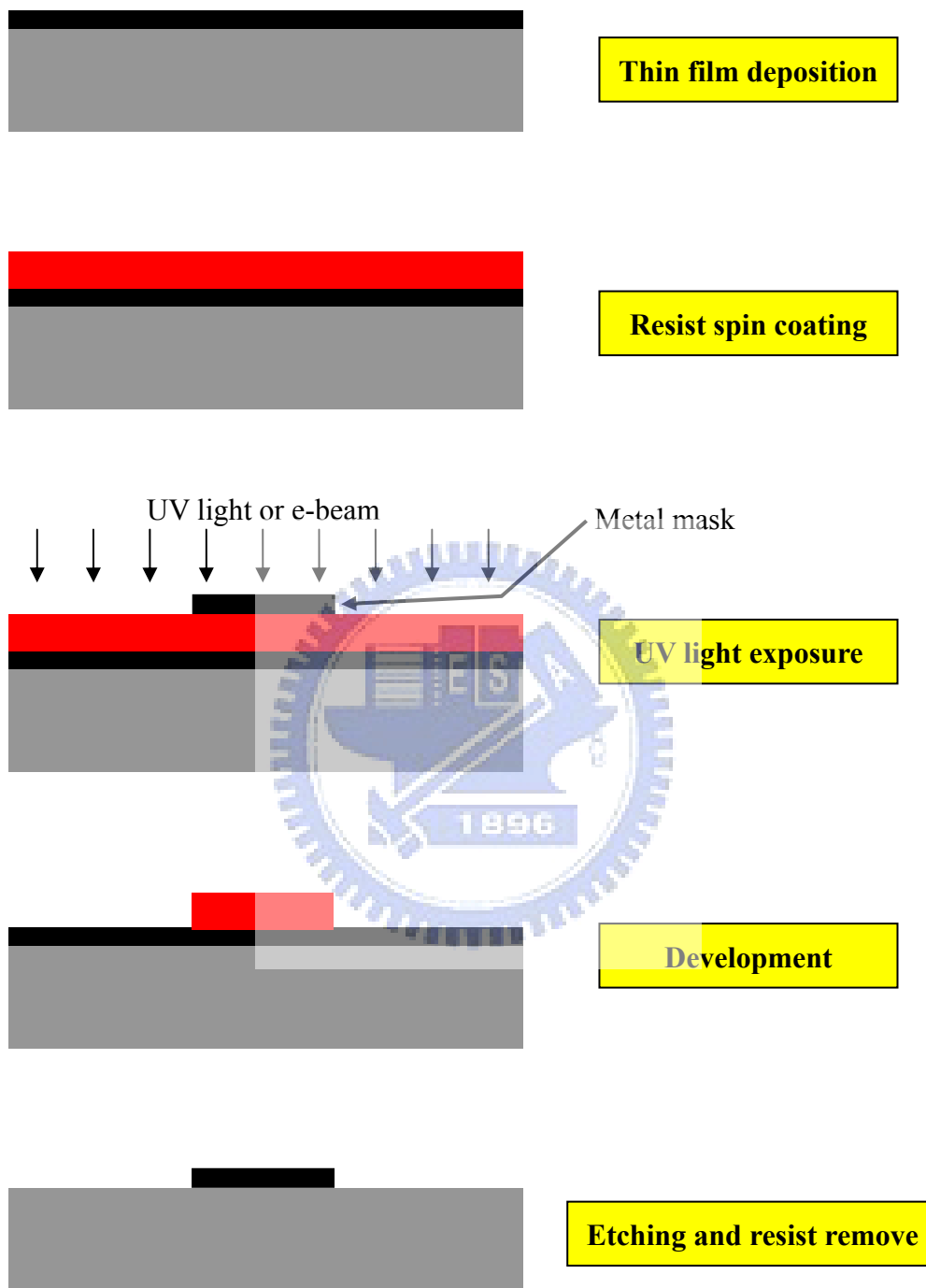
Figure 4.6 The typical sequences of process steps are given as above. It is typical for most silicon substrate fabrication steps.

| | Resist spin coating |

UV light or e-beam

Metal mask

| | UV light exposure |

| | Development |

| | Thin film deposition |

| | Resist remove |
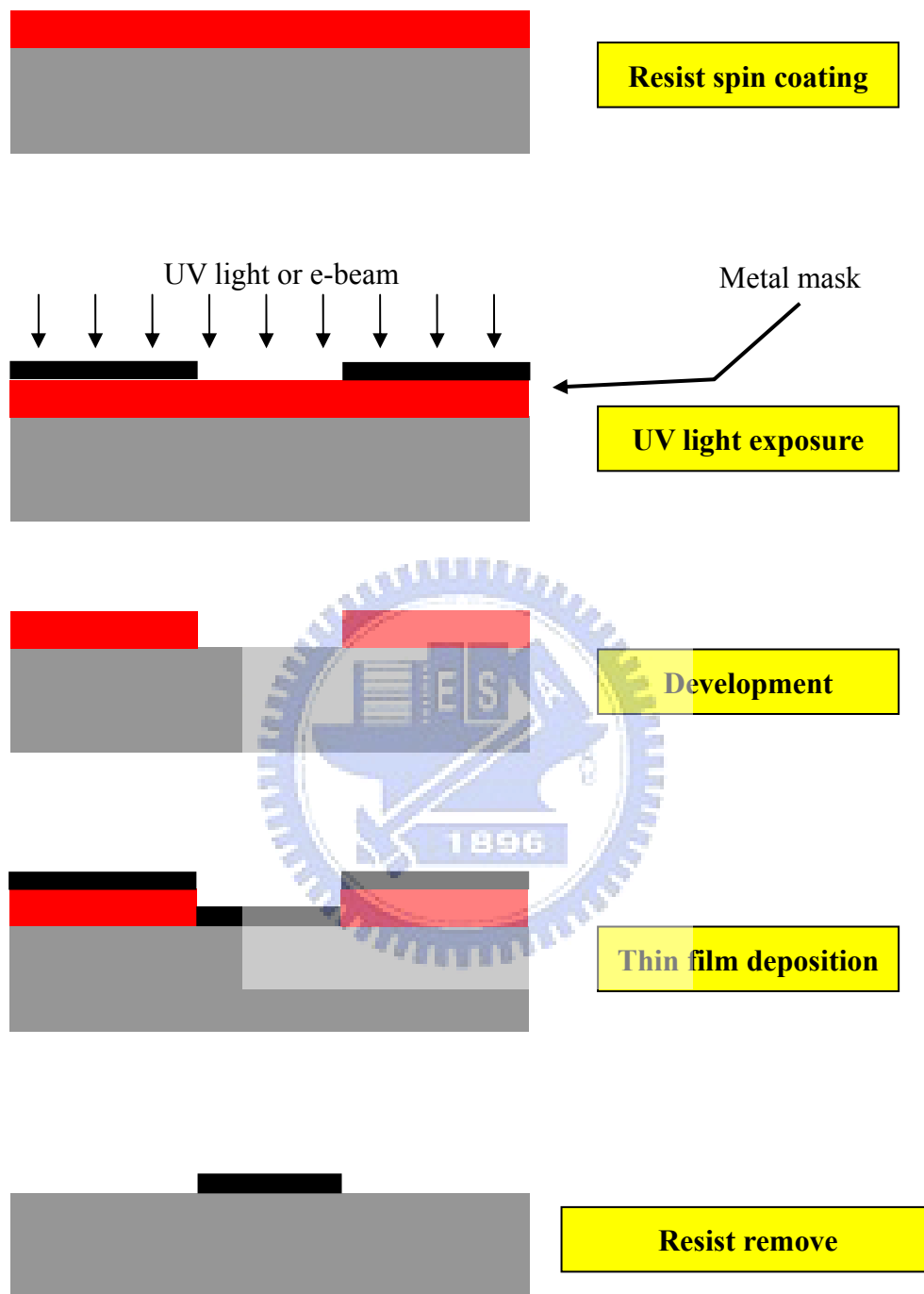
Figure 4.7 The much nonmetal material is not performed by procedure as figure 4.6, since essentially all suitable metal etchants attack those materials as well. Therefore, fabrication scheme above is typically used.
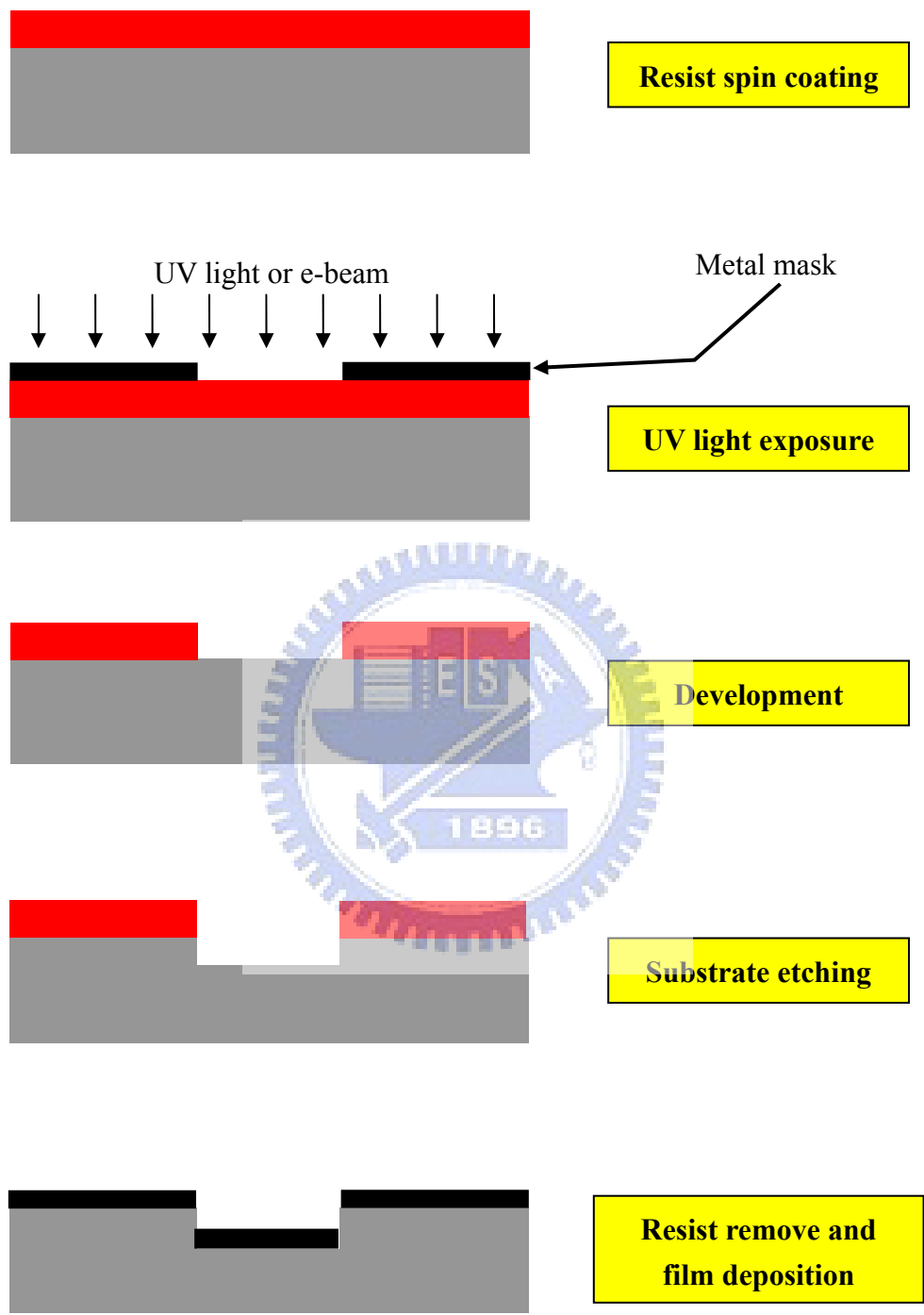
Figure 4.8 For that of high temperature deposition process, the substrate etching procedure usually choosing to solve the difficulty.

Defining patterns in resists

Optic lithography

By this we mean illumination of a photoresist by visible or ultraviolet light.   The sample is coated with a thin and homogeneous photosensitive resist.   This is done by dropping some resist solution onto the sample, which is then rotated for about one minute at high speed, typically a few thousand rpm. The spinning speed and the viscosity of the solution determine the thickness of the resist layer, which is of the order of 1 μm.   After baking the resist the sample is mounted into a mask aligner, a device designed for adjusting the sample with respect to a mask that contains the structure to be illuminated.   The mask aligner is equipped with a strong light source that illuminates the resist film through the mask see Figure 4.9a.   The pattern sizes are Doppler limited, which means that the smallest feature sizes are about half the wavelength (~ 150 nrn), divided by the index of refraction of the resist (~ 1.5), which limits the resolution to roughly 100 nm.   The mask can be a quartz plate Coated With a thin chromium film, which contains the pattern to be illuminated.   In the contact illumination scheme, the Cr film is in mechanical contact with the resist and blocks the light, such that the resist underneath the Cr remains unexposed. During contact illumination the mask suffers contaminations due to dust particles on top of the resist, as well as by resist adhesion.   This can be avoided by projection illumination, where the mask pattern is transferred into the resist via lenses. This technique is widely used in industry, but somewhat unusual in research labs. The photoresists can be classified as positive and negative. The solubility of the exposed areas increases for a positive resist, while it decreases in negative resist; see Figure 4.9a.   Immersing the sample into a suitable developer removes the corresponding sections of the resist film.   Both

types of resists have in common that their solubility as a function of the illumination dosage is a step-like function. This ensures high resolution and sharp edge profiles. It may seem irrelevant at first what kind of resist is used in a particular process. There may, however be some process specific requirements which favor one type or the other. Most importantly negative resist predominantly produces an undercut profile which means that after development, the resist area in contact with the sample is smaller than the area at the resist surface, Figure 4.9b. This is a consequence of the approximately exponentially decreasing intensity of the illuminating light as it penetrates into the resist. An undercut profile is highly, desirable for subsequent metallization steps, in which the resist itself serves as mask. After the metallization the resist including the metal film on top usually has to be removed in a lift-off step, which is bound to fail for resists with an overeat profile since the metal on the sample and that one on top of the resist are connected. An undercut profile avoids this problem, provided the thicknesses of metal layer and resist are properly selected.

In principle, the resolution can be increased by using shorter wavelengths. In X-ray lithography resists, are illuminated with wavelengths in the 10 nm regime. While significant progress, has been achieved over the past decade severe technological obstacles have to be overcome before this, version of optical lithography can he widely used. Photoelectrons limit the resolution to several 10 nm, and optical components as well as masks are difficult to fabricate since, metals get transparent in the UV. The ultimate limit of such lithographic techniques is set by the resolution of the resists, which contain organic polymers. The cross linking of the polymers is enhanced or reduced by the light, which modifies their solubility accordingly. Thus, the resolution cannot become better than the size of the corresponding monomers, which is of the order of 0.5 nm. For feature sizes below ~ 150 nm, electron beam lithography is· the current technique of choice.
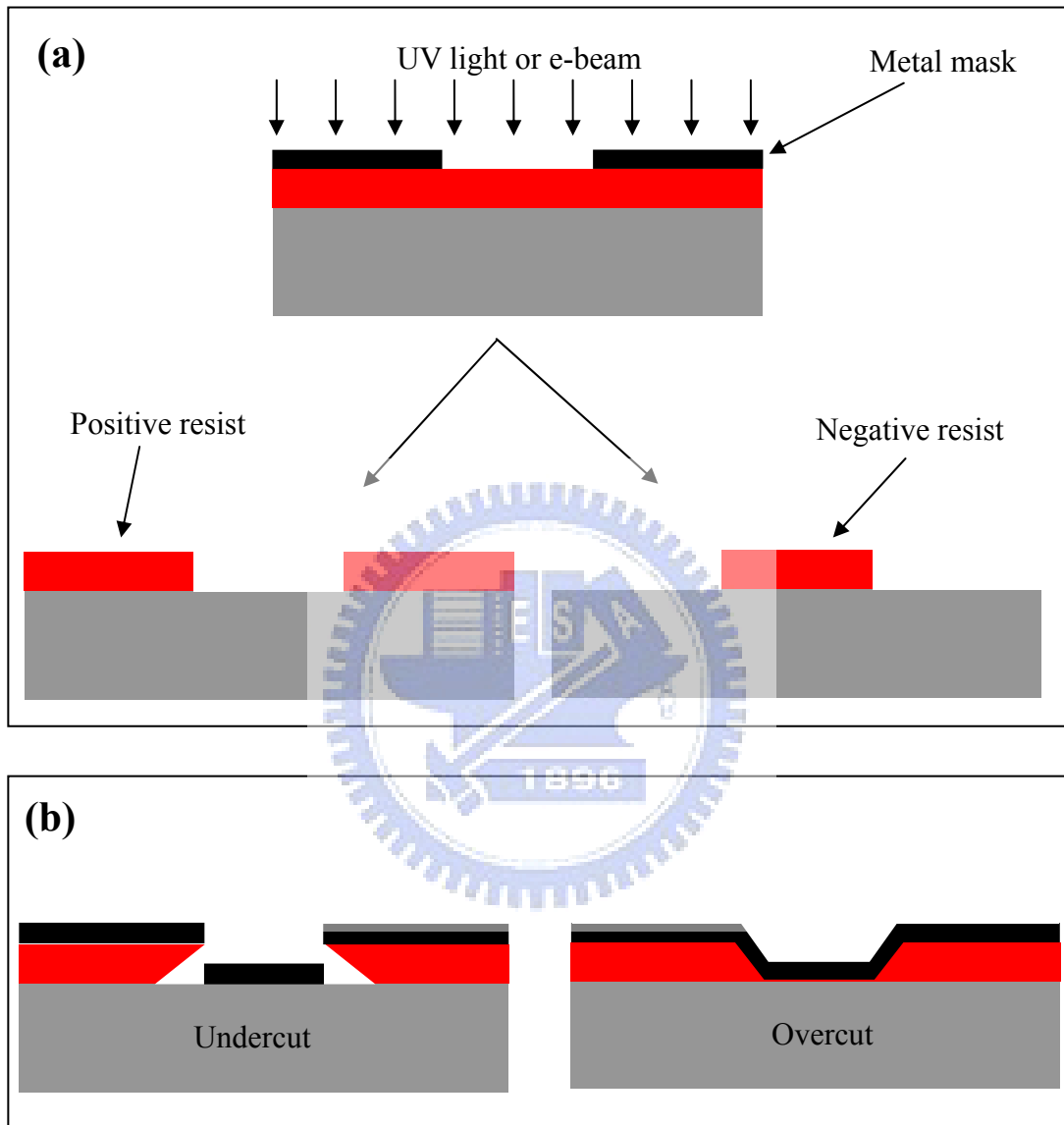
Figure 4.9 The selected resists and exposure devices may change the pattern resolution of by the typical sequences of process steps. Inset (a) is the resist cross section of positive and negative resist. The solubility of the exposed areas increases for a positive resist, while it decreases in negative resist. Inset (b) is the resist profile of different resist.

Electron beam lithography (EBL)

Instead of light electrons may be used as well for illuminating resists, which are in this case polymers like PMMA (poly-methyl metacrylate) with a well-defined molecular weight.   In a positive resist, the electron beam breaks the bonds between the monomers, and an increased solubility results. In negative resists, on the other hand, the electron beam generates inter-chain cross linking, which deceases the solubility in that respect electrons have a very similar effect as U.V. light on the resist. A focused electron beam is scanned in a predefined pattern across the, sample using deflection coils in the electron optics.   In contrast to optical lithography, this is a serial and therefore a slow process.   However structure sizes of 50 nm and even below can be fabricated.   Many research groups use electron beam lithography in the lab for all feature sizes below 2 μm, because the technique gives very good and reproducible results.   One type of electron beam lithography uses a high energy-beam of electrons (about 30 keV or larger), which produce extremely small spot sizes of about 1 nm only.   However the illumination resolution is worse than this, since the spatial distribution of secondary electrons backscattered from the substrate actually illuminate the resist.   Since the intensity of those electrons drops from the substrate towards the surface of the resist, an undercut profile is intrinsic to this process.   The undercut is often enhanced by a two-layer electron beam resist with different dosages.

4.2.2   Thin film deposition system

The vacuum thermal evaporation deposition technique consists in heating until evaporation of the material to be deposited. The material vapor finally condenses in form of thin film on the cold substrate surface and on the vacuum chamber walls.

Usually low pressures are used, about 10^{-6} or 10^{-5} Torr, to avoid reaction between the vapor and atmosphere. At these low pressures, the mean free path of vapor atoms is the same order as the vacuum chamber dimensions, so these particles travel in straight lines from the evaporation source towards the substrate. This originates "shadowing" phenomena with 3D objects, especially in those regions not directly accessible from the evaporation source (crucible). Besides, in thermal evaporation techniques the average energy of vapor atoms reaching the substrate surface is generally low (order of kT, i.e. tenths of eV). This affects seriously the morphology of the films, often resulting in a porous and little adherent material.

4.2.3   Etching

An important techllique for transferring the resist pattern into the sample is etching. Patterned resists can be used as etch masks, provided the etchant is sufficiently selective. We distinguish between dry etching and wet chemical etching.

Dry etching

The setup for dry etching techniques consists of a vacuum chamber with two electrodes at the top and the bottom.   The sample is placed at the bottom which may be the anode or the cathode, depending on the process.   A gas discharge is ignite, and the ions of the etch gas hit the sample (Figure 4.10).   One speaks of plasma etching if the reaction is purely chemical. Oxygen plasma etching is often used to remove resist layers.   The low energy ions avoid damage of the semiconductor and metal components of the sample.   A purely physical technique, on the other hand is ion etching.   Here, suitably selected ions are generated and strongly accelerated towards the sample.   The physical impact removes sample atoms.   Here, resists may serve

as masks for a limited time.   Radiation, damages in the sample, combined with the requited high vacuum and the large rate of material deposition at the walls, make this a rather unusual technique.   Widely used, however, is reactive' ion etching. Here, both the physical and the chemical aspects of the ionic, exposure are important.   A very convenient side produces in this kind of etching a polymer formation at the etched walls, which prevent lateral removal of material.   As a consequence very steep and deep grooves can be etched.
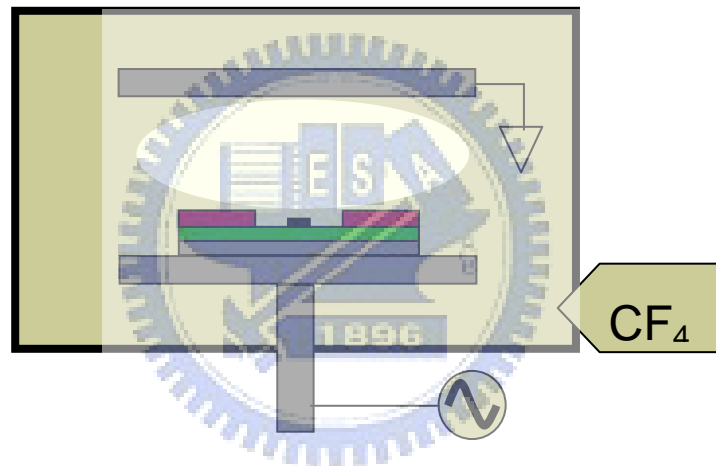
Figure 4.10 The sketch of a reactive ion etching (RIE) device, which performed a high selectivity and uniformity for etching process.

Anisotropic wet chemical etching

This is the simplest etching technology.   The rates depend on the etch composition as well as on the crystal direction.   The resulting edge profile can thus be tuned accurately.   All it requires is a container with a liquid solution that will dissolve the material in question.   Unfortunately, there are complications since

usually a mask is desired to selectively etch the material. One must find a mask that will not dissolve or at least etches much slower than the material to be patterned.

Some single crystal materials, such as silicon, exhibit anisotropic etching in certain chemicals. Anisotropic etching in contrast to isotropic etching means the different etch rates in different directions in the material. The classic example of this is the <111> crystal plane sidewalls that appear when etching a hole in a <100> silicon wafer in a chemical such as potassium hydroxide (KOH). The result is a pyramid shaped hole instead of a hole with rounded sidewalls with an isotropic etchant. The principle of anisotropic and isotropic wet etching is illustrated in the figure below.

Silicon anisotropic wet chemical etching using KOH, EDP or TMAH solutions, as one of the key manufacture techniques in MEMS fabrication, plays a critical role in the development of most MEMS devices. The anisotropic etching process can be greatly improved and optimized if efficient and accurate simulation tools are used to predict performance of anisotropic etching process.
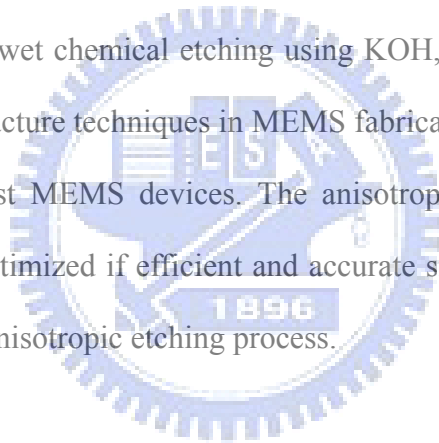
Chapter 5

Results and Discussion

Introduction

In this chapter we present results of fabrications for AAO template, iron nanowire, and sagging Ni-NW, and the characterization of those samples. Section 5.1 shows the results and SEM images of various pore size AAO templates. Meanwhile, section 5.2 shows the electrical and magnetic characterization of iron nanowire, which grow in the AAO template with chemical electrodeposition. Section 5.3 gives a simple example of 10 μm platinum wire how the 3ω method applies for studying the filament like sample. At the last section of this chapter, we discuss the fabricating result, electronic and thermal transport, and thermodynamic properties of Ni-NW.

5.1 AAO template fabrication

In this work, a commercially available aluminum foil (purity~99.9995%) with a thickness of 130 μm was used as the initial material to prepare AAO, and remain about 70 ~ 100 μm.   There are two diameters of pores were fabricated, one is 60 nm template and the other one is 25 nm template.   The 60 and 25 nm templates are performed with different procedures, which descript as follow.

For 60 nm

The first anodizing, flattened foil is anodized in a 0.3 M oxalic ($H_2C_2O_4$) acid aqueous at applied voltage 40 V at 0 °C for 2 hours.   Before second step, the formed alumina layer was removed by 5 wt% NaOH as a pretreated sample.   Pretreated foil then goes through the second anodizing with the same condition of first step for 20 hours.   Figure 5.1 shows the SEM images of the 60 nm template.

For 20 nm

There is only one anodizing step performed in fabricating of 20 nm template. The flattened foil is anodized in a 12 wt% sulfuric acid (H_2SO_4) aqueous at applied voltage 18 V at 0 °C for 8 hours.   Fig. 5.2 shows the SEM images of the 20 nm template.
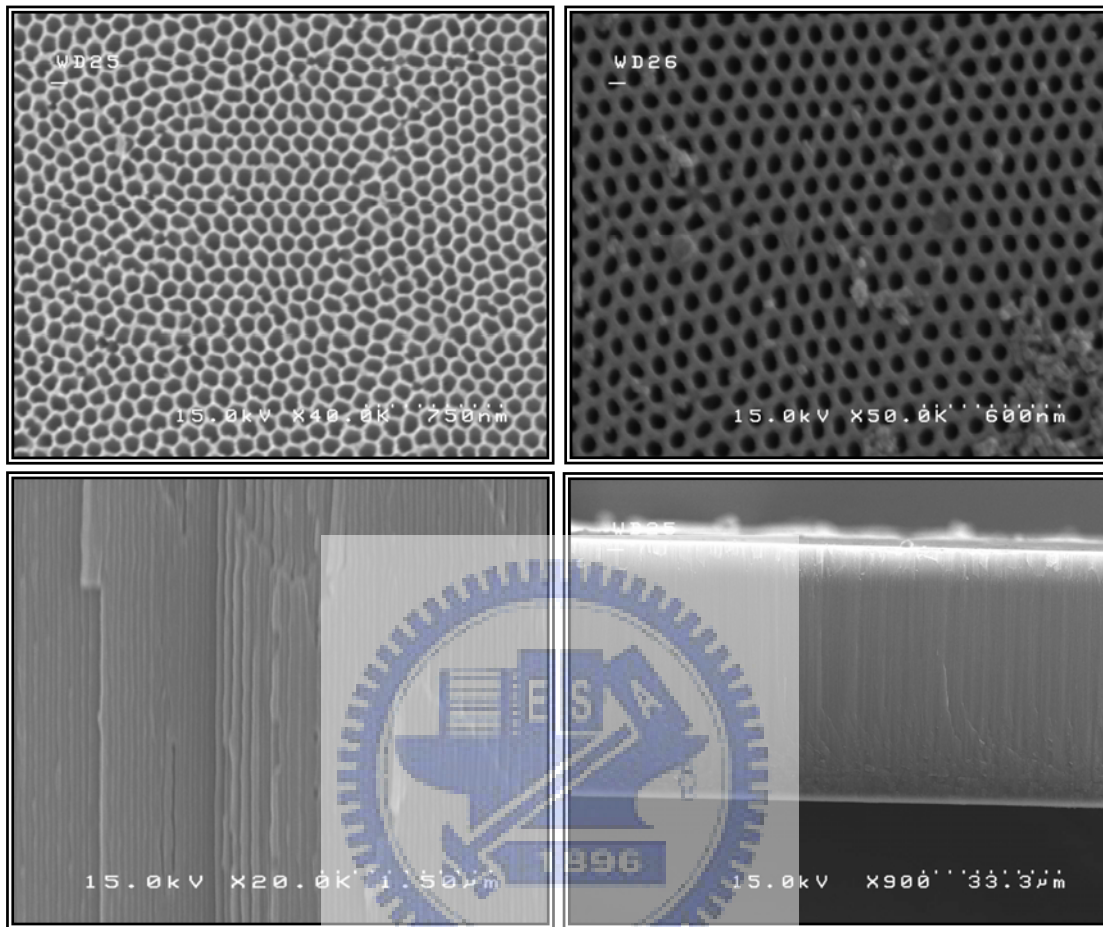
Figure 5.1 The SEM images for the 60 nm template. The (a) and (b) are the top and back side view, respectively. It shows that the average pore size is about 60 nm. The (c) and (d) shows a cross section view in different magnification, which shows that the thickness of template is about 70 μm.
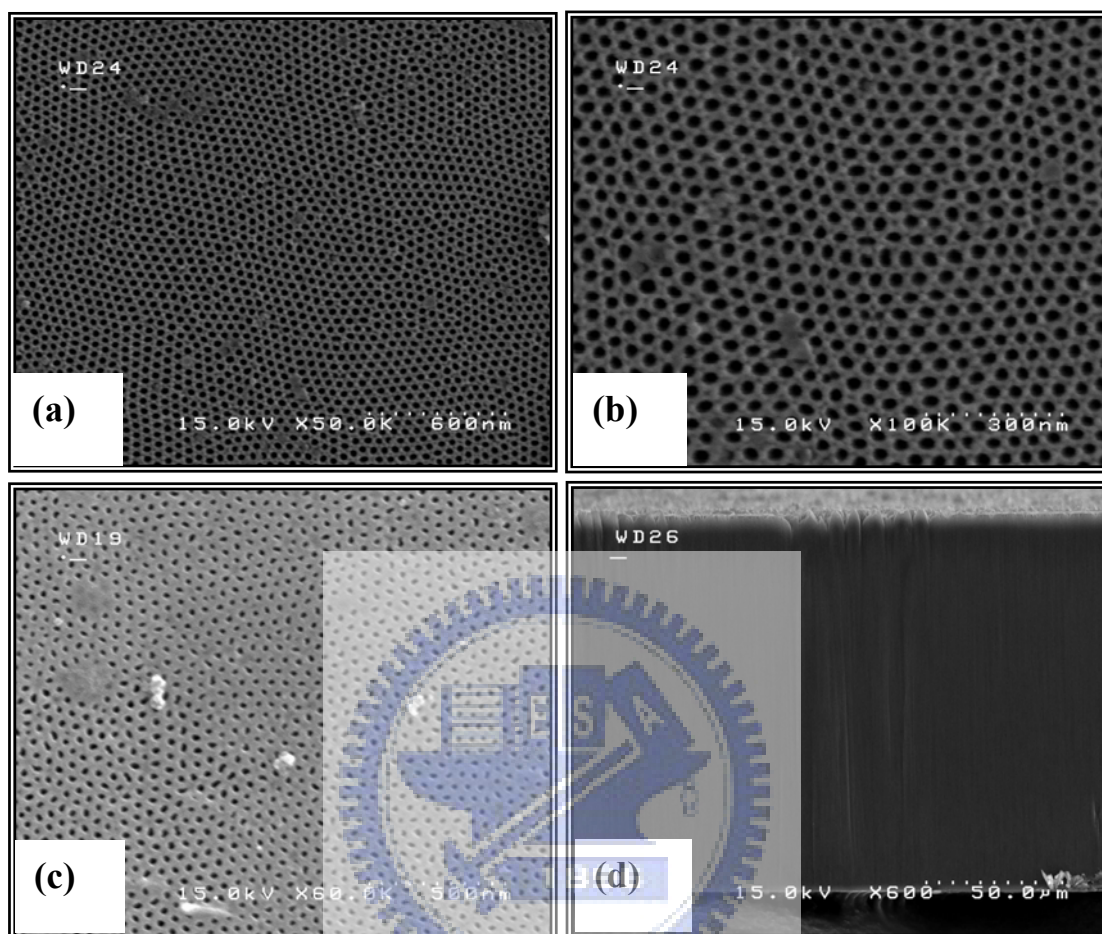
Figure 5.2 The SEM images for the 20 nm template.   The (a) and (b) are the top view in different magnification.   It shows that the average pore size is about 20 nm. The (c) is back side view.   The (d) shows a cross section view, which shows that the thickness of template could be over 100 μm.

5.2   Imbedded iron nanowires

5.2.1   Synthesis of nanowire arrays

In order to study the size dependent behaviors, two anodized alumina membranes were used for growing Fe NWs.   One is the available commercial AAO template from the Whatman International Ltd. with pores diameter ~200 nm and thickness ~60 μm.   The other one is homemade, according to procedure described in section 4-1 with diameter ~60 nm and thickness ~80 μm.   In order to perform chemical electro-deposition, a gold layer was deposited on the bottom side of AAO by means of thermal evaporation to serve as the cathode electrode. Iron was electrodeposited into a porous membrane using dc electrolysis in solution of $FeSO_4 \cdot 7H_2O$ (0.43 M) and boric acid (0.72 M) with pH~3 at room temperature.   Deposition was carried out with constant potential at -1.2 V, with platinum counter electrodes [97, 98] until the iron could be seen on the surface of AAO by eyes.   A mechanical polishing process was carry on to remove the over grown thick iron layer on the upper surface of AAO. The shinny iron surface on the top of template indicates that the oxidation of iron was negligible.   Figure 5.3 shows the optical microscopic (OM) images for iron-filled commercial AAO templates.

The morphology, diameter and length of pores in the AAO were determined with scanning electron microscope (SEM, Hitachi S-4200) by the plane and cross section images of SEM, respectively; meanwhile the iron filling was confirmed by EDX and shows in Figure 5.6.   Images in figure 5.4 and 5.5 show SEM images of 60-nm and 200-nm FeNWs template, respectively.

Finally, a gold electrode was deposited on that of the template to form a thin

layer on the surface of iron nanowire (FeNW) array.   The gold layer plays two roles; it protects the surface of FeNWs from oxidation, and serves as the contact layer for the resistance measurements.   After the magnetization measurement, the x-ray diffraction (XRD) pattern of FeNWs-array was taken immediately, no noticeable oxidation of iron was revealed on the XRD profile.

Figure 5.3 OM images of the iron-filled AAO templates.   Images are (a) and (b) the as grow sample without mechanical polish of 60 nm template, (c) the as grow sample without mechanical polish of 200 nm template, and (d) the sample performed with polishing. The silver parts indicate the filling of iron.
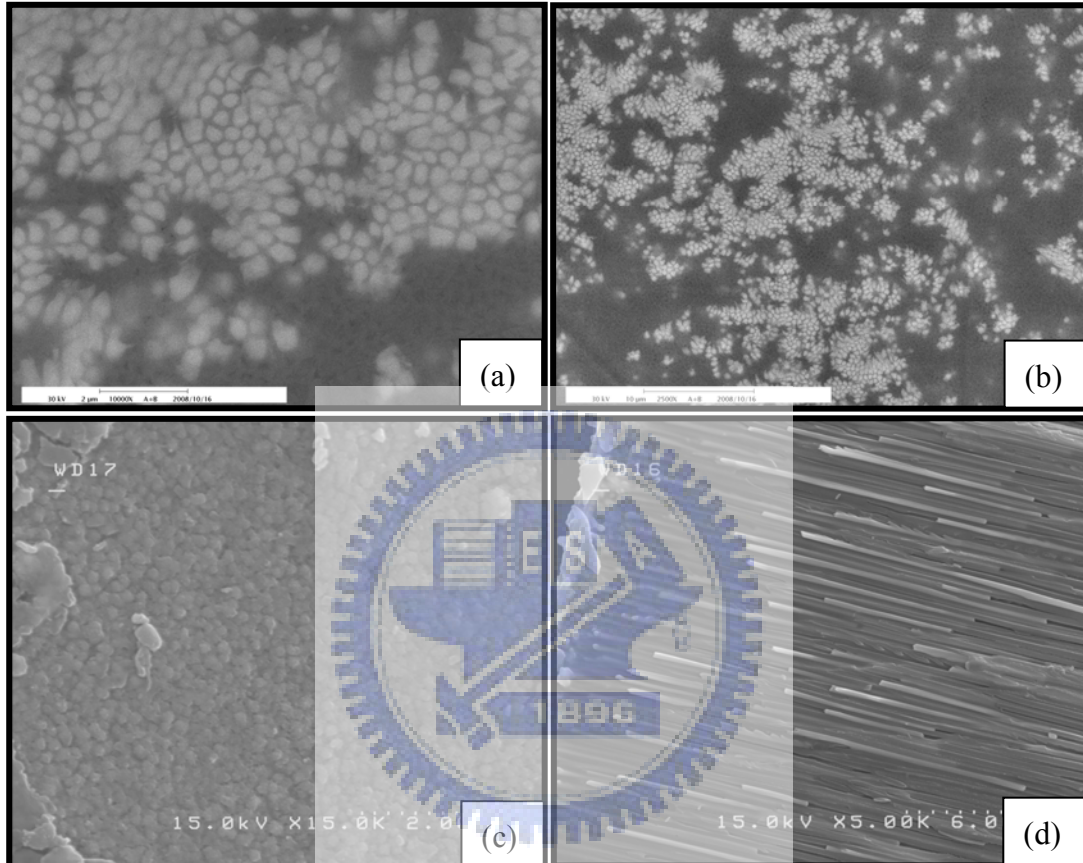
Figure 5.4 SEM images of the iron-filled AAOtemplates with pore diameter about 200 nm.   Images are (a) and (b) the top view by different magnification after mechanical polish of 200 nm template, (c) the top view without mechanical polish, and (d) the side view.   The white spots and color indicate the filling of iron.
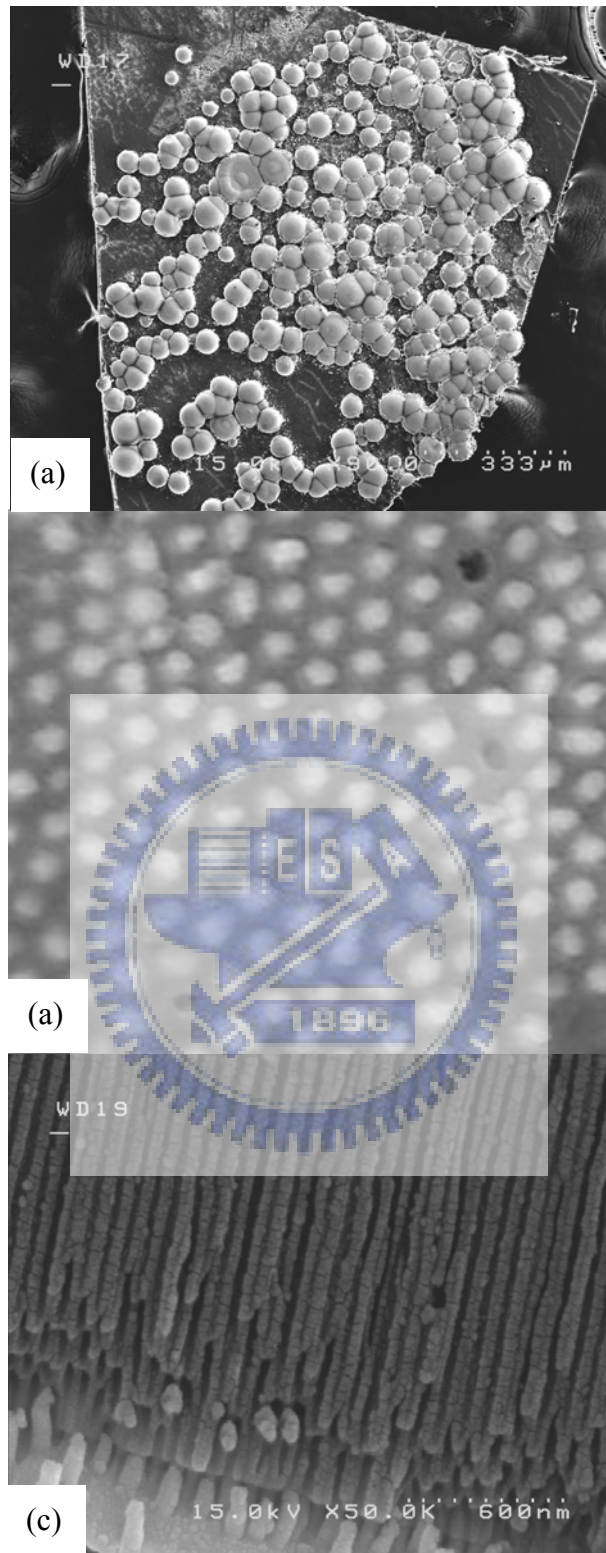
Figure 5.5 SEM images of the iron-filled AAO templates with pore diameter about 60 nm. Images are (a) the top view of as grow one, (b) the top view after mechanical polish, and (c) the side view. The white spots and color indicate the filling of iron.
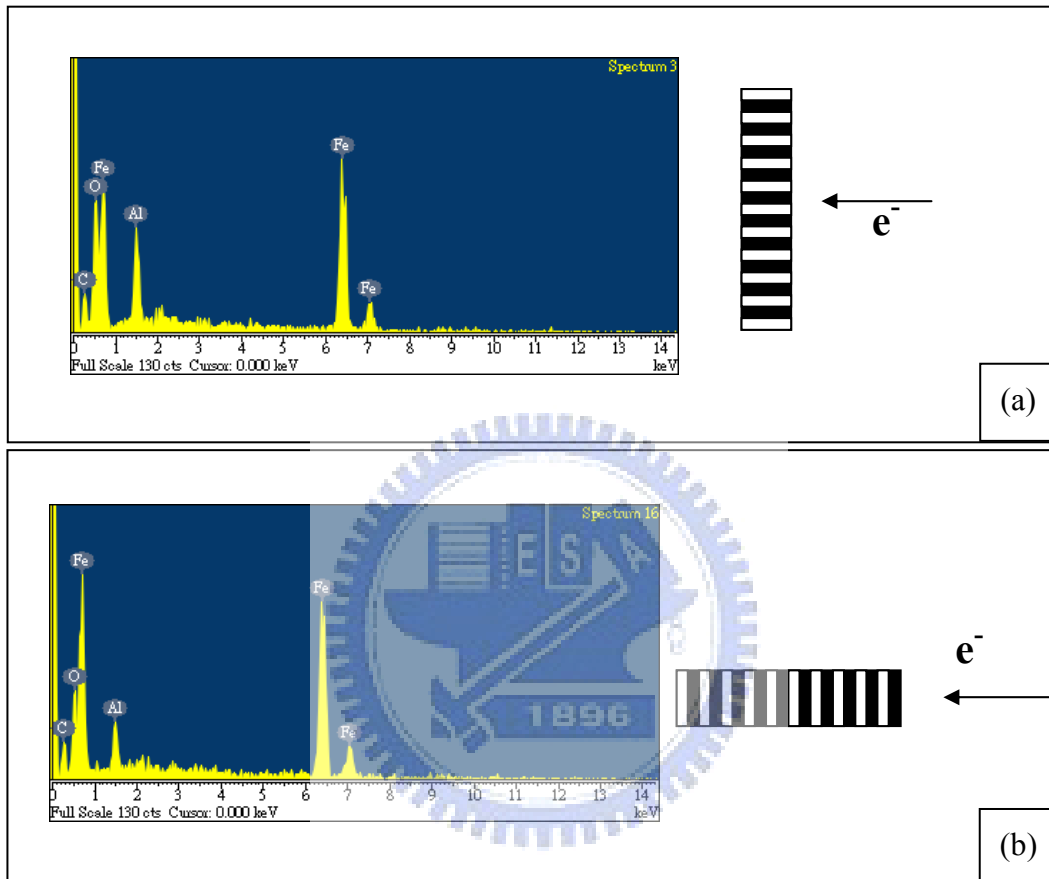
Figure 5.6 The EDS of imbedded iron nanowires. Inset (a) and are the electrons spotting on top and side of AAO respectively.

5.2.2   XRD of Imbedded FeNWs in AAO

The x-ray diffraction was carried out to examine the composition and texture of the NWs (Figure 5.7).   For 200 nm Fe NWs the diffraction peaks were identified to be the (110), (200) and (211) planes of α-Fe, the result indicates 200 nm Fe NW are poly-crystal material, whereas 60 nm Fe NW shows a strong diffraction peak corresponding to the [110], indicating a preferred orientation along the longitudinal axis [99].
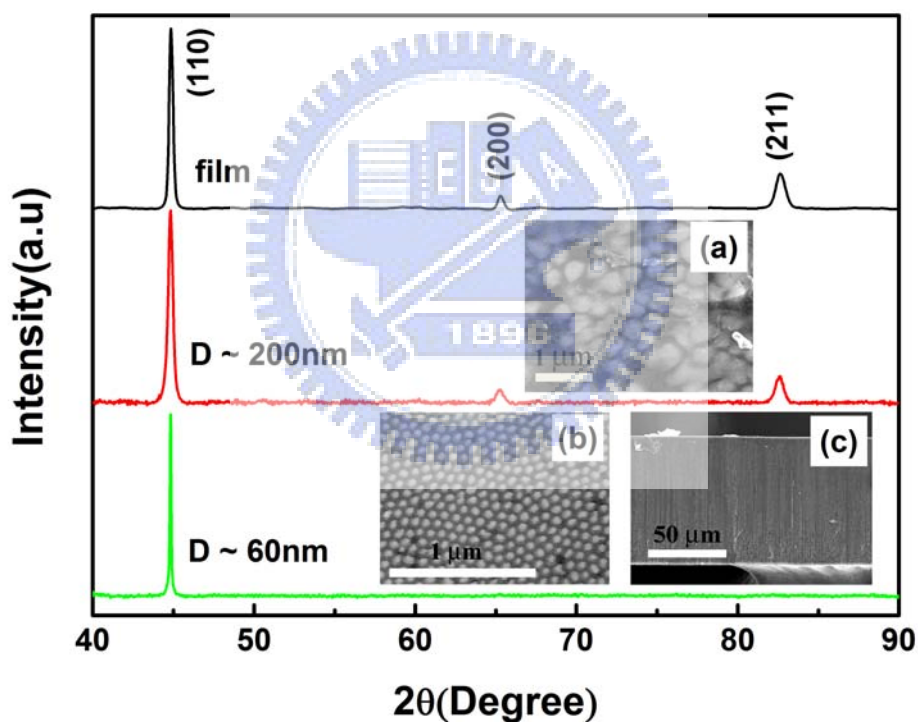
Figure 5.7 X-ray diffraction patterns of film, 200-nm, and 60-nm NWs.   Insets (a) and (b) are the Crosse section view of 200 and 60 nm NW arrays respectively. The white spots represent the nano-pores filled with α-Fe. Inset (c) is the side view of home-made empty AAO template.

5.2.3 Electronic transport properties

For the study of the electrical transport properties of the NW arrays, four platinum wires were connected to both sides of AAO with silver paste. The arrangement of those four wires is going to form a four-probe method connection, which shows in figure 5.8.
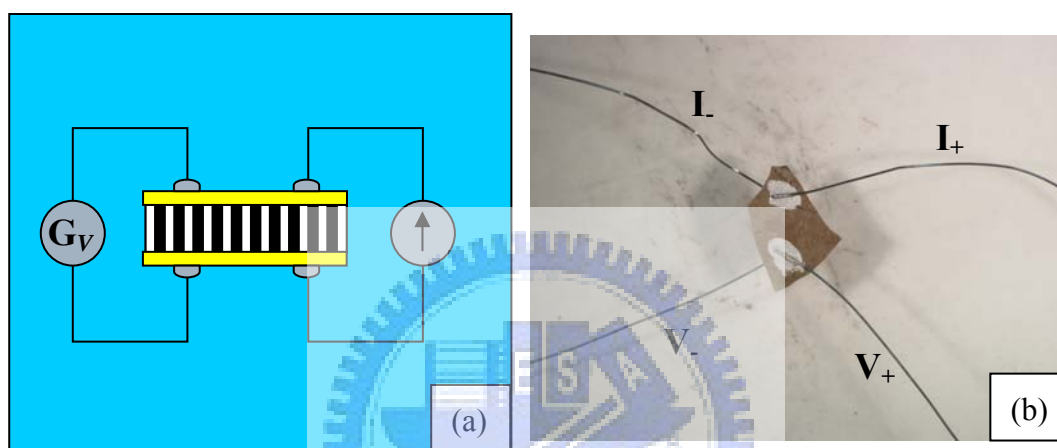
Figure 5.8 Arrangement of electrodes. (a) is the sketch of 4-probe method for the imbedded iron nanowires, while the (b) is the real image of this sample.

The electrical transport properties were investigated with above quasi four-probe setup. The Figure 5.8(a) shows a sketch measurement design, in which the 200nm thick gold layers at both top and bottom work as the electrodes. The thickness ratio between electrode and AAM is around 0.01 to 0.001, so that the contribution of electrode resistance can be neglected. The resistivity ρ ~0.01 $\Omega \cdot$ cm of 200-nm FeNWs array is about 1000 times that of bulk Fe. A temperature dependence resistance result was shown in Figure 5.9.
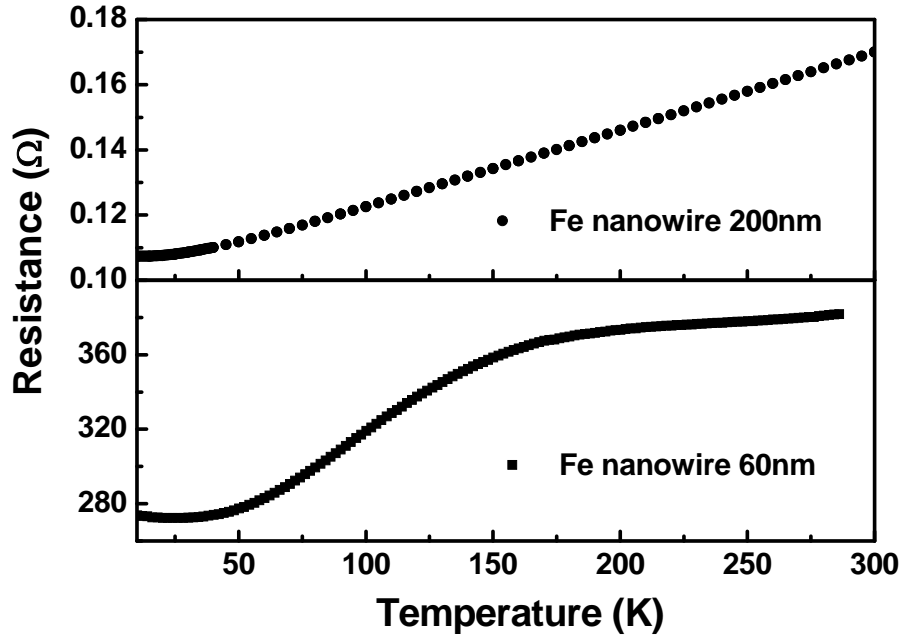
Figure 5.9 The resistance of 60-nm and 200-nm nanowires measured with quasi-four probe.

The magneto-transport properties were investigated by the Quantum Design Physical Property Measurement System (PPMS) with the sketch of connection condition in the inset (a) of Figure 5.10. The measurement of magneto-resistance is performed with the applied magnetic field perpendicular to the long axis. In the arrangement, electric current is perpendicular to the applied magnetic field. The calculation of magnetoresistance (MR) is performed with formula

$$MR = \frac{R(H) - R_0}{R_0} \times 100\%,$$
(5.1)

where $R(H)$ and R_0 represent the resistance with and without magnetic field, respectively. The obtained MR curves are mainly attributed to the anisotropic magnetoresistance (AMR) in low-dimensional systems. The AMR is caused by an anisotropic scattering of electrons with strong dependence on the orientation of the external magnetic field relative to the current direction. This consequence originates from the spin-orbit interaction.

The value of MR ratio of 60 nm NW arrays is about 5 times higher than that of

73

the 200 nm one at 5 Tesla. This can be attributed to the existence of additional scatterings related to various spin-diffusion mechanisms, which strongly depend on disorder and grain-boundary conditions [100]. The field dependent resistance change due to AMR in the transverse case can be described as [101]

$$R(H) - R_0 = -\Delta R \frac{M_S^2}{4K^2} H^2 , \qquad (5.2)$$

where R_0 is the maximum resistance , ΔR is the absolute resistance variation defined as |R(5T)-R(0)| , M_S is the saturation magnetic moment, and K is the shape anisotropy energy constant.   The normalized MR ratio (MR/ΔR) is shown in the inset (b) of Figure 5.10.   The data of 60 nm are better fitted to the equation (2), indicating that the anisotropy constant in 60 nm is higher than that of 200 nm NWs.
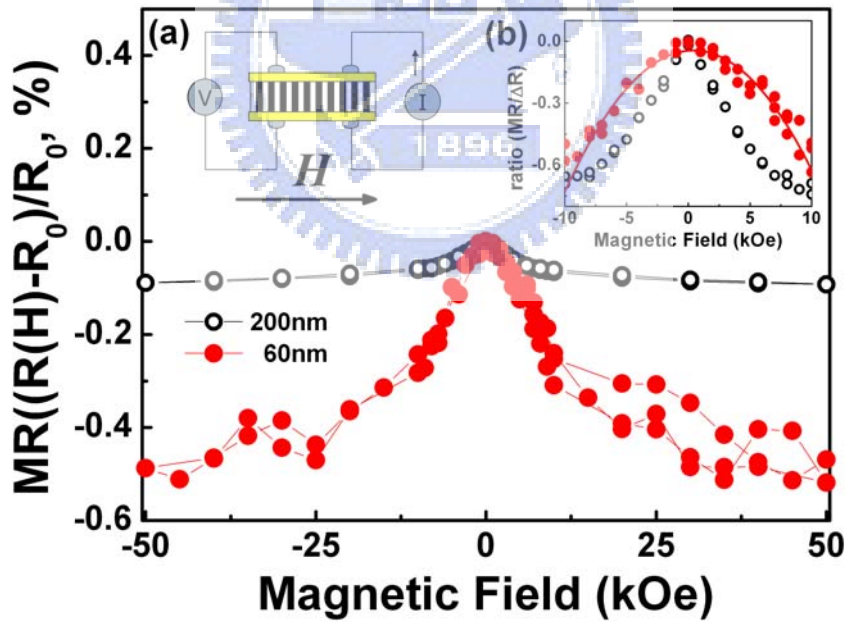
Figure 5.10 Magneto-resistance of NW arrays, with the current applied on longitudinal axis of Fe NWs and perpendicular to applied magnetic field. Inset (a): transport measurement setup. The 200 nm gold layers are deposited onto both top and bottom sides of samples to serve as the electrodes. Inset (b): the normalized MR/ΔR ratio of 60 and 200-nm NWs.   The parabolic fitting based on Eq. (2) for 60-nm NWs is represented by the solid line.

5.2.4　Magnetic properties

In order to study the magnetization without the influence of electrodes, both side of AAO were polished to remove the gold film contacts. The size effects on magnetism of Fe NWs were investigated by Quantum Design Magnetic Property Measurement System (MPMS). The hysteresis loops for the Fe NW arrays at 300 K are shown in Fig 5.11. The 60 nm Fe NWs array shows stronger hysteresis and anisotropic behaviors, revealed by the larger difference between magnetization data of field parallel and perpendicular to the axis as compared with that of 200 nm NWs. These results arise from the fact of the magnetic easy axis and preferred crystal orientation of [110] along the longitudinal direction of NWs, which originated from the line shape anisotropy and the large aspect ratios in NWs. The aspect ratios are calculated to be 300 and 1300 for 200 nm and 60 nm respectively.

As an external perpendicular magnetic field is applied to 60 and 200 nm NWs, magnetization was saturated for 200 nm NWs as field up to 1 Tesla, but not for the 60 NWs. The explanation is that for large-diameter NWs, the square ratio and the coercive force decrease appreciably due to the smaller anisotropy and the formation of a multi-domain structure. Interaction between NWs in dense NW arrays should not be disregarded also, because of possibility of appearing (as a result of the interaction) of large demagnetization fields keeping the moments along the longitudinal axis. The hysteresis loops shows that the coercive fields in easy axis (along the longitudinal direction of NWs) are ~600 Oe and ~100 Oe for 60 nm and 200 nm NWs, respectively. The ratios of remanence (M_r) to saturation magnetization (M_S) are about 3% for 200 nm and 87 % for 60 nm NWs. The magnetization is thus concluded to be more stable in the longitudinal direction of NWs.
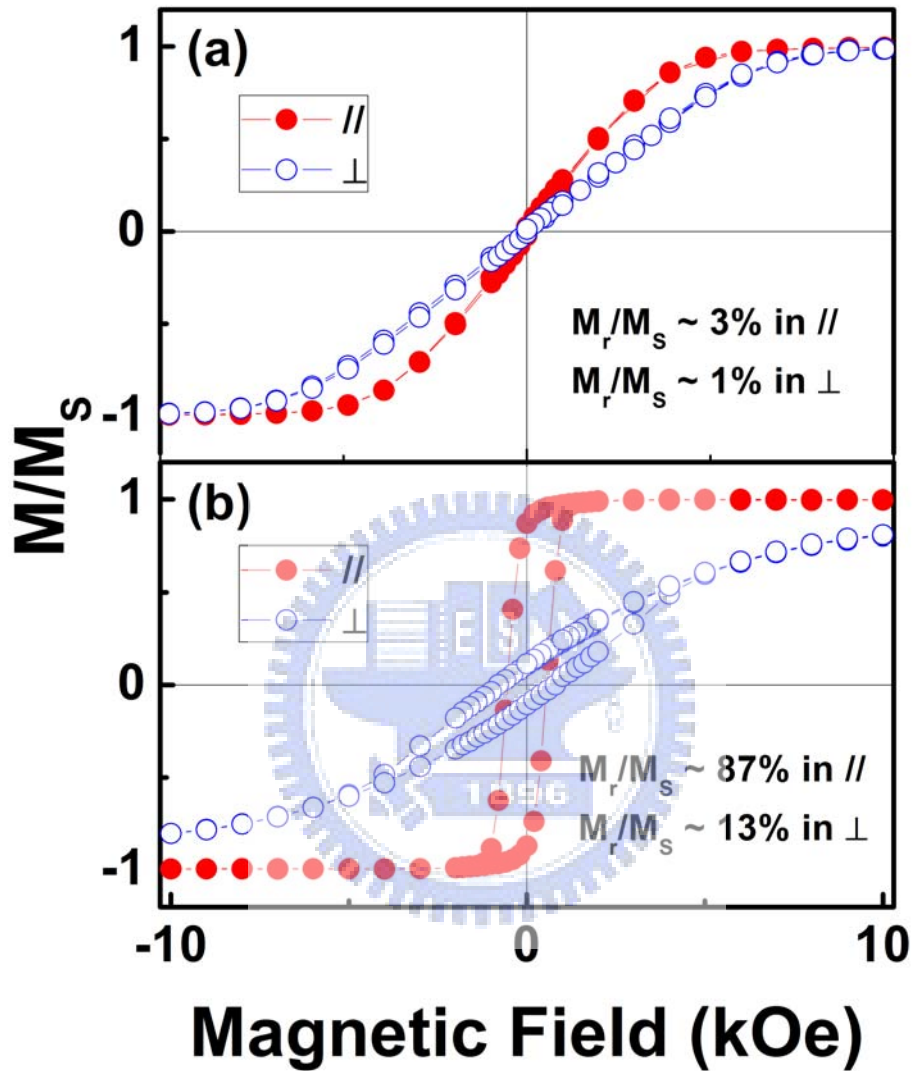
Figure 5.11 Hysteresis loops of the NW arrays with magnetic field parallel (//) and perpendicular (⊥) to longitudinal axis of NWs: (a) 200-nm and (b) 60-nm NWs.

5.3 A test for 3ω method: 3rd harmonic signal of Platinum wire

A commercially available platinum wire (purity~99.98%) with diameter D ~10 μm is used for verifying the 3ω method measurement.   By fitting with the frequency dependence $V_{3\omega}(t)$, the thermal conductivity was resulted by the calculation with equation 3.6.   Figure 5.12 shows a fitting result.   Table 5.1 shows a calculation result.
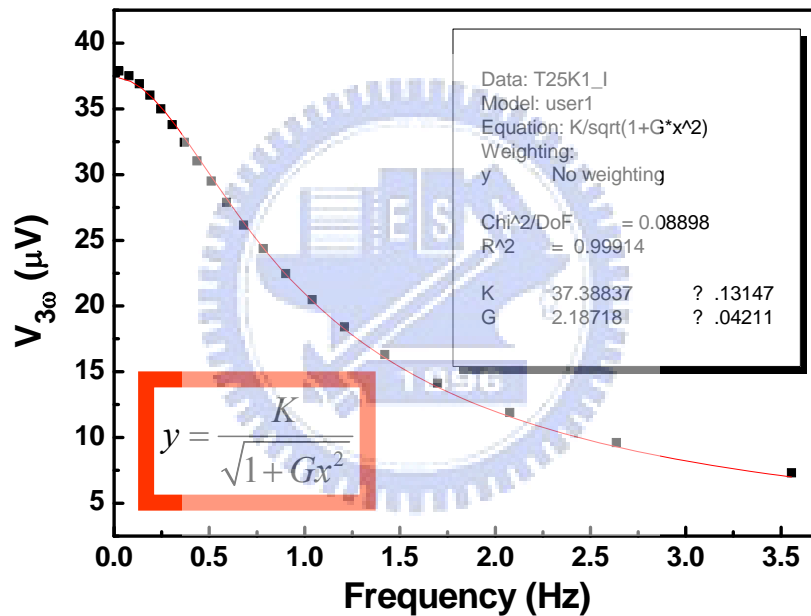
Figure 5.12 The frequency dependence 3ω-signal (T ~ 300 K) of platinum wire was fitted with inserted equation. Thermal conductivity κ and specific heat C_p can be calculated with two coefficients K and G.

TABLE 5.1 The calculate results for thermal conductivity and specific heat from the fitting parameters K and G in Figure 5.12.

T~300K	κ (W/m $\cdot$ K)	C_p (J/Kg $\cdot$ K)
Article	71	130
present	69	129

5.4　Individual nickel nanowire

5.4.1　Sample preparation and sagging structure constructing

　　The standards and details of optic and e-beam lithography methods were described in the section 4-2. Here shows the key steps of fabrication process in Figure 5.14 for the sagging single nickel nanowire (NiNW).

　　In order to measure thermal conductivity and specific heat with 3ω-method of an individual nanowire, there are some requisitions. Undoubtedly, middle part of the sample should separate from all other components to minimize heat leakage to allow the temperature fluctuation. For example, the heat could leak to substrate and environments by direct heat-contact and radiation. Furthermore, the end points of sample should highly thermal contact to substrate due to the requisition keeping the temperature of end parts same with that of substrate. The fabricating process for satisfying all measuring requisition will descript as follow to prepare the sagging individual nickel nanowire.

　　The primary substrate is a silicon-nitride coated p-type silicon wafer (Si_3N_4/Si),

which the out-plane orientation is silicon [1 0 0] plane.   The 200 nm thick Si_3N_4 film is an insulating layer to separate silicon substrate and sample.   Meanwhile, it's a resist layer to protect the silicon under silicon-nitride from the etching of KOH aqua. On this substrate, there are sixteen Ni/Pt electrodes on this substrate and it would be the primitive chip (Figure 5.13 a, b) for the following processes.

The pattern was defined with focused electron beam (E-Beam) on a clear and polymethyl methacrylate (PMMA)-coated primitive chip.   This pattern includes four wires, which each one was design for four-probe method.   The construction of each one includes one nano-ditch, two thin leads for signal picking up and two large leads for current injection.   As shows in Figure 5.13c, the design-dimension of nano-ditch is 35 μm in length, and 150 nm in width.   In order to prevent the influence of joule heating at the interface and current injection leading wire, the width of leading wire is about 50 times of nano-ditch to reduce the resistance of junctions and leading wires. Furthermore, also the nano-ditch takes about 8μm away from the junction to reduce the temperature fluctuation at the end parts of nanowire.

The next step, nickel would deposit onto the exposed and developed chip by thermal evaporator in the vacuum chamber with base pressure less than 1×10^{-6} torr at room temerature.   The followed lift-off process would take off the resist and the nickel upon this resist, the remained nickel form a nickel nanowire with four electrodes.   This result was shown at Figure 5.13d.   Before the next processes, this sample was taken to measure the resistance by four-probe method for circuit condition checking, and the observed resistance is about 750 Ω.   This pattern-defining process will repeat to form an etching window around the nanowire as figure 5.14b, and CF_4 would use to etch out the Si_3N_4 film in the windows area by RIE system.   Finally, the silicon in this window area would be etched and form a "V" shape groove, and the nickel would sag on the groove.   The sketch of detail steps for this sagging structure

is showed in figure 5.15.   The formed sagging nickel nanowire is about 35 μm in length, 180 nm in width, and 100 nm in thickness, which shows in Figure 5.16.   This junction-free connection of electrodes (the leads) prevents the undesirable heating of contact areas on the nanowire during the measurements.   Finally, although this sample goes through all the processes, the resistance of this sample is kept around 750 Ω.   This result implies that this procedure never changes neither the geometry and physical properties, nor the surface oxidation of NiNW.
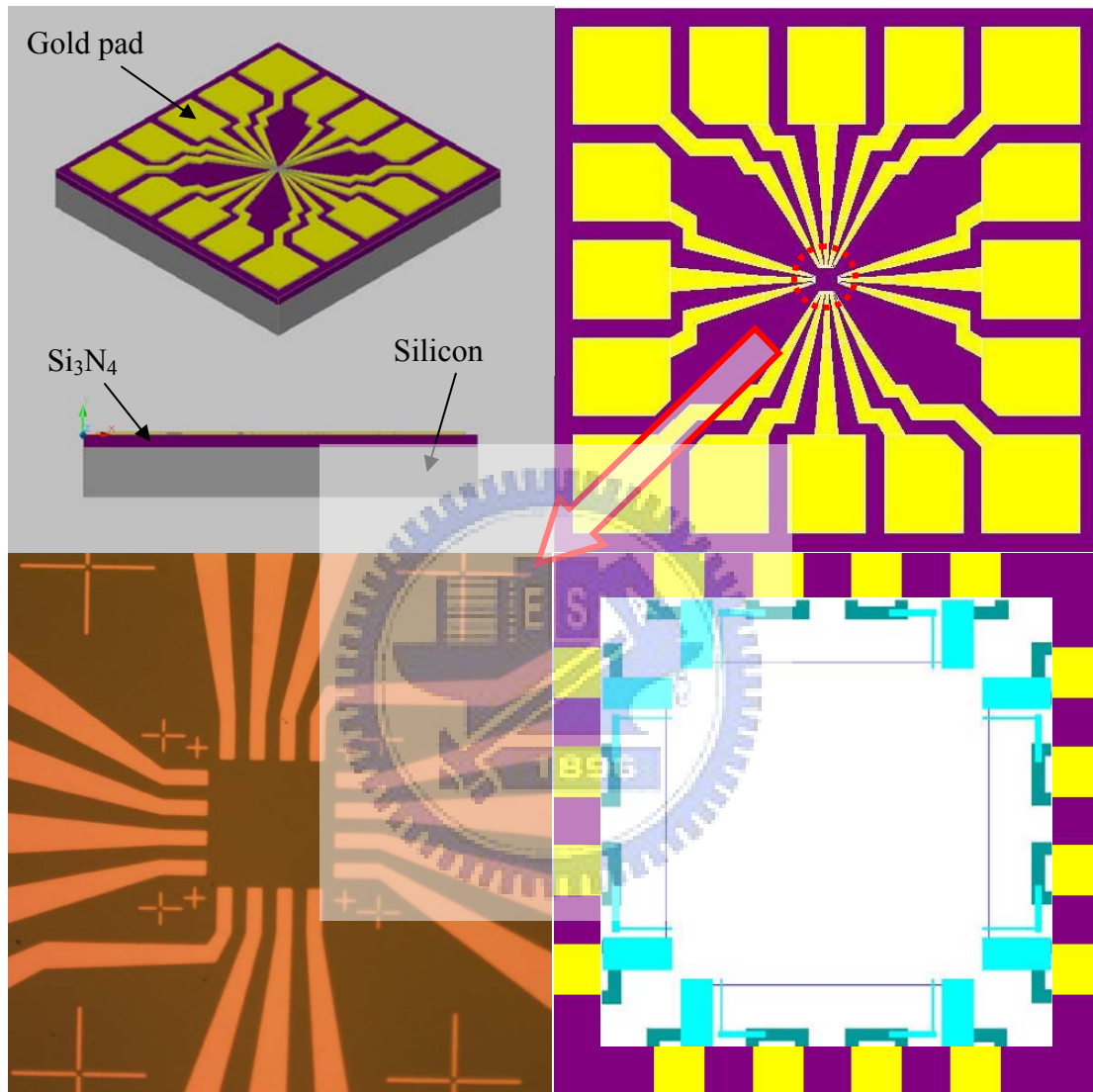
Figure 5.13 the diagram for primary chip and the patter design for NiNW.   They
are inset (a) and (b) the sketch for the primary chip, inset (c) the center image of
the primary chip, and (d) the four nano ditch pattern.
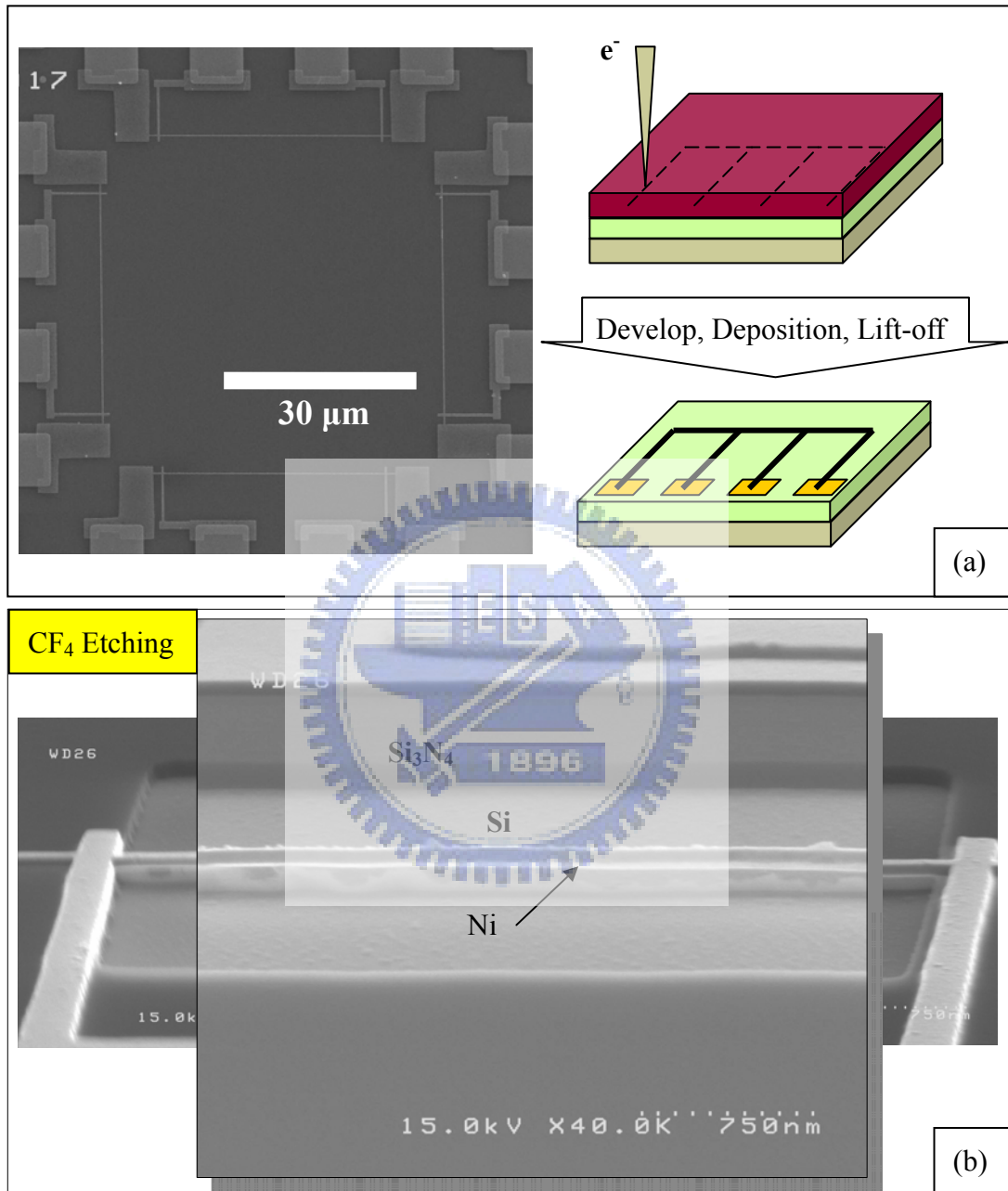
Figure 5.14 the pattern defined and etching results. Inset (a) shows the sequence of e-beam exposure, develop, deposition, and lift-off process. Inset (b) shows the etching results with CF_4 by RIE.
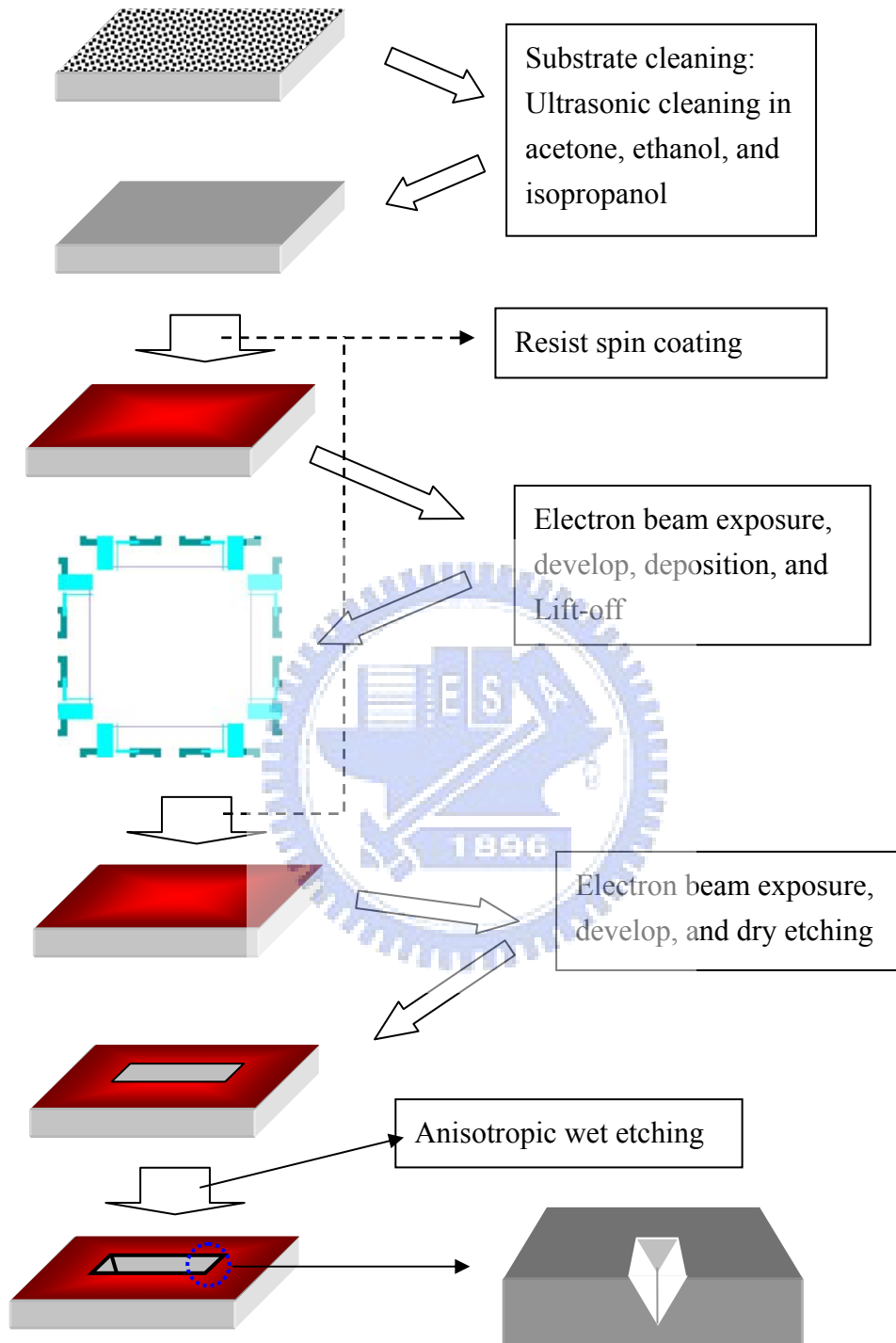
Figure 5.15 The detail steps of lithography and etching processes for the sagging nickel nanowire.
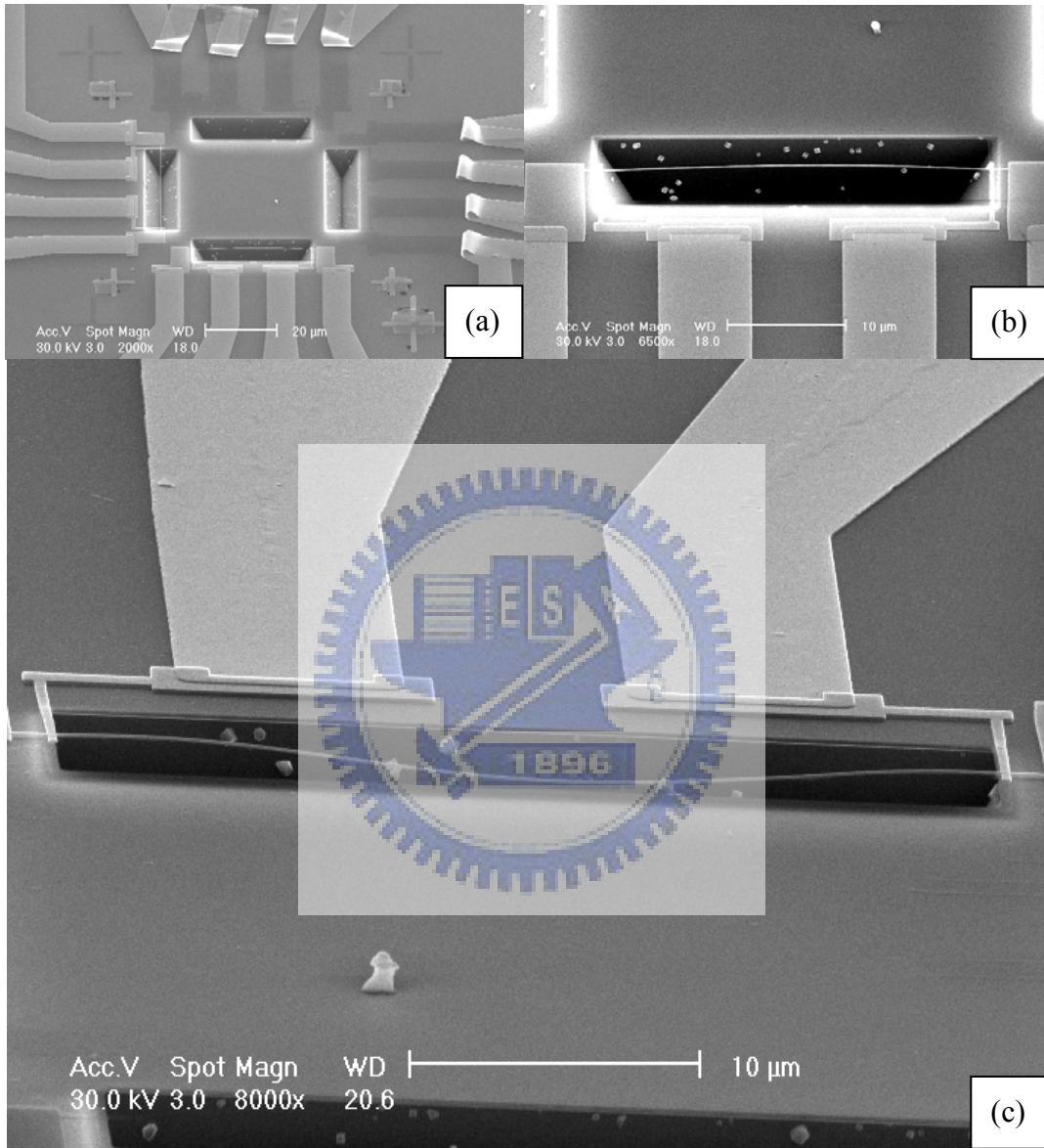
Figure 5.16 The SEM image of sagging Ni-NW with dimensions 100 nm in thickness, 180 nm in width, and 35 μm in length. Inset (a) and (b) are the top view with different magnification. Inset (c) is the image at the tile angle 45°.

5.4.2   Electronic and thermal Transport Properties

The electrical conductivity and thermodynamic properties of the nanowire was measured by four-probe and self-heating method, respectively.   The sample holder was arranged on a ^{3}He-refrigerator probe to form a measurement setup as showing in Figure 3.2, which provides a variable and stable temperature control system with high vacuum environment.

Electronic transport properties

The arrangement of measuring circuit shows as Figure 5.17, which the current was injected through two outside electrode, and the gauge pick up voltage drop from two inside electrodes.   An applied current dependent voltage was shown in Figure 5.18 for illuminate.   The voltage drop in the current range 1 ~ 50 µA shows a linear dependence without any anomaly.   The measurement of electrical conductivity was excited by a constant alternating current about 1 µA, where it is a sine wave $I_0=\sin(\omega t)$ profile with constant frequency f = 15.3 Hz.   Meanwhile, the corresponding in phase voltage signal with same reference frequency was pickup by the lock-in amplifier.

The experimental data of resistivity ρ of the Ni-NW in the temperature region of 0.5 - 300 K are showed in Figure 5.19 and 5.20.   The metallic temperature dependence of resistivity is similar to the bulk but with a larger magnitude of resistivity.   The relative ratio of resistivity ρ(300 K)/ρ(4.2 K) = 2 is much smaller as compared to the value of 47 for the bulk.   Since the wire dimensions are much larger than the *mfp* of Ni (~14nm) [102], the increase in resistivity is conjectured to be the predominant effect of the grain–boundary scattering.   The temperature coefficient of resistivity (TCR) is positive in the whole temperature range (Figure 5.19), indicating that the Ni-NW is weakly disordered.   At low temperatures T < 10 K, the

temperature dependence of resistivity can be formulated as $\rho=\rho_0+T^n$, with the power n ~ 2 (inset in Figure 5.20).　The consequence is similar to that of the bulk [26], except the magnitude of residual resistivity ρ_0=17.6 $\mu\Omega$-cm is much larger than that of bulk Ni.　The huge residual resistivity indicates an enhanced electronic scattering on interfacial boundaries and defects.
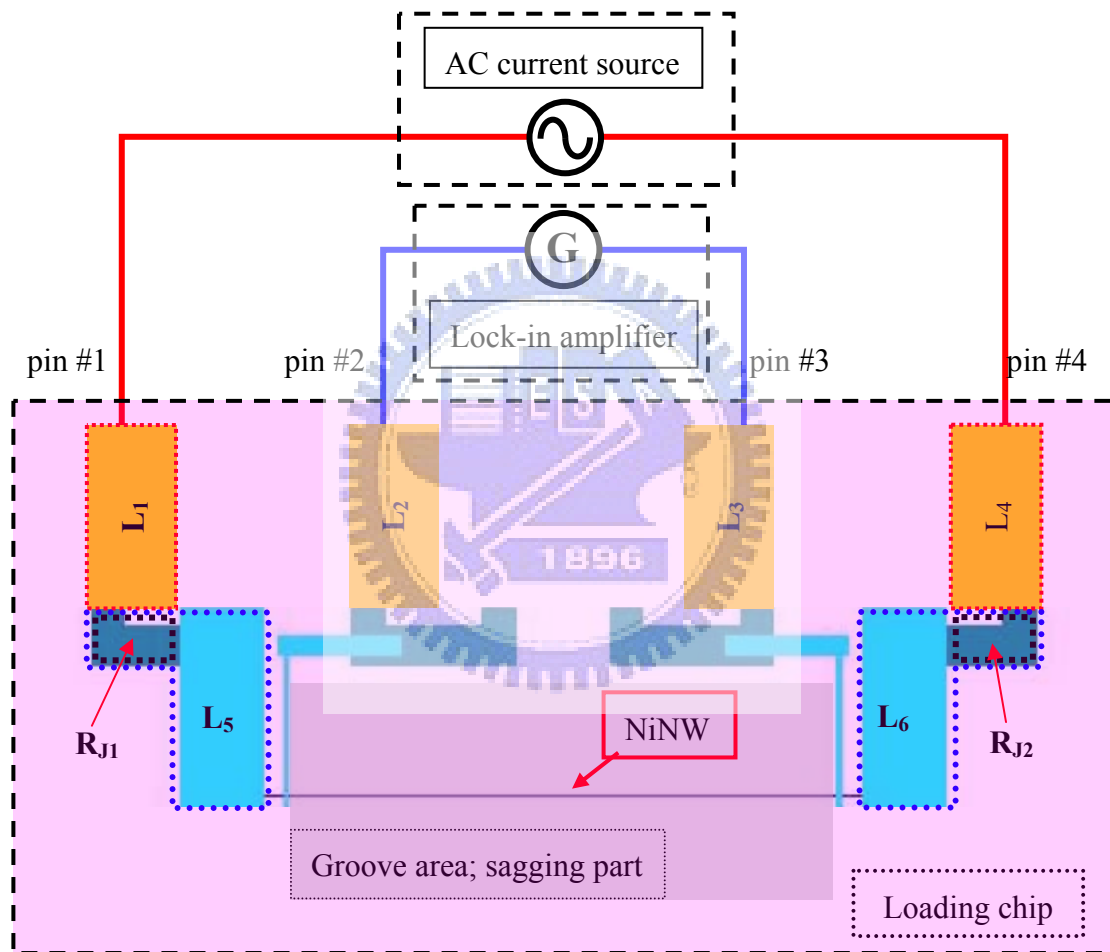
Figure 5.17 The sketch of the measurement arrangement for both electrical and thermodynamic properties.　L_5 and L_6 is the nickel leading pad, which there is not junction in each pad, although it is denoted in two different colors. L_1, L_2, L_3 and L_4 is the gold leading pad. There are two junctions presented. One locates at the interface between L_1 and L_5, and the other one between L_6 and L_4.
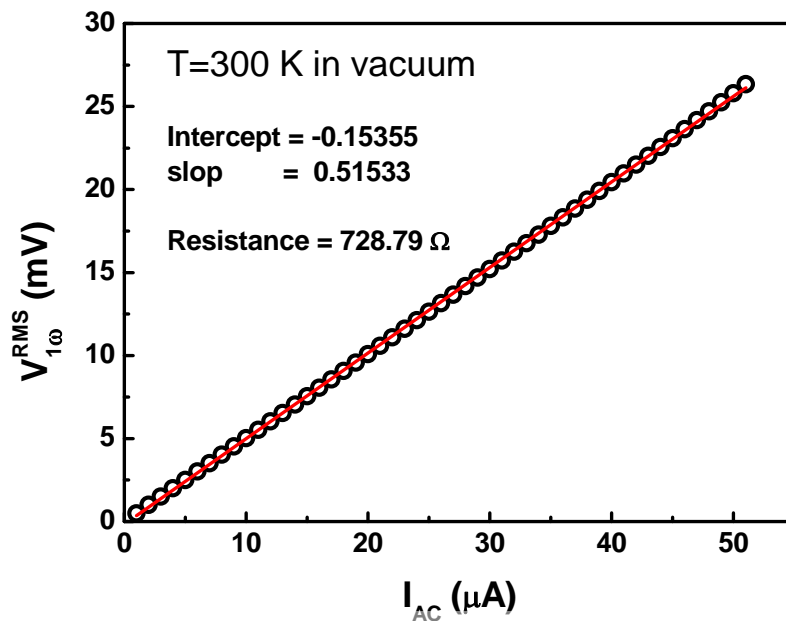
Figure 5.18 The current dependence of 1st harmonic signal. Open circle is the data. Solid line is the fitting result.
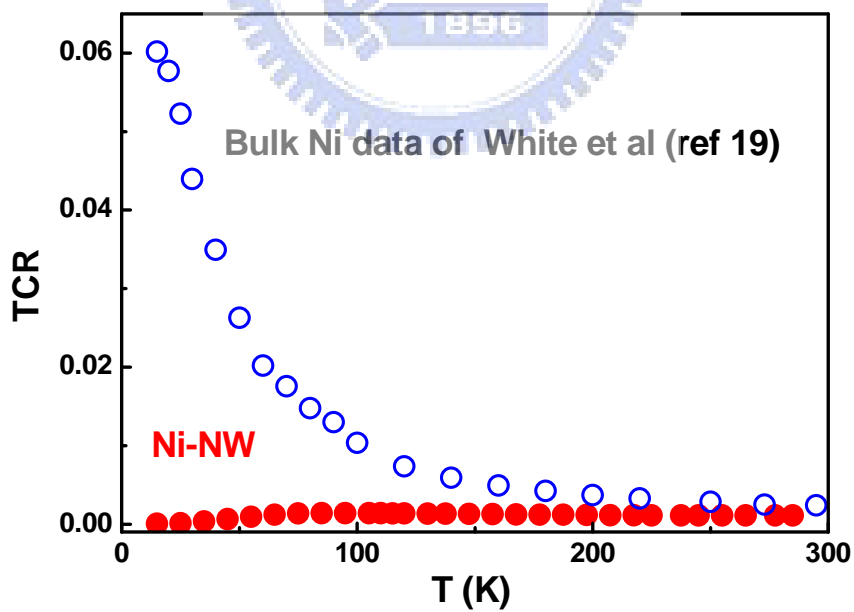
Figure 5.19 The temperature coefficient of the NiNW (solid circle) is much small than that of bulk, meanwhile the trend them are totally different.
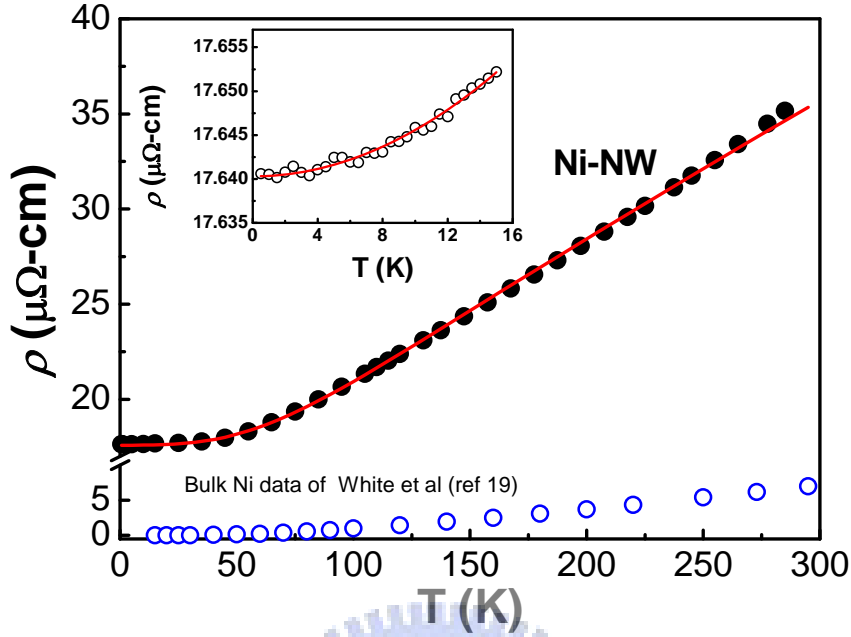
Figure 5.20 The resistivity $\rho(T)$ of the Ni-NW (solid circles) and the bulk (open circles) from White et al. The solid line is the fitting results by Bloch-Gruneisen formula. Inset: the resistivity in low temperature range, which is agreed with the T^2 fitting curve (solid line in inset).

It is necessary to note that the $\rho(T)$ curve of our Ni nanowire are still good fitted by Bloch-Gruneisen formula modified by Wilson [103] for transition metals

$$\rho_i(sd) = d(\frac{T}{\theta_D})^3 \int_{\theta_E/T}^{\theta_D/T} \frac{x^3 dx}{(e^x - 1)(1 - e^{-x})} = d(\frac{T}{\theta_D})^3 J_3(\frac{\theta}{T}),$$

using Debye temperature θ_D and constant d as the only two adjustable fit parameters. As a result of the fitting we obtained the smaller value of $\theta_D = 440$ K at fixed d than that is in case of the bulk (θ_D= 557 K). The reduction of the value of Debye temperature is presumably the reflection of softening of vibration mode of nanowire compare to bulk sample due to enhanced disorder in nanowire. The reduction of θ_D and softening of vibration mode have been observed previously for nanowires and disordered systems [104-106]. In particular, measurements of phonon density of states (DOS) of nanocrystalline Fe [105] and Ni_3Fe [106] by means of inelastic

88

nuclear scattering shows enlargement of low energy part of phonon DOS curve and smearing of high energy peak. Our obtained trend of Debye temperature and modification of the DOS of nanonocristalline materials are indicating that for this material the heat capacity can be enhanced compare to bulk samples.

The magnetoresistance behavior of Ni-NW is shown in Figure 5.21, the behavior of magnetoresistance is likely due to the contributions of many effects which include Lorentz-MR, spin-dependent scattering, and anisotropic magnetoresistance (AMR). The MR-ratio calculated by formula (R(1T)-R(0))/R(0) is about 0.002. The smooth resistance decrease for H<Hc indicates a magnetization reversal process that incorporates a multidomain state of the magnetization. The peak value of magnetic field indicates that the coercive field is about 500Oe.
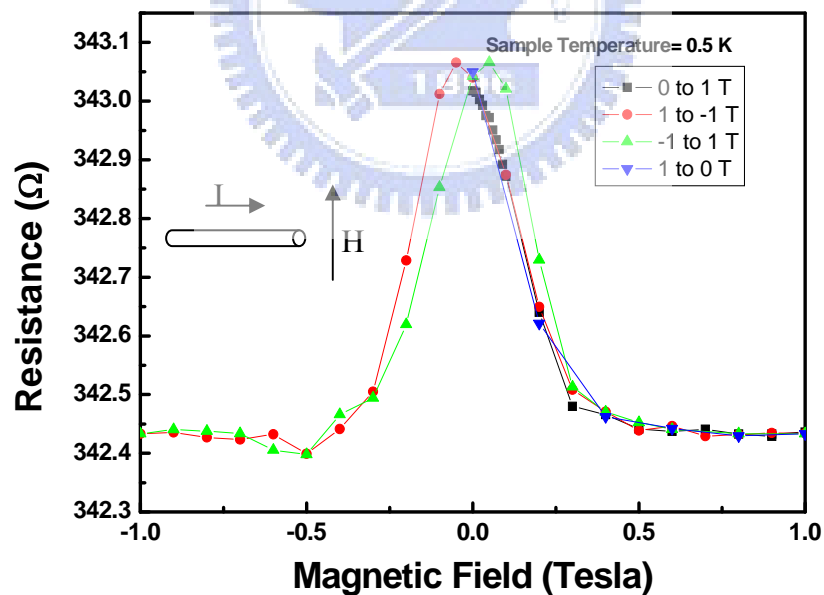
Figure 5.21 The magnetoresistance of Ni-NW with magnetic field perpendicular to applied current.

Thermal transport properties

Usually, the various properties ($\kappa(T)$, $\sigma(T)$, $C(T)$) are measured by different instruments even using the different specimen. In the applied 3ω-method [11] the three dependencies are measured on the same specimen and at the same moment and environment. Although the nanowire still exhibits metallic behavior in $\rho(T)$, the situation in thermal conductivity is changed drastically. The sketch of measurement connection and arrangement of instruments were showed in Figure 5.17 and Figure 3.2 respectively, which same as the setup for resistance measurement. The whole set of base and specimen are placed in an OXFORD He^3-refrigerator probe also.

Before we applied 3ω technique to study thermodynamic properties of our sagging NiNW, the thermal condition should be considered. As showing in Figure 5.17, the path of applying current includes leads, junctions, and sample, since the totally counting resistance is the summary as

$$R_t = R_{L1} + R_{J1} + R_{L2} + R_{NiNW} + R_{L3} + R_{J2} + R_{L4}.$$

The total resistance R_t could be measured by two probe method. For illustration, one of our samples the R_t is 1370 Ω, and the R_{NiNW} is 706Ω, since the total resistance of leads and junction R_{L+J} of current path is 664 Ω. It isn't a neglect able value to compare with sample resistance R_{NiNW}. However, the power density of leading wire and NiNW is calculated with joule heating power P and volume V by the formula

$$D_{power} = \frac{P}{V} = \frac{I^2 R}{At},$$

where the I, R, A, and t is the applied current, resistance, area, and thickness, respectively. Since the passing current for leading wire and NiNW is the same, the power density ratio of leads and NiNW would be

$$\frac{D_{L+J}}{D_{NiNW}} = \frac{R_{L+J}V_{NiNW}}{R_{NiNW}V_{L+J}},$$

where L and J stands for leads and junctions, respectively. Due to the R_{L+J} equal to

R_{NiNW} probably, since the ratio of power density is the ratio of volume. The sample, what we are taken to perform the 3w measurement, the volume ratio of NiNW to leads is about 10^{-5}. Take the data from Table 5.2, the estimated power density of leads is about 10 ppm to that of NiNW, since it's ignorable of the joule heating on leads and junctions for measurement of 3ω method. A junction-free design has been made to prevent the measurement error which could be caused by unexpected temperature variation of contacts. In additional, the heating power of the sagging Ni-NW is about 1 ppm of non-sagging one. This fact indicates that the thermal conductance is good enough to transport the heat from NiNW to substrate. This fact also implies that the temperature of contact points should kept same with substrate.

TABLE 5.2 An illustration for the NiNW resistance R_{NiNW} between each pair of pins for 4-probe measurements at room temperature. The definition of pin number shows in Figure 5.17

	2-probe						4-probe
Pin #	1,2	1,3	1,4	2,3	2,4	3,4	1,2,3,4
R (Ω)	704	1370	1370	1390	1390	777	634

We have applied this 3ω technique on a sagging Ni-NW by just using the approximation solution 3.6. The electrical resistance of the former specimen has a positive temperature coefficient (Figure 5.19). There are two test measurements were performed at 10 and 300 K, respectively, for choosing an appropriate exciting current. Within appropriate ranges of frequency and current, we do find that $V_{3\omega} \propto I^3$ as showing in Figure 5.22 and 5.23. For these tests, the $V_{3\omega}$ is totally linear dependence to cubic current I^3 at 300 K as showing in inset of Figure 5.22, but the

condition is apparent different from that of the test at 10 K as showing in inset of Figure 5.23. Since, the I^3 dependent $V_{3\omega}$ is a little bending as the current lower than 20 µA at 10 K, so that the applied current should higher than 20µA. Furthermore, in order to reduce the measurement error due to the radiation loss, the applied current was chosen as 30µA.

For the pick up of $V_{3\omega}$ signal, a digital lock-in amplifier such as "Dual Phase DSP Lock-in Amplifier 7265" made by AMETEK, Inc. was selected. All the filters on the lock-in were turned off, and the dc coupled input mode was selected, to ensure the observation of a true frequency dependence of $V_{3\omega}$. Before measuring the 3ω signal, the phase of the lock-in amplifier was adjusted to zero according to the 1ω voltage component. The phase angle of $V_{3\omega}$ is then if R′>0 or 180°−φ if R′<0 according to Eq. 3.5. The 3ω component in the current was below 10^{-4} compared to its 1ω component. Because the 3ω voltage signal is deeply buried in the 1ω voltage signal, a certain amount of dynamic reservation is required for the lock in if, in order to keep the simplicity of this method, one is not using a bridge circuit to cancel out the 1ω signal. We kept the dynamic reservation unchanged relative to the total magnification of the lock in during the entire measurement.

Figure 5.24 shows the frequency dependencies of the amplitude at 15, 85, 155, 225, and 295 K, compared with the predicted functional forms (the solid lines) for illustration. By fitting the data in Figure 5.24 (a)-(e) to Eq. 3.6, we obtained the thermal conductivity κ and the thermal time constant γ. The thermal diffusivity and the specific heat of the specimen can be obtained by using the relations $\gamma=L^2/\pi^2\alpha$ and $\alpha=\kappa/\rho C_p$. Figure 5.24f gives the comparison for the fitting results at those five temperatures.
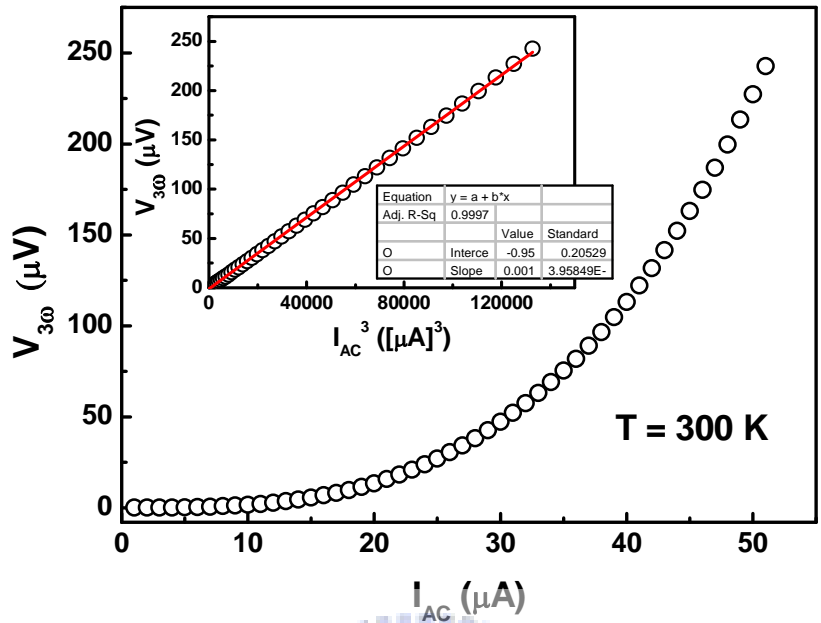
Figure 5.22 The current dependence 3rd harmonic signal at 300 K. The inset shows the linear dependence, which agree with equation 3.6.
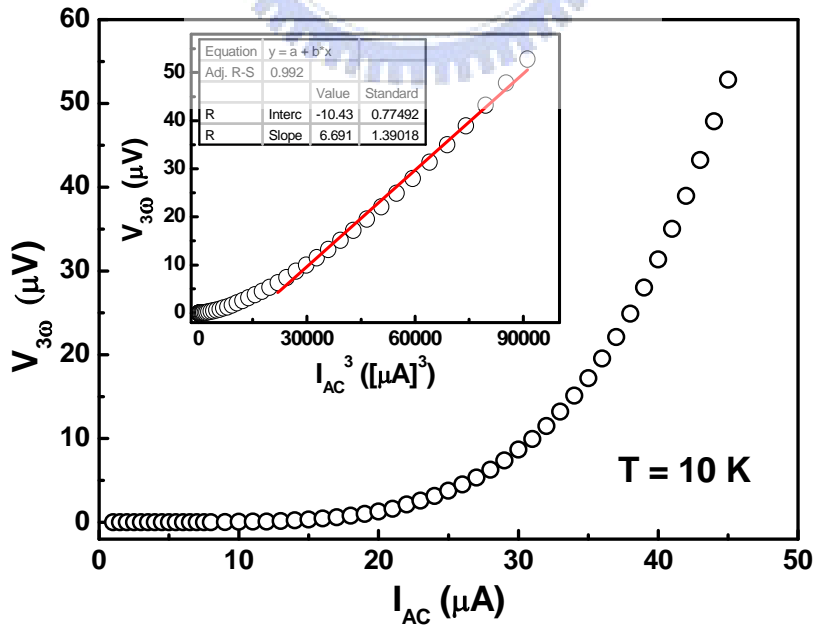
Figure 5.23 The current dependence 3rd harmonic signal at 10 K.
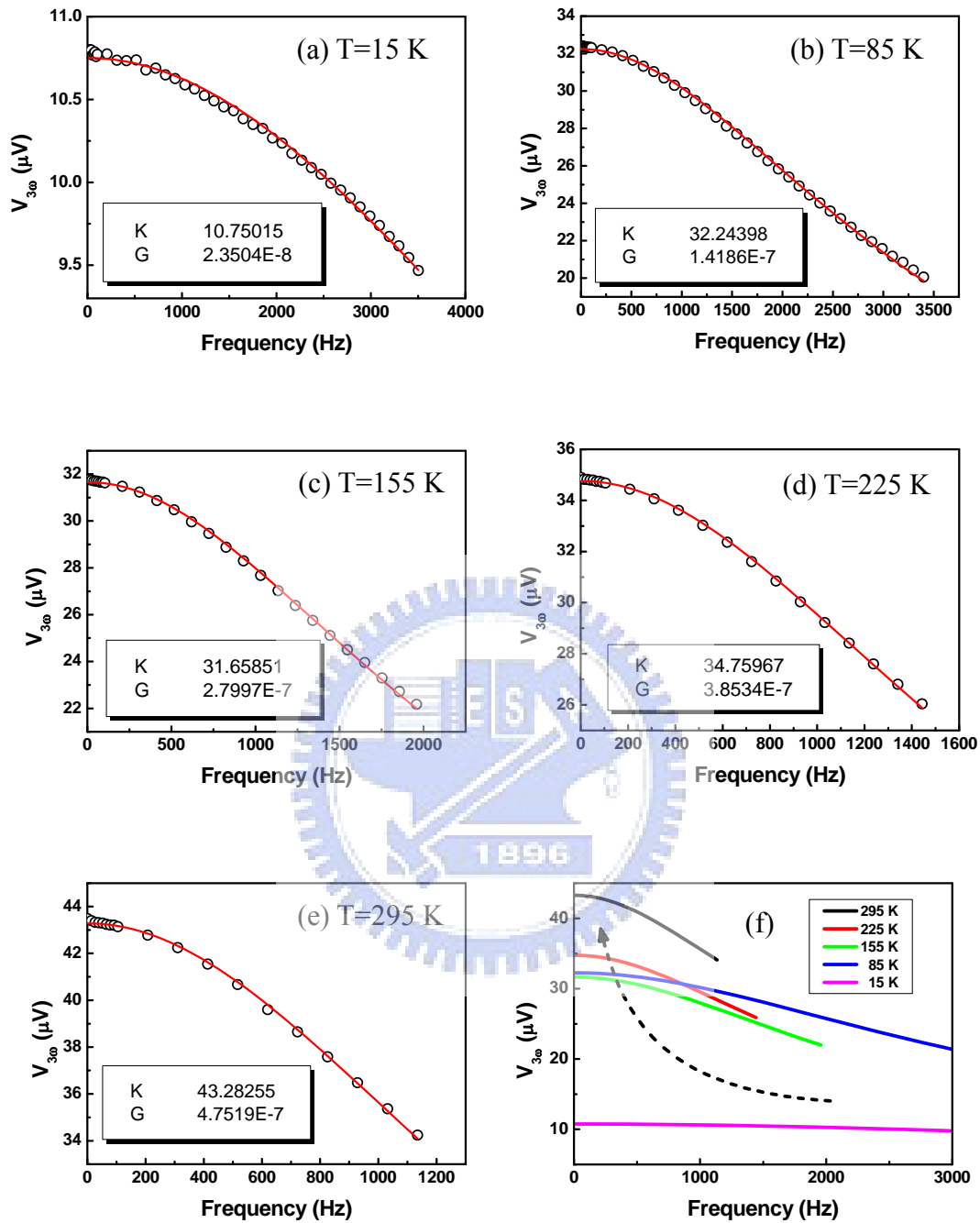
Figure 5.24 The frequency dependent 3rd harmonic signal. Insets (a) to (e) are five data performed at 15, 85, 155,225, and 295 K to show the dependence and the fitting results. Inset (f) collects those five fitting to show the trend of temperature relationship.

Figure 5.25 shows the experimental data of the thermal conductivity k in the temperature region of 15-300 K, representing a slight monotonic decrease of thermal conductivity with temperature decreasing. The much smaller $\kappa(T)$ of the nanowire completely differs from that of the bulk (inset of Figure 5.25) [108]. The phenomena of the metallic electrical resistivity and decreasing thermal conductivity have been observed in disordered metallic systems of thin films, glasses and concentrated alloys as well as in superlattices [109-112]. Such behavior was explained by increased scattering of heat carrier with the structural defects and by the substantial contribution of the phonon thermal conductivity. In general, thermal conductivity κ is the summation of electronic κ_E and phonon κ_{PH}. If the WF law holds, one can obtain the κ_E from the data of $\rho(T)$ through the relation $k_E = L_0 T/\rho$. The calculated κ_E for T< 60 K is larger than the experimental data κ_{total}, indicating the violation of the WF law in this temperature region (Figure 5.25). To estimate the phonon part of thermal conductivity κ_{PH} for T> 100 K, the κ_E was subtracted from experimental κ_{total}, the result of κ_{PH} does not exceed 10% of total thermal conductivity κ_{total}, and thus no considerable enhancement in the phonon part was observed at this temperature region (Fig.5.25).

To compare heat and charge currents the Lorenz number of the Ni-NW is calculated and plotted in Figure 5.26. It is known [112] that in pure metals at temperatures higher than Debye temperature (θ_D) the Lorenz number approaches the Sommerfeld value $L_0 = 2.45 \times 10^{-8}$ W-Ω/K^2 , at T < θ_D it falls below L0 and in the limit of low temperature region T→0 K, L returns to L_0 again. Such kind of behavior of L was observed for bulk nickel (Figure 5.26) [108, 113]. Unlike that of the bulk, Lorenz number of the Ni-NW is constant for 75 K< T < 300 K, although a little higher than the value of L_0, indicating both dominant electronic thermal conductivity kE and large-angle scattering events mostly caused by elastic scattering

at the grain boundaries. Based on the weak temperature dependence of electrical resistivity, the contribution to the thermal resistivity due to phonon scattering is relatively small. The small phonon thermal conductivity k_{PH} is likely the reason for the enhanced value of L in this temperature region. At T < 75 K when mfp become comparable with grain size and transverse dimension of the Ni-NW, the contribution of small-angle scattering (N-process) grows. The small-angle scatterings relax only the heat current, leaving the charge current relatively unaffected [114], which result in decreasing of the Lorenz number. Since the correction ΔL is the combined effects of positive contribution of the disorder ΔLdis and negative contribution of the small-angle scattering (ee interaction) ΔLee, the variation in L(T) is mainly depend on the relative weights of the two constituents.
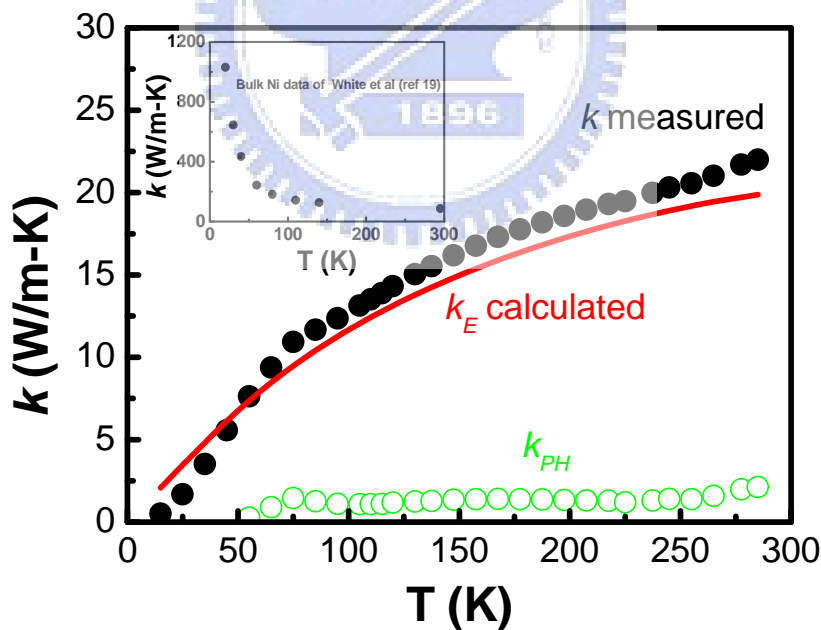
Figure 5.25 The thermal conductivity *k(T)* of the Ni-NW (solid circles), the calculated k_E (solid line) and the k_{PH} (open circles). Inset: the thermal conductivity *k(T)* of the pure bulk Ni [12].
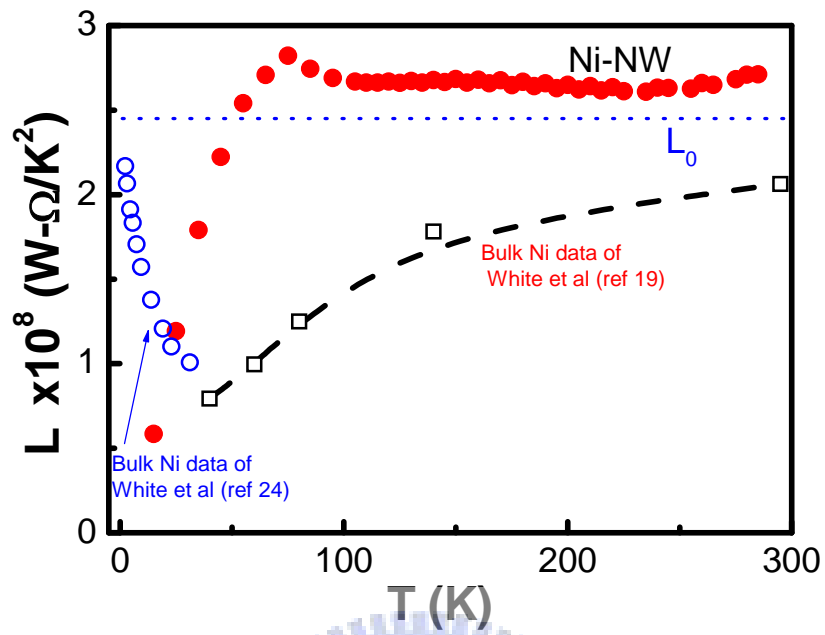
Figure 5.26 The Lorenz number *L(T)* of the Ni-NW (solid circles) and the pure bulk Ni (open circles) [108, 113].
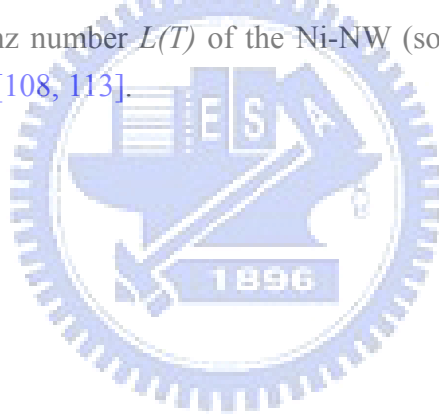
5.4.3 Specific heat

Figure 5.27 shows the measured heat capacity for our Ni nanowire. The heat capacity C_P behavior strongly differs from that of the bulk [115]. The temperature dependence of C_P at T>100 K comes close to the linear and the magnitude at room temperature exceed the bulk value 2.5 times. The additional specific heat may came from the contribution of lattice defects or grain boundaries which modify the phonon density of states as discussed above.
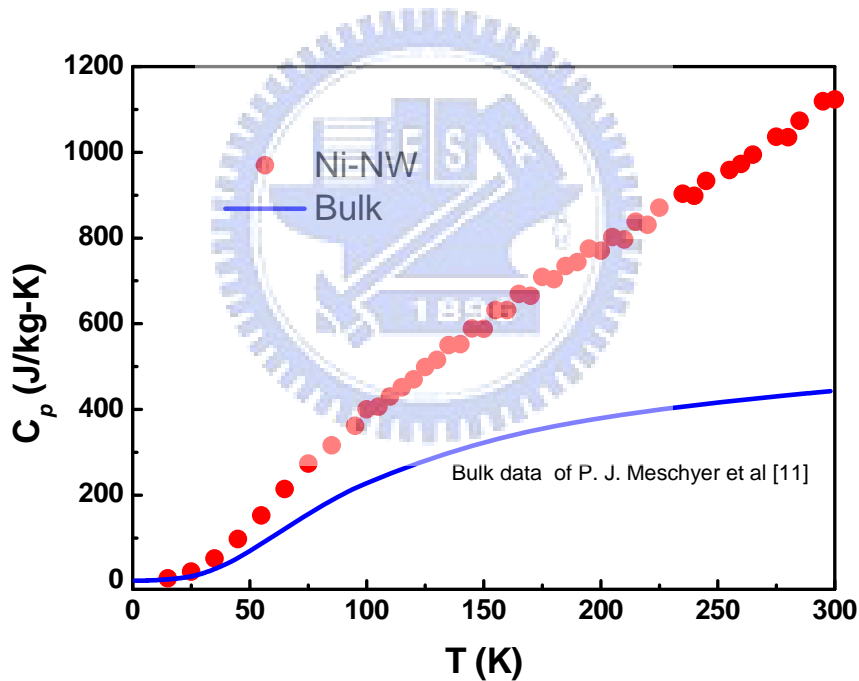
Figure 5.27 The specific heat of Ni-NW and the bulk.

5.5   Bi$_2$Te$_3$ nanowire

Two kinds of anodic alumina membrane (AAM) were used for growing Bi$_2$Te$_3$ nanowires.   One from the Whatman International Ltd. has a pore diameter D ~200 nm and length L ~60 μm.   The other one with D ~60 nm is homemade following a published procedure.   BiTe alloy was electrodeposited in the pores using cyclic voltammetry technique in a pH ~1 solution of [Bi^{3+}] (0.013M), [HTeO$_2^+$] (0.01 M) and HNO$_3$.   Deposition was carried out in -0.2 ~-0.005 V at room temperature, with platinum counter electrodes.

Using x-ray diffraction (XRD), scanning electron microscope (SEM), and energy-dispersive x-ray (EDX) the crystal structure, filling morphology, and composition were identified.   Figures 5.28, 5.29 show the details.   The Resistance measurement was done with a quasi-four probe method.   Figure 5.30 shows a 60-nm result. The e-beam lithography technology was used to make four electrode contacts on nanowire.   Figure 5.31 shows the result.
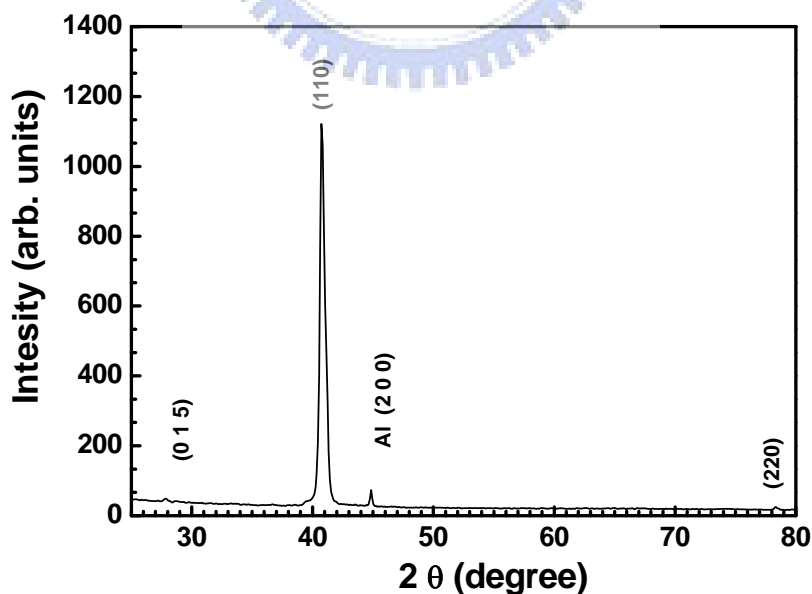
Figure 5.28 The XRD pattern of BiTe alloy with diameter ~60 nm. This result suggests a strong crystal texture, with the [110] direction aligned along the longitudinal axis.
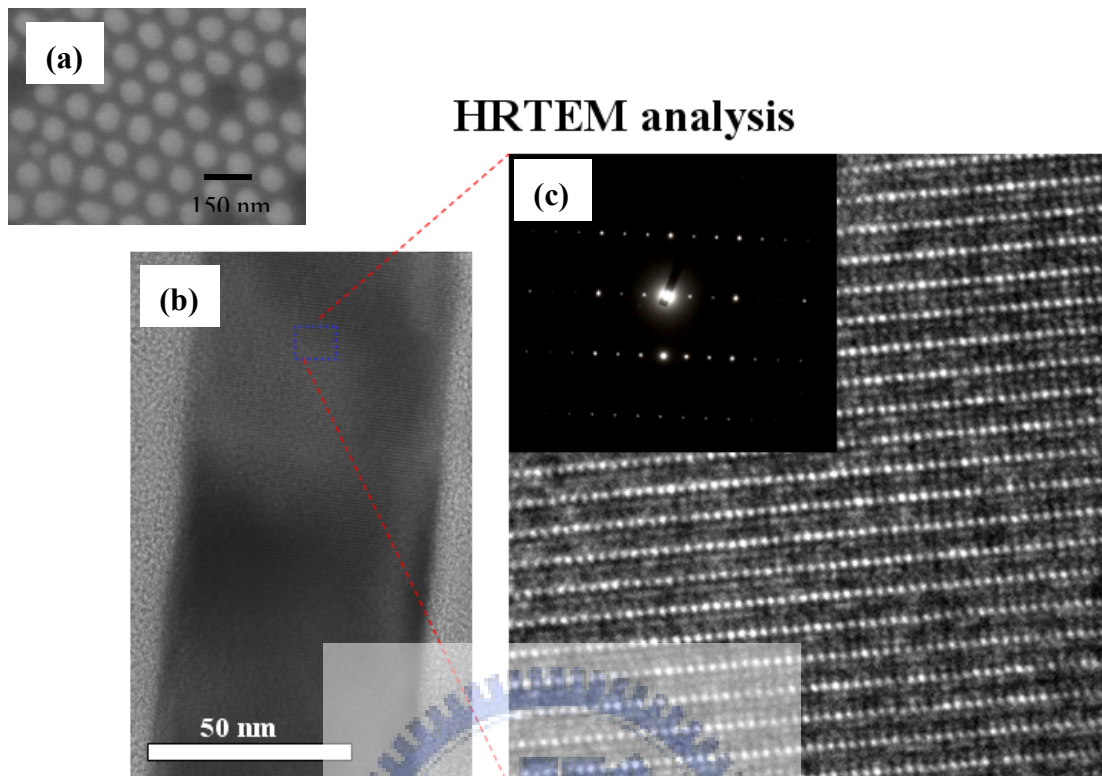
Figure 5.29 The High Resolution TEM analysis. (a) A top-view SEM image of 60-nm Bi$_2$Te$_3$-alloy nanowire. (b) and (c) are TEM images and electronic diffraction pattern of free-standing nanowire.
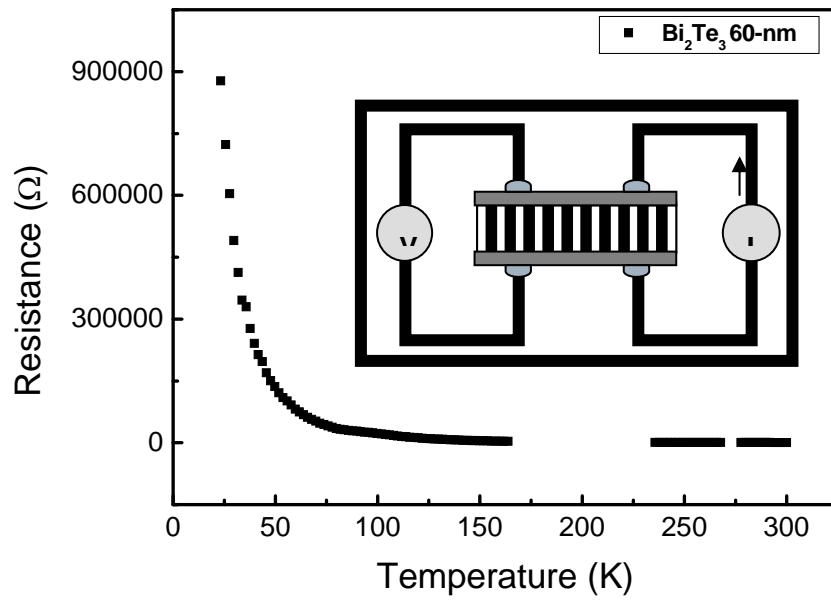
Figure 5.30   The resistance of BiTe-alloy nanowire with diameter ~60 nm.
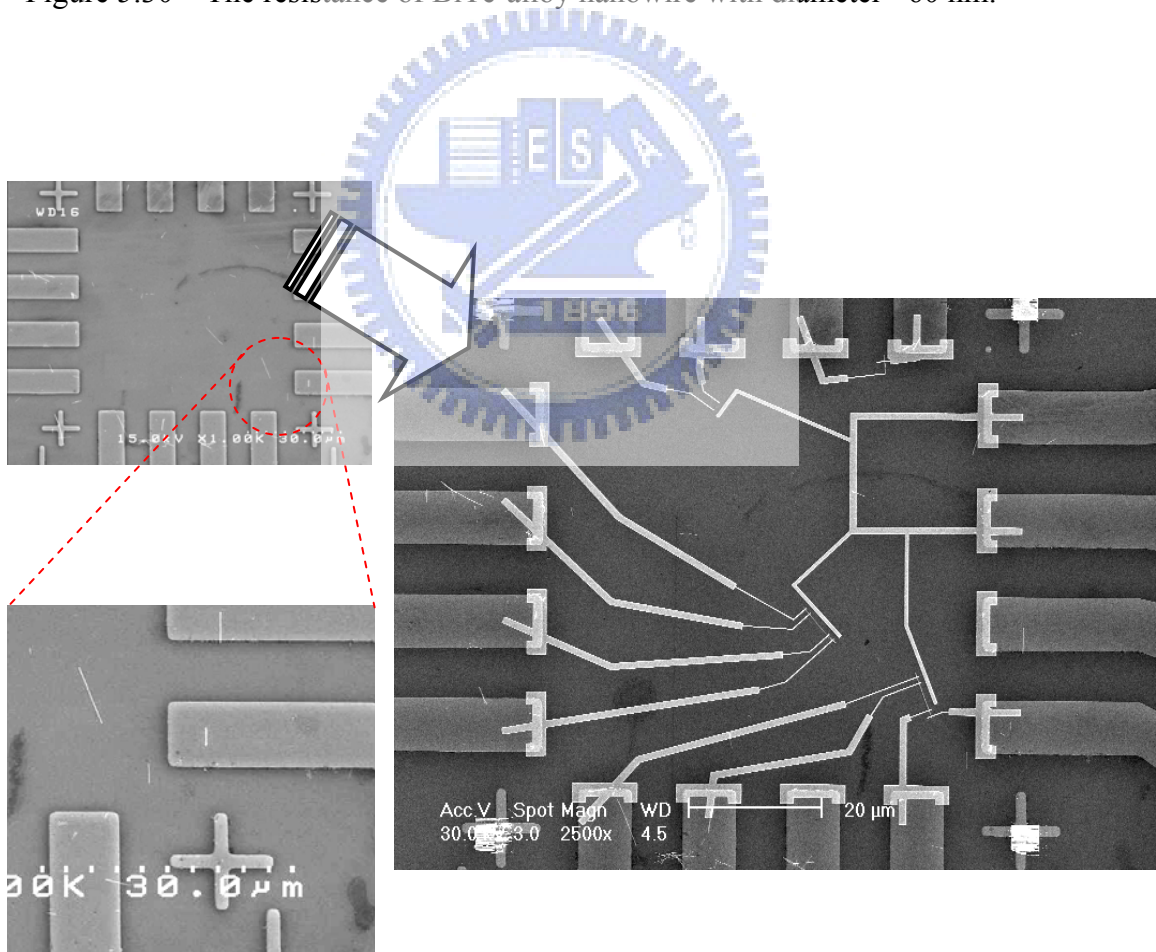
Figure 5.31   The electrodes for four-probe resistance measurement were obtained by e-beam lithograph technique.

Chapter 6

Conclusions

This study began with emphasis on synthesizing nanowire (NW) clusters—separated and ideally identical nanowires being treated as a single entity in certain physical properties measurements. The obtained data can be used to derive the average value for a given property of each single nanowire. A bottom-up method was employed to prepare such materials based on iron (FeNW) and Bi_2Te_3 (BTNW). First, we used a chemical anodize process to prepare a porous alumina as host template. Although the pore diameter of the anodic aluminum oxide (AAO) could be as small as 25 nm, but the filling rate of the follow-up chemical electrodeposition becomes quite low for the pore size below 30 nm. Therefore, two templates with pore-diameter of about 60 and 200 nm, respectively, were chosen to grow FeNW and BTNW. The average diameters of regularly ordered FeNW and BTNW are about the same size of AAO pores, and their morphology is confirmed by scanning electron microscopy (SEM) images. XRD patterns show clear texture along the nanowire longitudinal-axis in 60-nm FeNW and BTNW, indicating that the lattice structure of crystalline nanowire is affected by the geometric-dimension of pores.

As expected, the magnetization hysteresis loop of 60-nm FeNW depends on lattice texture, which shows a stronger magnetic anisotropic behavior than that of 200-nm sample. Magnetoresistance (MR) measurements on the 60-nm FeNW yielded a significant and parabolic field dependence MR. This can be attributed to the geometric effect, since the 60-nm FeNW has large aspect ratio (length to diameter ratio > 1000). In addition, the electrical resistivity of both FeNW and BTNW was in the exceedingly high range of 1 to 10 Ω-cm, implying that most of the nanowires

inside template had partially necked cross-sections or even broken sections.

Although the template method provided an easy way to study magnetism of nanowires, but unfortunately it is difficult to study their transport properties due to cracks of nanowires in template. To overcome this, a novel process was developed to form a single nickel nanowire. Starting with a 100-nm nickel film grown on a Si/Si$_3$N$_4$ substrate by thermal evaporation, a sagging nickel nanowire was then fabricated through e-beam lithography and etching processes. The width and length of the wire were determined by SEM as 180 nm and 35 μm respectively. Its thermal conductivity (κ), specific heat (Cp) and resistivity (ρ) were measured in the temperature range from 15 to 300 K by means of a "self heating 3ω" technique. The thermal conductivity is ~ 20% of the bulk at 300 K, then decrease with temperature in the whole temperature range in opposite to that of the bulk. This behavior might be explained by the restriction of mean free path of electron/phonon–phonon interactions due to grain boundaries and defects. In addition, the resistivity of nanowire at room temperature is about four times larger than that of the bulk, and the small residual resistivity ratio (RRR) confirms the polycrystalline characteristic of the nanowire. The average ratio of thermal-to-electrical conductivity is 2.68 × 10^{-8} W-Ω/K^2, which suggests that thermal current in this material is suppressed more than electrical current. In this regard, the transport properties are dominated by the electronic component. The large reduction of electronic thermal conductivity can be attribute to the combination of confined dimension, enhanced disorder and increased contribution of *N-processes*. On the other hand, the monotonic decrease of thermal conductivity indicates that the high electronic thermal resistance predominates the heat transport behavior in the nanowire materials. Furthermore, the enhancement of ~250% of the bulk in specific heat was also observed, which is presumably caused by the softening of vibration modes of nanocrystalline, surface effects, and defects.

Reference

1. D. H. Reich, M. Tanase, and A. Hultgren, L. A. Bauer, C. S. Chen and G. J. Meyer, J. App. Phys. 93, 7275 (2003)

2. M.Shiraki, Y.Wakui, T.Tokushima and N.Tsuya, IEEE Trans. Magn. MAG-21, 1465 (1985)

3. L. Sun, Y. Hao, C.-L. Chien and P. C. Searson, IBM J. RES. & DEV. 49, 79(2005)

4. K. Liu, K. Nagodawithana, P. C. Searson, and C. L. Chien, Phys. Rev. B 51,7381 (1995)

5. Vassil Skumryev, Stoyan Stoyanov, Yong Zhang, George Hadjipanayis, Dominique Givord and Josep Nogue´s, Nature 423,850 (2003)

6. Dieter Weller and Andreas Moser, IEEE TRANS ACTIONS ON MAGNETICS 35, 4423 (1999)

7. D. A. Thompson and J. S. Best, IBM J. RES. DEVELOP 44, 311 (2000)

8. D. A. Allwood, T. Schrefl, G. Hrkac, I. G. Hughes and C. S. Adams, Appl. Phys. Lett. 89, 014102 (2006)

9. J. Velev, R.F. Sabirianov, S.S. Jaswal, and E.Y. Tsymbal, Phys. Rev. Lett. 94, 127203 (2005)

10. W. Wernsdorfer, R. Clerac, C. Coulon, L. Lecren, and H. Miyasaka, Phys. Rev. Lett. 95, 237203 (2005).

11. D.A. Allwood, G. Xiong, C.C. Faulkner, D. Atkinson, D. Petit, R.P. Cowburn, Science 309 1688 (2005).

12. S. Brands, B. Leven, and G. Dumpich, J. Appl. Phys. 97,114311 (2005).

13. U. Ebels, A. Radulescu, Y. Henry, L. Piraux, and K. Ounadjela, Phys. Rev. Lett. 84, 983 (2000).

14. S. Mani, T. Saif, and J. H. Han, IEEE Trans. On Nanotech. 5, 138 (2006).

15. J-E. Wegrowe, D.Kelly, A. Franck, S.E. Gilbert, and J-Ph. Ansermet, Phys. Rev. Lett. 82, 3681 (1999).

16. I.S. Beloborodov, K.B. Efetov, A.V. Lopatin, and V.M. Vinokur, Phys. Rev. Lett. 91, 246801-1 (2003).

17. G. Reiss, J. Vancea, and H. Hoffmann, Phys. Rev. Lett. 56, 2100 (1986).

18. X.Y. Qin, W. Zhang, L.D. Zhang, L.D. Jiang, X.J. Liu, D. Jin, Phys. Rev. B 56, 10596 (1997-II).

19. N.V. Volkenshtein, V.P. Dyakina, and V.E. Startsev, Phys. Status Solidi B 57, 9 (1973).

20. M.J. Rice, Phys. Rev. Lett. 20, 1439 (1968).

21. E.P. Wohlfarth, Ferromagnetic materials, (Elsevier, North-Holland, 1980) p.634.

22. V. Tripathi and Y.L. Loh, Phys. Rev. Lett.   96, 046805 (2006).

23. I.S. Beloborodov, A.V. Lopatin, F.W.J. Hekking, R. Fazio and V.M. Vinokur, Europhys. Lett. 69, 435 (2005)

24. J. Heremans, C. M. Thrush. Y.-M. Lin, S. Cronin, Z. Zhang, M. S. Dresselhaus, J. F. Mansfield, Phys. Rev. B 61, 2921 (2000).

25. A. J. Yin, J. Li, W. Jian, A. J. Bennett, and J. M. Xu, Appl. Phys. Lett. 79, 1039 (2001).

26. X. Y. Zhang, L. D. Zhang, W. Chen, G. W. Meng, M. J. Zheng, and L. X. Zhao, Chem.Mater. 13, 2511(2001).

27. T. M. Whitney, J. S. Jiang, P. C. Searson, C. L. Chien, SCIENCE 261, 1316 (1993)

28. L. C. Sampaio, E. H. C. P. Sinnecker, and G. R. C. Cernicchiaro, M. Knobel, M. Va´zquez and J. Vela´zquez, Phys. Rev. B 61, 8976 (2000)

29. D. J. Sellmyer, M. Zheng and R. Skomski, J. Phys.: Condens. Matter 13, R433–R460 (2001)

30. J. B. Wang, X. Z. Zhou, Q. F. Liu, D. S. Xue, F. S. Li, B. Li, H. P. Kunkel and Gwilliams, Nanotechnology 15, 485–489 (2004)

31. L. Piraux, J. M. George, J. F. Despres, C. Leroy, E. Ferain, R. Legras K. Ounadjela and A. Fert, Appl. Phys. Lett. 65, 2484 (1994)

32. C. Kittel, Introduction to Solid State Physica, 8th ed. Wiley, 2005

33. Neil W. Ashcroft, N. D. Mermin, Solid State Physics, Thomson Learning, 1976

34. T. M. Tritt, Thermal Conductivity-Theory, Properties, and Applications, 2004)

35. G.S. Nolas, J. Sharp, H.J. Goldsmid, 'Thermolectrics' 2001.

36. G. Chen, M. S. Dresselhaus, G. Dresselhaus, J.-P. Fleurial and T. Caillat, International Materials Reviews 48, 1 (2003)

37. T. M. Tritt, Recent Trends in Thermmoeletric Materials Research, Semicond. Semimet., 69-71, 2001

38. L.D. Hicks and M.D. Dresselhaus, Phys. Rev. B 47, 12727 (1993).

39. T.C. Harman, P. J. Taylor, D. L. Spears and M. P. Walsh, Proc. 18th Int. Conf. on Thermoelectrics (ed.Ehrlich, A.), 280 (IEEE, Piscataway, NJ, 1999).

40. R. Venkatasubramanian, et al., Proc. 1st Natl Thermogenic Cooler Workshop (ed. Horn, S. B.), 196 (Center for Night Vision and Electro-Optics, Fort Belvoir, VA, 1992).

41. R. tasubramanian, Naval Res. Rev. 58, 31 (1996).

42. S. M. Lee, D. G. Cahill and R. Venkatasubramanian, Thermal conductivity of Si-Ge superlattices. Appl. Phys. Lett. 70, 2957 (1997).

43. G. D. Mahan and L. M. Woods, Phys. Rev. Lett. 80, 4016 (1998).

44. G. Chen Heat Transfer in Micro- and Nanoscale Photonic Devices Annu. Rev.

Heat Trans. 7, 1^57 (1996).

45. K. Goodson and Y. Ju Heat Conduction in Novel Electronic Films Annu. Rev. Mater. Sci. 29, 261^ 293 (1999).

46. G. Chen, T. Borca-Tasciuc, B. Yang, D. Song, W. L. Liu, T. Zeng and D. Achimov Heat Conduction Mechanisms and Phonon Engineering in Superlattice Structures Therm. Sci. Eng. 7, 43 (1999).

47. G. Chen, T. Zeng, T. Borca-Tasciuc, and D. Song Phonon Engineering in Nanostructures for Solid-State Energy Conversion Mater. Sci. Eng. A 292, 155^161 (2000).

48. See, for example, Thermal Conductivity of Solids, J. E. Parrott and A. D. Stuckes (Pion Limited Press, 1975), T. C. Harman and J. M. Honig, Thermoelectric and Thermomagnetic E¡ects and Applications (McGraw-Hill, New York, 1967).

49. L. R. Holland, J. Appl. Phys. 34, 2350 (1963).

50. D. Gerlich, B. Abeles, and R. E. Miller, J. Appl. Phys. 36, 76 (1965).

51. L. R. Holland and R. C. Smith, J. Appl. Phys. 37, 4528 (1966).

52. D. G. Cahill and R. O. Pohl, Phys. Rev. B 35, 4067 (1987).

53. N. O. Birge and S. R. Nagel, Rev. Sci. Instrum. 58, 1464 (1987).

54. D. G. Cahill, E. Fischer, T. Klitsner, E. T. Swartz, and R. O. Pohl, J. Vac. Sci. Technol. A 7, 1259 (1989).

55. David G. Cahill, "Thermal conductivity measurement from 30 to 750 K: the 3ω method", Rev. Sci. Instrum. 61 (2), 802 (1990)

56. R. Frank, V. Drach, and J. Fricke, Rev. Sci. Instrum. 64, 760 (1993).

57. D. H. Jung, T. W. Kwon, D. J. Bae, I. K. Moon, and Y. H. Jeong, Meas. Sci. Technol. 3, 475 (1992).

58. L. Lu, W. Yi, and D. L. Zhang, Rev. Sci. Instrum., 72, 2996 (2001)

59. D. J. Sellmyer, M. Zheng and R. Skomski, J. Phys.: Condens. Matter 13, R433–R460 (2001)

60. J. B. Wang, X. Z. Zhou, Q. F. Liu, D. S. Xue, F. S. Li, B. Li, H. P. Kunkel and Gwilliams, Nanotechnology 15, 485–489 (2004)

61. L. Piraux, J. M. George, J. F. Despres, C. Leroy, E. Ferain, R. Legras K. Ounadjela and A. Fert, Appl. Phys. Lett. 65, 2484 (1994)

62. F. Rousseaux, D. Decanini, F. Carcenac, E. Cambril, M. F. Ravet, C. Chappert, N. Bardou, B. Bartenlian and P. Veillet, J. Vac. Sci. Technol. B 13, 2787 (1995)

63. O. Fruchart, J.-P. Nozie`res, B. Kevorkian, J.-C. Toussaint, D. Givord, F. Rousseaux, D. Decanini and F. Carcenac, Phys. Rev. B 57, 2596 (1998)

64. F. Wacquanta, S. Denolly, J.-P. Nozie` res, D. Givord, and V. Mazauric, J. Appl. Phys. 85, 5484 (1999)

65. P.G. Shao, J.A. van Kan, K. Ansari, A.A. Bettiol and F. Watt, Nuclear Instruments

and Methods in Physics Research B 260, 479–482 (2007)

66. B. Roxlo, H. W. Deckman, J. Gland, S. D. Cameron, R. Cianelli, Science 235, 1629 (1987).

67. K. Douglas, G. Devaud, N. A. Clark, ibid. 257,642 (1992).

68. G. E. Possin, Rev. Sci. Instrum. 41, 772 (1970).

69. W. D. Williams and N. Giordano, ibid. 55,410 (1984).

70. C. A. Huber et al., Science 263, 800 (1994).

71. C.-G. Wu and 1. Bein, ibid. 264, 1757 (1994).

72. F. Keller, M. S. Hunter, and D. L. Robinson, J. Electrochem. Soc. 100, 411 (1953).

73. J. P. O'Sullivan and G. C. Wood, Proc. R. Soc. London, Ser. A 317, 511(1970).

74. G. Bailey and G. C. Wood, Trans. Inst. Metal. Finish. 52, 187 (1974).

75. G. E. Thompson and G. C. Wood, Nature ~London! 290, 230 (1981).

76. V. P. Parkhutik and V. I. Shershulsky, J. Phys. D: Appl. Phys. 25, 1258 (1992).

77. H. Masuda and K. Fukuda, ''Ordered metal nanohole arrays made by a two-step replication of honeycomb structures of anodic alumina'' Science 268, 1466–1468 (1995).

78. O. Jessensky, F. Mu¨ller, and U. Go¨sele, ''Self-organized formation of hexagonal pore arrays in anodic alumina,'' Appl. Phys. Lett. 72, 1173–1175 (1998).

79. K. Nielsch, J. Choi, K. Schwirn, R. B. Wehrspohn, and U. Go¨sele, ''Selfordering regimes of porous alumina: The 10% porosity rule'' Nano Lett. 2, 677–680 (2002).

80. A. P. Li, F. Mu¨ller, A. Birner, K. Nielsch, and U. Go¨sele, ''Hexagonal pore arrays with a 50–420 nm interpore distance formed by self-organization in anodic alumina'' J. Appl. Phys. 84, 6023–6026 (1998).

81. O. Jessensky, F. Mu¨ller, and U. Go¨sele, ''Self-organized formation of hexagonal pore structures in anodic alumina'' J. Electrochem. Soc. 145, 3735–3740 (1998).

82. F. Li, L. Zhang, and R. M. Metzger, ''On the growth of highly ordered pores in anodized aluminum oxide'' Chem. Mater. 10, 2470–2580 (1998).

83. H. Masuda, K. Yada, and A. Osaka, ''Self-ordering of cell configuration of anodic porous alumina with large-size pores in phosphoric acid solution'' Jpn. J. Appl. Phys., Part 2 37, L1340–L1342 (1998).

84. S. Shingubara, O. Okino, Y. Sayama, H. Sakaue, and T. Takahagi, ''Ordered two-dimensional nanowire array formation using self-organized nanoholes of anodically oxidized aluminum'' Jpn. J. Appl. Phys., Part 1 36, 7791–7795 (1997).

85. S. A. Knaack, M. Redden, and M. Onellion, ''AAO nanopore arrays: A practical entre´e to nanostructures'', Am. J. Phys. 72 (7), (2004)

86. F. Keller, M. S. Hunter, D. L. Robinson, J. Electrochern. Soc. 100, 411 (1953).

87. G. E. Thompson, R. C. Furneaux, G. C. Wood, J. A. Richardson, J. S. Gode, Nature 272, 433 (1978).

88. S. Kawai and R. Ueda, J. Electrochem. Soc. 122, 32 (1975).

89. M. Shiraki, Y. Wakui, 1. Tokushima, N. Tsuya, IEEE Trans. Magn. MAG-21, 1465 (1985).

90. M. Saito, M. Kirihara, T. Taniguchi, M. Miyagi, Appl. Phys. Lett. 55, 607 (1989).

91. C. J. Miller and M. Majda, J. Am. Chern. Soc. 107, 3118 (1985).

92. M. J. Tierney and C. R. Martin, J. Electrochem. Soc. 137, 3789 (1990).

93. Yoshino and N. Baba, J. Chern. Soc. Jpn. 1983, 955 (1983).

94. I. Mizuki, Y. Yamamoto, 1. Yoshino, N. Baba, J. Metal Surf. Finish. Soc. Jpn. 38, 561 (1987).

95. T. Ohgai1, L. Gravier, X. Hoffer, M. Lindeberg, K. Hjort, R. Spohr and J-Ph Ansermet, Template synthesis and magnetoresistance property of Ni and Co single nanowires electrodeposited into nanopores with a wide range of aspect ratios, J. Phys. D: Appl. Phys., 36, 3109–3114 (2003)

96. Gabor L. Hornyak, Joydeep Dutta, Harry F. Tibbals, Anil K. Rao, introduction to Nanoscience, CH4, page 201

97. A. J. Yin, J. Li, W. Jian, A. J. Bennett, and J. M. Xu, Appl. Phys. Lett. 79, 1040 (2001)

98. D. AIMawlawi, N. Coombs and M. Moskovits, J. Appl. Phys. 70, 4421 (1991)

99. J. B. Wang, X. Z. Zhou, Q. F. Liu, D. S. Xue, F. S. Li, B. Li, H. P. Kunkel and Gwilliams, Nanotechnology 15, 485–489 (2004)

100. C.H. Marrows, Advances in Physics 54, 585-713 (2005)

101. M. Brandsa and G. Dumpich, J. Appl. Phys. 98, 014309 (2005)

102. C. Reale, J. Phys. F: Metal Phys. 4, 2218 (1974)

103. G.K. White, S.B. Wood, Electrical and thermal resistivity of the transition elements at low temperatures. Phyl. Trans. Of Roy. Soc., v.251, A995, 273 (1959)

104. A. Bid, A. Bora, A.K. Raychaudhuri. Temperature dependence of the resistance of metallic nanowiers of diameter $\geq$ 15nm: Applicability of Bloch-Gruneisen theorem. Phys. Rev. B., v. 74, 035426 (2006)

105. B. Fultz, C.C. Ahn, E.E. Alp, W. Sturhahn, T.S. Toellner. Phonon in Nanocrystalline 57Fe. Phys. Rev. Lett, v. 79, 937 (1997)

106. H. Frase, B.Fultz. Phonon in nanocrystalline Ni3Fe. Phys. Rev. B., v. 57, 898 (1998)

107. L. Lu, W. Yi, and D. L. Zhang, Rev. Sci. Inst., v. 72, #7, 2996 (2001)

108. G.K. White, S.B. Wood, Phyl. Trans. Roy. Soc. 251, A995, 273 (1959)

109. Zh. Zhou, C. Uher, D. Xu, W.L .Johnson, W Gannon, M. C. Aronson, Appl. Phys. Lett. 89, 031924 (2006).

110. Q. G. Zhang, B. Y. Cao, X. Zhang, M. Fujii, K. Takahashi, Phys. Rev. B 74, 134109 (2006).

111. Y. Yang, J.-G. Zhu, R. M. White, M. Asheghi, J. Appl. Phys. 99, 063703 (2006).

112. R. Berman, Thermal Conduction in Solids (Oxford University Press, Oxford, 1976), p.143.

113. G. K. White, and R. J. Tainsh, Phys. Rev. Lett. 19, 165 (1967).

114. Y. Zhang, N. P. Ong, Z. A. Xu, K. Krishana, R. Gagnon, and L. Taillefer, Phys. Rev. Lett. 84, 2219 (2000).

115. Peter J. Meschter, James W. Wright, Charlie R. Brooks and Thomas G. Kollie, J. Phys. Chem. Solids 42, 861 (1981)

著作目錄

1. Size effect on magnetic ordering in Ce_3Al_1
    C.R. Wang*, Y.Y. Chen, S.Neeleshwar, M.N. Ou, J.C. Ho, Physica B 329–333, 620–621 (2003)

2. Superconductivity in aluminum nanoparticles
    S. Neeleshwar*, Y.Y. Chen, C.R. Wang, M.N. Ou, P.H. Huang, Physica C 408–410, 209–210 (2004)

3. Magnetic and calorimetric studies of antiferromagnetic transitions in erbium sesquisulfide
    C.R. Wang, Y.Y. Chen, Y.D. Yao, Y.S. Lin, M.N. Ou, S.M.A. Taher, H.H. Hamdeh, X. Zhang, J.C. Ho*, John B. Gruber, Journal of Magnetism and Magnetic Materials 269, 419–422 (2004)

4. Superconducting transition parameters in aluminum–lithium alloys (0–10 at.% Li)
    M.N. Ou, T.J. Yang, B.J. Chen, Y.Y. Chen, J.C. Ho*, Solid State Communications 142, 421–424 (2007)

5. Thermal and electrical transport properties of a single nickel nanowires
    M. N. Ou*, S. R. Harutyunyan, S. J. Lai, C. D. Chen, T. J. Yang, and Y. Y. Chen, Physica Status Solidi (b) 244, 4512–4517 (2007)

6. Kondo Interactions and Magnetic Correlations in $CePt_2$ Nanocrystals
    Y.Y. Chen*, P. H. Huang, M. N. Ou, C. R. Wang, Y. D. Yao, T. K. Lee, M.Y. Ho, J. M. Lawrence, and C. H. Booth, Physical Review Letters, 98, 157206 (2007)

7. Electrical and thermal transport in single nickel nanowire, Applied Physics Letters
    M. N. Ou, T. J. Yang, S. R. Harutyunyan, Y. Y. Chen*, C. D. Chen, and S. J. Lai, 92, 063101 (2008).

8. Anisotropic magnetism and magnetoresistance in iron nanowire arrays
    M. N. Ou, T. J. Yang, and Y. Y. Chen*, Chinese Journal of Physics, accepted